THESIS REPORT
Master's Degree

S Y S T E M S
R E S E A R C H
C E N T E R

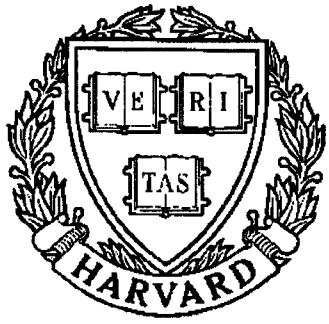

Supported by the National Science Foundation Engineering Research Center Program (NSFD CD 8803012), the University of Maryland, Harvard University, and Industry

Investigation of the Thrust and Torque Generated during Drilling Processes

by H-F. Hsieh
Advisor: G.M. Zhang

M.S. 92-4

ABSTRACT

Title of Thesis:	Investigation of the Thrust and Torque Generated during Drilling Processes
Degree candidate:	Hsiang-Fu Hsieh
Degree and Year:	Master of Science, 1992
Thesis directed by:	Dr. Guangming Zhang, Assistant Professor Department of Mechanical Engineering and Systems Research Center

This thesis presents a study of the thrust and torque generated during drilling processes, with emphasis on applications to perform on-line monitoring of drilling processes. Two mathematical models are developed for quantitatively relating the thrust and torque to the machining parameters and drill geometry. A modal testing is conducted to identify the effect of drill structure on thrust and torque generation. In addition, a prototype sensing system is employed to measure the thrust and torque in an on-line fashion. The prototype sensing system shows great promise for integration with the mathematical model to produce untended drilling systems.

Analytically, an unique approach for evaluating the thrust and torque generated during drilling processes is developed. Mathematical models relating drill geometry (point angle, helix angle, drill radius and web thickness) and cutting parameters (feed rate and spindle speed) are established based on machining science. Specifically, a force analysis is performed on the geometry of a twist drill. Experimentally, a dynamometer for measuring the thrust and torque during drilling is designed and

fabricated. The sensing system is calibrated and tested to demonstrate the capability of detecting the dynamic variation of the generated thrust and torque. Effects of the cutting parameters are investigated and explained through a two-level design experimentation.

The sensing system described in this thesis is a prototype of a sensor-based drilling system. A strategy for implementing such a system on the shop floor is proposed, suggesting the direction of future research for achieving high quality and productivity with the drilling process.

INVESTIGATION OF THE THRUST AND TORQUE GENERATED DURING DRILLING PROCESSES

by

Hsiang-Fu Hsieh

THESIS
submitted to the Faculty of the Graduate School
of The University of Maryland in partial fulfillment
of the requirements for the degree of
Master of Science
1992

Advisory Committee:

Assistant Professor Guangming Zhang, Chairman/Advisor
Professor Jackson Yang
Assistant Professor Mohamed K. Abdelhamid

ACKNOWLEDGEMENTS

I would like to express my gratitude to my advisor, Dr. Guangming Zhang, who always provided enthusiastic guidance, encouragement, and support during this project. I would like to thank Dr. Mohamed Abdelhamid for his valuable advisement throughout the course of this research. Also, I would like to thank Dr. Jackson Yang for his assistance.

I thank my fellow students in Dr. Zhang's group: Tsuwei, Raju, Farukh, and Jayant for their help. A special thanks goes to Tsuwei, who helped me with the drilling force measuring, the experimental data processing, and the thesis editing on weekends or even overnight.

Thanks are also due to Mr. Robert Bonenberger of the Photomechanics Laboratory, who helped me with installation of the strain gages, wire soldering, thesis writing, etc. I thank Mr. Bob Anders of the machine shop, Mr. David Hahn of the Measurements Laboratory, and Mr. David Pelgrim of the SAE Laboratory, who provided practical assistance and technical support for the construction of the drilling dynamometer and the instrumentation for the drilling experiments. I would also like to thank Mr. Winbin Shieh, Mr. Yeongshu Chen, and Mr. Steve Wells of the Vibrations Laboratory, who helped me set up the modal testing experiment.

Finally, I want to express my respect to my parents, for their patient concern and support. Also I want to thank my fiancee in Taiwan, for her true love and constant encouragement from far away.

TABLE OF CONTENTS

PAGE

LIST OF FIGURES

LIST OF TABLES

PAGE

NOMENCLATURE

A	Modal constant
Ac	Chip load
As	Cross section area of the cylinder
Cn, Cn', Cn"	Proportionality coefficient in the formula of cutting force Rn
Cp	Proportionality coefficient of the penetration rate
Cs	Lead angle
Ct, Ct', Ct"	Proportionality coefficient in the formula of cutting force Rt
Cv	Proportionality coefficient for cutting force with respect to speed
D	Diameter of the drill
d	Depth of cut
E	Young's modules
F	Feed rate level, equals +1 at higher level and -1 at lower level
Fc	Cutting force
$\vec{F}e^{i\omega t}$	Harmonic input force to the structure
$F_{in}(\omega)$, $F_k(\omega)$	Input force to the system in frequency domain
Fn	Cutting force normal to the finished surface
Ft	Cutting force tangential to the finished surface
F(t)	Cutting force
f	Feed rate
H1, H2, H3	Holes of different diameters in the workpiece specimens
IF_{fn}	Interaction effect of spindle speed and feed rate
i	Complex value
i	Inclination angle
$I(\omega)$, I_{17}, I_{27}	Inertance of the system
J_s	Polar moment of inertia

j	Index number of the section along the cutting edges
j_{in}, j_{out}	Index numbers of the inner and outer sections engaged in cutting
Kc	Cutting stiffness
Ks	Proportionality coefficient; unit cutting force
Kv,Kp,Kt	Proportionality coefficients in Tobias' and Zhang's models
k1, k2, k3	Proportionality coefficients for p_1, p_2, p_3
Mean	Mean of the factorial design experimentation
MF_f	Main effect of feed rate
MF_n	Main effect of spindle speed
N	Spindle speed level, equals to +1 at higher level; -1 at lower level
n	Spindle speed
nf	Exponential value of the feed rate factor for ΔRn
nr	Exponential value of the rake angle factor for ΔRn
nv	Exponential value of the cutting speed factor for ΔRn
p	Point angle
p_1	The tangential force component
p_2	The radial force component
p_3	The feed force component
R	Resultant cutting force
R'	force between the workpiece and the chip
R_a, R_b,	
$R_{ij}(\omega)$, $R_{jk}(\omega)$	Receptance of the system
R_g	The resistance of the strain gage
R_i	Inner radius of the cylinder
R_n	Cutting force normal to the rake face
R_s	Outer radius of the cylinder
R_t	Cutting force tangential to the rake face

R1, R2	Resistances of the two resistors in the operational amplifier
$R_{1,2,...,8}$	Resistances of the eight arms of the Wheatstone bridge
r	Radius of the drill (a variable)
${}_rA_{jk}$	Modal constant of the r^{th} mode with input of the j^{th} station and output of the j^{th} station
rD	Diameter of the modal circle
r_e	Ratio of the resistances in the Wheastone bridge
rR	Receptance at the resonance
S_g	Gage factor of strain gages
S_n	Cutting force normal to the shear plane
S_t	Cutting force tangential to the shear plane
TH, TH1, TH2, TH3	Thrust in the drilling processes
$TH1_{prd}$, $TH2_{prd}$, $TH3_{prd}$	Thrust prediction by the empirical models
TR	Transform matrix from output voltage to applied force
TRR	Transform matrix from applied force to output voltage
TQ	Torque in the drilling processes
$TQ1_{prd}$, $TQ2_{prd}$, $TQ3_{prd}$	Torque prediction by the empirical models
tf	Exponential value of the feed rate factor for ΔRt
tr	Exponential value of the rake angle factor for ΔRt
tv	Exponential value of the cutting speed factor for ΔRt
u, u(t)	Chip thickness
u_0	Nominal chip thickness
Vth	Thrust voltage output
Vtq	Torque voltage output

Vy	The penetration rate
Vz	The cutting velocity
w	Web thickness
wd	Width of cut
x_j, $x(\omega)$	Output displacement of the structure in the frequency domain
x(t)	Output displacement of the structure at the tip
$\vec{x}(t)$	Output displacement of the structure
y(t)	Tool motion
Z	Tool displacement in the tangential direction
α_b	Back rake angle
α_e	Effective rake angle
α_n	Normal rake angle
α_v	Velocity rake angle
α_s	Side rake angle
ΔEin	Input voltage of the Wheastone bridge
ΔEout1	Thrust output voltage increment in the Wheastone bridge
ΔEout2	Torque output voltage increment in the Wheastone bridge
ΔFx, ΔFy, ΔFz	Cutting forces of the sections in the x,y,z directions
ΔR	Variation of the resistance R
ΔR_n	Cutting force normal to the rake face of the section
ΔR_g	Resistance increment of the strain gage
ΔRt	Cutting force tangential to the rake face of the section
Δr	Drill radius increment
ΔTH(j)	Partial thrust of the j^{th} section
ΔTQ(j)	Partial torque of the j^{th} section
δ	Helix angle of the drill
ε	Strain

ϕ_{jr}	The j^{th} element of the r^{th} mode in mass normalized mode shapes
$[\phi]$	Mode shape matrix
γ	Split angle
η_c	Chip flow direction angle
$\eta, \eta_r, \eta_{1,2,3}$	Structural damping factor of the system
ν	Poison ratio of material
θ	Relief angle of the drill
$\theta a, \theta b$	Angle to the maximum receptance in the modal circle
σ_X, σ_Y	Normal stress in the X, Y axis
$\sigma_{X'}, \sigma_{Y'}$	Normal stress in the X', Y' axis
τ_{XY}	Shear stress in the X-Y plane
ω	Frequency of the excitation
ω_c	Angular velocity of the chip along the drill axis
ω_{dr}	Structural damped natural frequency of the r^{th} mode
ω_h	Resultant angular velocity of ω_c, ω_x, and ω_z.
$\omega_{Max(\|R(\omega)\|)}$	Frequency at the maximum absolute value of the receptance
ω_r	Natural frequency of the r^{th} mode
ω_x	Angular velocity of the chip along the cutting edge
ω_z	Angular velocity of the chip normal to ω_c and ω_x

CHAPTER 1

INTRODUCTION

In this chapter three topics are presented: background, technological needs, and scope of the thesis. Basic knowledge about drills, the mechanics of drilling processes, the importance of drilling processes in modern industries, and main issues of the research work are described.

1.1 Background

Drilling is one of the most basic machining operations performed by machinists. The process is used to make holes by first fixing a drill to the end of a rotating spindle, and then boring a hole through a stationary workpiece pressed against the drill. The drill is an end cutting rotary-type tool having one or more cutting lips and one or more flutes for the removal of chips and the passage of coolant.

There are many different types of drills. Examples are twist drills for general machining, rock drills for mining minerals, laser drills for extremely small holes, spade drills for large holes, and gun drills for deep holes. It was reported that the first and second drilling machines were developed in 1801 by an engineer at Soho Foundry. [20] The first machine-made twist drill appeared around the year 1860. Truly modern twist drill development actually began with the introduction of high-speed steel around the year 1900.[3] A variety of drills, such as split-point, racon, helico and multifaceted, were developed for specific functions around 1950 [33].

The twist drill is by far the most common type of drill used today and is often rated as the most efficient of all cutting tools. It is a tool which will stand a tremendous amount of abuse and still keep cutting. The geometry of a typical twist drill is shown in Figure 1.1. To understand the mechanics of the drilling process, one must understand two types of cutting processes: orthogonal cutting and oblique cutting. The main difference between the two cutting processes is the orientation of the tool's cutting edge with respect

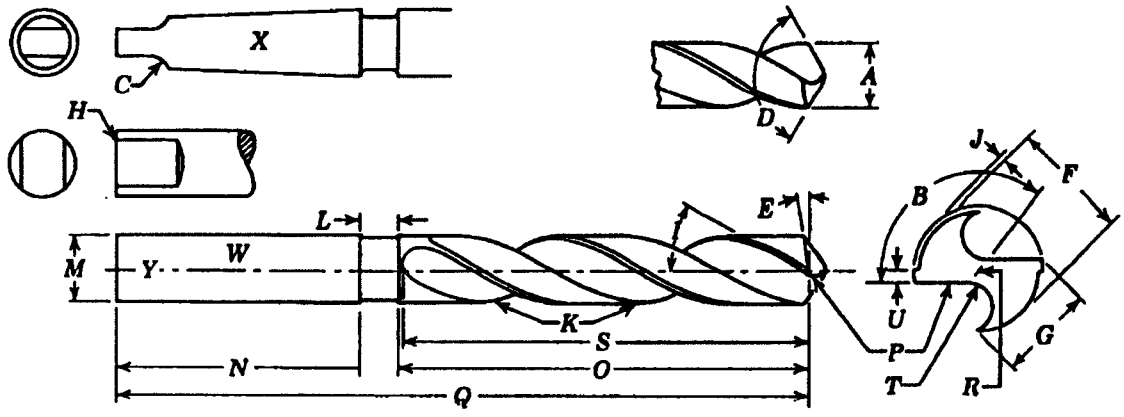

A -	Drill diameter	M -	Shank diameter
B -	Chisel edge angle	N -	Shank length
C -	Tang	O -	Body
D -	Drill point angle	P -	Cutting lip
E -	Lip relief angle	Q -	Over-all length
F -	Clearance diameter	R -	Chisel edge
G -	Land	S -	Flute length
H-	Tang drive	T -	Web
I -	Helix angle	U -	Margin
J -	Body diameter clearance	W -	Straight shank
K -	Flute	X -	Taper shank
L -	Neck	Y -	Axis of drill

Figure 1.1 Geometry of a typical twist drill (from [21]).

to the direction of the cutting velocity. According to Merchant's description of orthogonal cutting [16] ,"the tool is set so that its cutting edge is perpendicular to the direction of relative motion of the tool and workpiece and generates a plane surface parallel to the original work surface". The orthogonal cutting process is relatively simple, as shown in the Figure 1.2. Cutting of this type can be described in the plane containing both the tool motion vector and the normal to the finished surface. The relations between tool geometry, velocity, and cutting forces were developed by Merchant and have been accepted for years.

The second type of cutting process is oblique cutting. In oblique cutting processes, the cutting edge is rotated at an angle (90^{0}-i) relative to the direction of tool motion, as shown in Figure 1.3. Since the chip does not flow in the plane defined by the tool motion and the normal to the finish surface, the cutting action no longer can be described two-dimensionally. The relations between tool geometry, velocity, and cutting forces become more complex and will be discussed in detail later.

During drilling process, the observable forces are the thrust applied by the rotating drill to the workpiece and the torque supplied by the spindle to maintain the drill rotation. The thrust and torque of a general drilling process are caused by drill point. The drill point is the main cutting region and consists of the web and the lips, as shown in Figure 1.1. The drilling process for hole enlargement utilizes the lips only. It is common practice to machine a hole by drilling a small hole first and then enlarging the hole by employing larger diameter drills until the desired size is reached. This procedure tends to protect the drills and to increase production rate. The

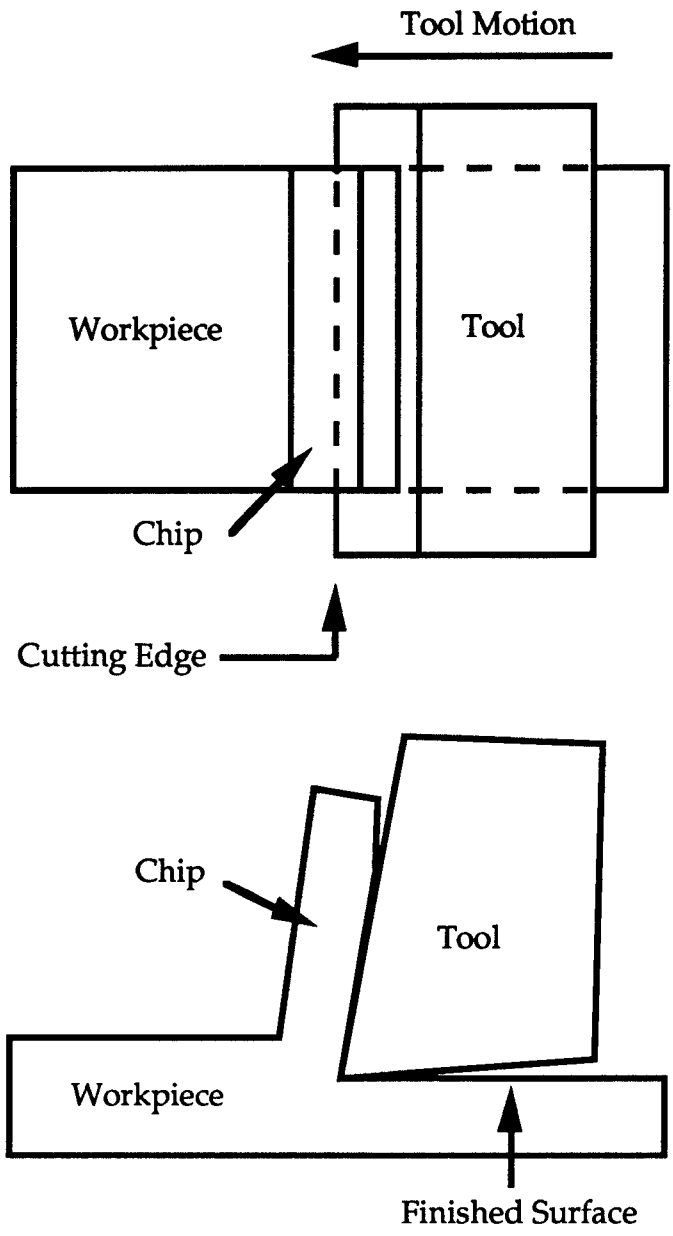

Figure 1.2 Orthogonal cutting geometry

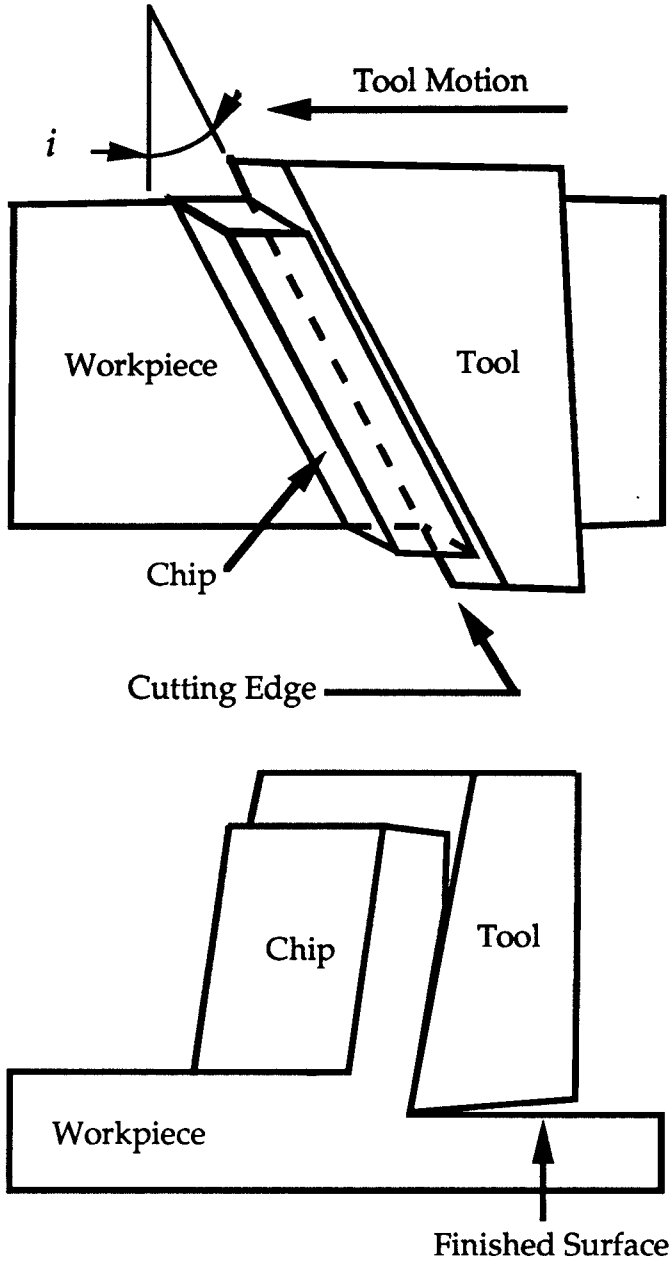

Figure 1.3 Oblique cutting geometry

drilling process is treated as a double oblique-cutting process by the lips, with varying inclination angles and geometry along the cutting edges. The details of the thrust and torque models will be discussed later.

Besides thrust and torque, a drill is subjected to a cutting force in the lateral direction due to unsymmetrical lips or misalignment of the drill axis. A drill subjected to a lateral cutting force will change the thrust and torque magnitudes, which is an indication of tool wear or system instability. Also, the vibration in the lateral direction greatly influences the quality of the finished hole.

1. 2 Technological Needs

Many industries make use of drilling processes. Modeling of drilling processes is remarkably important, especially under the conditions of high spindle speed and large feed rate, which accompany mass production and industrial automation. For instance, in a factory producing printed circuit boards, hundreds of holes on a board are drilled for soldering electrical components or wires. In an automatic assembly line, almost all parts pass through a machining station for screw hole or pin hole drilling processes.

Drills are easily worn by friction, heat, etc. and sometimes break when subjected to severe cutting forces at the lips, which are the main cutting regions and the weakest parts of the drill. In order to maintain finish quality, drills are changed by stopping the production line and reducing the production rate.. Vibration of the drills during machining creates elliptical finished holes, increases the difficulty and the cost of the post machining

processes, such as boring and taping, and also reduces the strength of the products (by introducing a stress concentration and metal fatigue).

By specifying the workpiece material properties, operating conditions, and drill geometries, the thrust and torque models are used to predict the corresponding cutting forces and machining performance of interest. Such models allow a CNC programmer to check the design of operating conditions such as feed rate and spindle speed before actual machining. Also, a tool designer can predict the performance of the designated tool geometry to improve the design, and a quality inspector can replace the inspection by a model simulation on a computer.

1.3 Scope of Thesis

This thesis is concerned with the drilling process of enlarging a hole which has already been cut in the workpiece. The mathematical thrust and torque models are established, which predict the effect of various cutting parameters and drill geometry on the performance measures. In light of these objectives, the main parts of the thesis deal with modeling of thrust and torque, structure identification, and measurement thrust and torque .

Chapter 2 is a review of the literature relative to drill geometry and the modeling of metal cutting processes. Important books and papers are surveyed, and key issues are discussed.

Chapter 3 describes the basic modeling methodology. The thrust and torque on a drill are obtained by summing cutting force vectors of small sections along a cutting edge and then using symmetry arguments. The cutting action of each section is approximated by orthogonal cutting in a

specific plane. The relations between tool geometry, velocity, and cutting forces are applied in the specific orthogonal cutting plane for each section. The total thrust is the summation of force components in the thrust direction for all sections of each lip. The total torque is the summation of the inner products of radius vectors and force components, in the direction normal to both quantities. Finally, chip formation during drilling processes is studied and related to the developed models.

Chapter 4 presents experimental work of a modal testing and analysis for the identification of dynamic characteristics of a twist drill. Instead of measuring the mass and stiffness of the structure, the modal parameters, natural frequencies, mode shapes, and damping factors are identified during vibration testing.

Chapter 5 describes the development of a force transducer and experiments performed by the force transducer. The construction of a drilling dynamometer for measuring the thrust and torque is depicted in three design stages: concept, structure, and gage layout. Experiments performed by drilling specially designed specimens for constant determination of the thrust and torque models are described. A two-level design experimentation is performed to estimate effects of the cutting parameters, feed rate and spindle speed. Dynamic characteristics of the drilling processes are also investigated based on the measured thrust and torque. The fundamental natural frequency of the dynamometer is found to be higher than that of the drill structure. This guarantees the stability of the machining processes and the precision level of the mean of the thrust and torque measurements.

Chapter 6 presents a factorial analysis of the thrust and torque measurements during the drilling tests. Empirical models are established to estimate the effects of the cutting parameters on the thrust and torque. A strategy for implementing a sensor-based drilling system on the shop floor control is presented. The prototype system to perform on-line monitoring of the drilling operation developed in the previous chapter will be discussed.

Chapter 7 summarizes the thesis and provides recommendations for future work in this area.

CHAPTER 2

LITERATURE REVIEW

A review of the literature pertaining to the development of thrust and torque models of drilling processes for hole enlargement is divided into four sections: machining system modeling, models of drilling structures, models of thrust and torque, and the purpose of the study. The first section presents a well-developed model to dynamically characterize a machining system, some applications, and continued development. The second section includes a survey of the developed theoretical models of drilling structures and an experimental method for structural identification. In the third section, the foregoing research work is discussed, and the cutting force in two-dimensional cutting is studied. The reasons for the thesis work are stated in the fourth section.

2.1 Machining System Modeling

A machining system basically consists of two subsystems: the cutting process and the machine tool structure. The output of the cutting process is the cutting force, which is the input to the machine tool structure. The output of the tool structure is tool motion, which affects the chip load, (the input of the cutting process). The machining system is naturally a complex closed-loop system. Many scientists have described the dynamic characteristics of machining systems in this manner. Merritt was the first to apply control theory to the study of machining systems [17]. He developed a theory of machine-tool chatter for stability analysis of an n-degree-of-

freedom (DOF) system. The three-step procedure for constructing the chatter loop is as follows:

(1) The instantaneous thickness of cut u(t) is formed by considering the reference or input thickness of cut u_0, workpiece (or tool) motion y(t), and regenerative feedback due to overlapping of successive cuts.

(2) The dynamic cutting force F(t) is assumed to be proportional to the thickness of cut, where the proportionality coefficient is a function of width of cut, workpiece material, and tool geometry.

(3) The dynamic compliance of the machine-tool structure is derived from 1 DOF , 2 DOF, to n DOF, and is visualized in the form of a frequency spectrum for stability criterion establishment.

By coupling the cutting process to the machine-tool-workpiece structure and feedbacking the uncut chip thickness, the chatter loop is constructed, as shown by the block diagram in Figure 2.1. Following Merritt's approach, many researchers have done significant work in this area.

Nachtigal and Cook were the first to demonstrate the applicability of an active control scheme to a turning operation [8]. Kline, Glaser, and Nachtigal also applied the same active control scheme to a boring operation [10]. Zhang linearized the system by treating the regenerative feedback path in Merritt's model as a second input [34]. In this work, the random excitation caused by nonhomogeneity in the hardness of the workpiece material was also investigated.

2.2 Models of Drilling Structures

The dynamic behavior of drills during machining is of great concern when strict tolerance of the holes must be met in the final product. During machining, the drill is fastened rigidly at the shank and is subjected to cutting forces along its two cutting edges. If the cutting force oscillates near the natural frequency of the drill structure, the drill will vibrate severely and degrade the quality of the finished surface or even cause instability and breakdown of the machining system.

A number of theoretical models of drill structures have been developed. Burnham tried to use a beam model to investigate the deflection due to a thrust force at the drill point. He found that under large feed rates, the drill may buckle and produce an over-size or off-center hole [4,5]. Galloway's work considered the fundamental mode of vibration of the drill

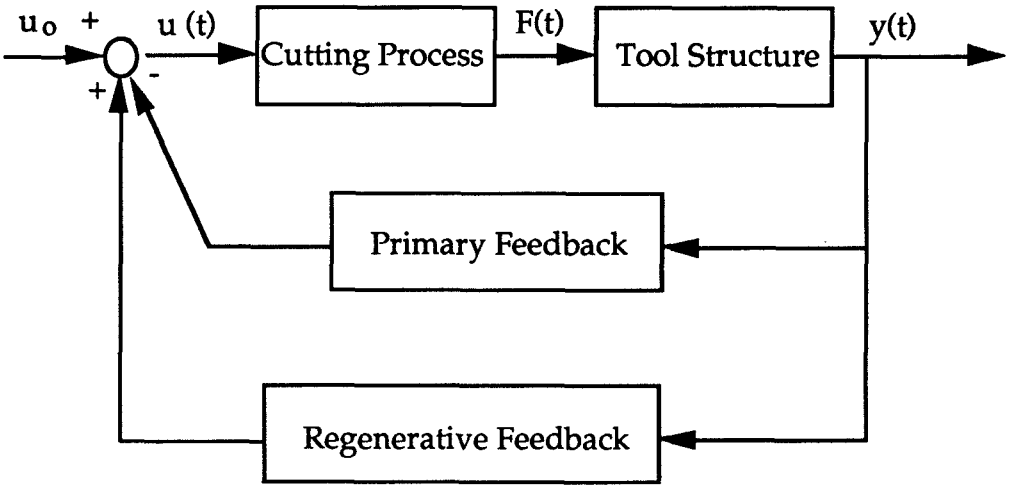

Figure 2.1 Merritt's machining system model.

in the axial direction, but did not mention the lateral vibration, which is closely related to the quality of the finished holes [7]. Magrab gave an explanation for the out-of-roundness of certain drilled holes due to the transverse vibration of drill bits [14]. The drill bit was modeled as a twisted Euler-type beam under axial compressive load that is clamped at both ends. The geometry of the cross section of the beam is chosen so that the torsional motion uncouples from the bending motion. In practice, the cross section of a drill is designed based on drilling performance by considering the power consumption, the strength of the drill, and the space of the flutes for chip removal.

The modal analysis method has been applied to solve dynamic system problems for many years [6]. By transforming the equations of motion from a spatial space (x, y, z, t-coordinates and time) to a modal space (ϕ, η, ω- mass normalized mode shape, damping factor, natural frequency), the solution in the modal space becomes easy to compute. After transforming back to spatial space, the solution in the time domain can also be obtained. Experimentally, instead of measuring the mass and stiffness of the structure, the modal parameters are identified through modal testing.

2.3 Models of Thrust and Torque

Because of their importance in nearly all production operations, twist drills have been the subject of numerous investigations. The most notable study is the work of Shaw and Oxford, Jr [22]. An analytical model relating thrust and torque to feed rate, web thickness and drill diameter was proposed. A quick-stop device and a special specimen were used during the investigation of the chip formation by the cutting lips and chisel edge. Based

on physical observations, the authors concluded that the web thickness of the drill had a strong influence on the thrust and torque. They established models by using the method of dimensionless reasoning [21].

Kaczmarek's work in Europe [9] was slightly different from Shaw's [22]. His experimental data, showing the contribution of the lips, the chisel, and the margins to the thrust and torque, is presented in Table 2.1. The chisel (i. e. web) seems to have little influence on the torque, but accounts for 40% of the thrust.

On the other hand, drilling processes for hole enlargement are only influenced by the cutting action of the tool lips. Such drilling processes may be approximated as two lathe tool points simultaneously engaged in an internal straight turning. This analogy makes the study of cutting mechanics during drilling processes similar to the study of cutting mechanics during turning processes, which facilitates the development of thrust and torque models of drilling processes for hole enlargement. Two basic issues in this study are described below for the construction of the proposed models: first, the comparison of orthogonal cutting processes and oblique cutting processes, and second, the developed cutting force models in two-dimensional cutting processes.

	Thrust	Torque
Lips	50%	80%
Margins	10%	12%
Chisel	40%	8%

Table 2.1 Kaczmarek's experimental results.

2.3.1 Orthogonal and Oblique Cutting Processes

Merchant developed force and velocity relations for the case of orthogonal cutting with a straight edged tool [21]. In his work, a compact diagram, shown in Figure 2.2 (a), was used to define the resultant cutting force and its various components. Some of the orthogonal cutting geometry definitions are also shown in Figure 2.2 (a), where α is the rake angle of the tool, ϕ_s is the shear angle, and t1 and t2 are the cut and uncut chip thicknesses. These force components are derived based on the equilibrium of the chip, as shown in Figure 2.2 (b). The force between the tool face and the chip, R, is equal to the force between the workpiece and the chip, R'. These forces R and R' can be decomposed into three pairs of orthogonal force components, which are normal and tangential to (i) the tool rake face (Rn and Rt), (ii) the shear plane (Sn and St) , and (iii) the workpiece surface (Fn and Ft). The resultant cutting force is obtained by measuring one pair of these components experimentally.

As mentioned in the previous chapter, the main difference between orthogonal and oblique cutting is the orientation of the tool with respect to the direction of the cutting velocity. Referring to Figure 2.3, for an oblique cutting process with the inclination angle i , there are three distinct rake angles: normal (oblique) rake, α_n; velocity (true) rake, α_v; and effective rake, α_e. The normal rake angle, $\angle$DOA, is measured in the plane containing the normals to both the cutting edge and the finished surface. The velocity rake angle, $\angle$DOB, measured in the plane containing the normal to the finished surface and the cutting-velocity vector, is insignificant and is mentioned here only due to its presence in past literature. The effective rake angle,

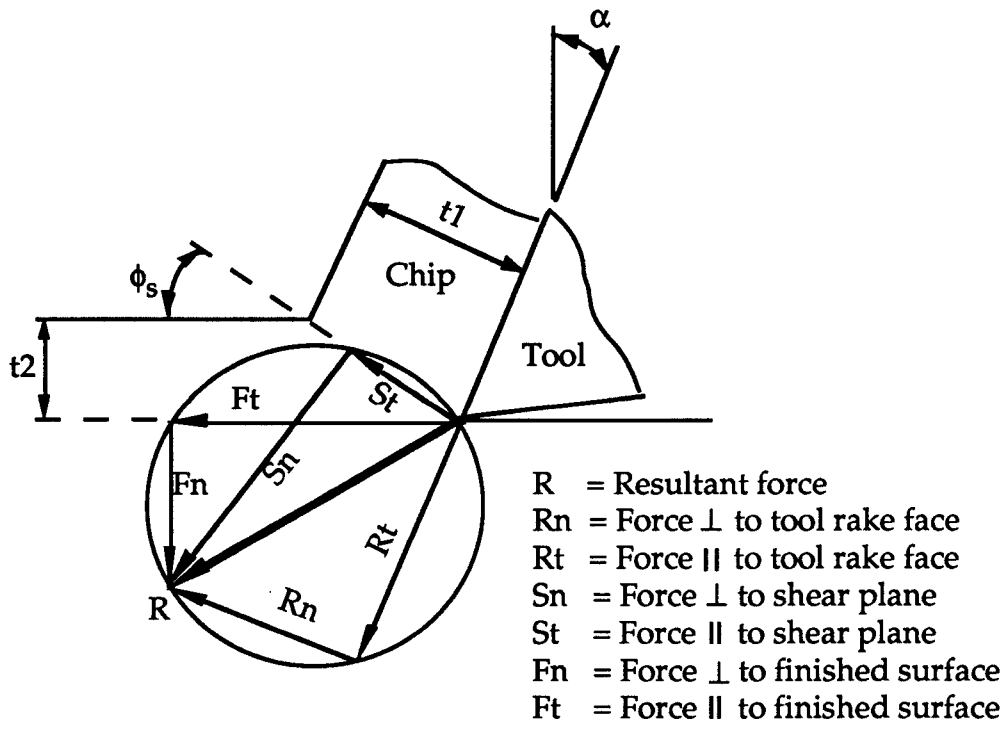

Figure 2.2 (a) Merchant's force circle for orthogonal cutting.

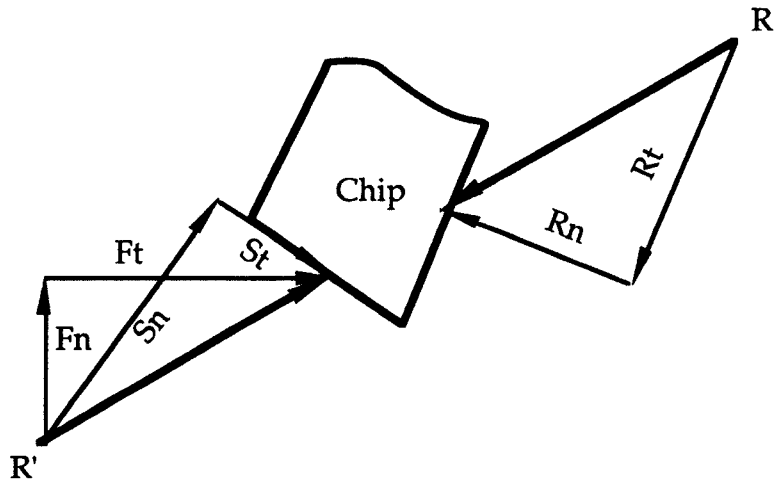

Figure 2.2 (b) Free body diagram of a chip.

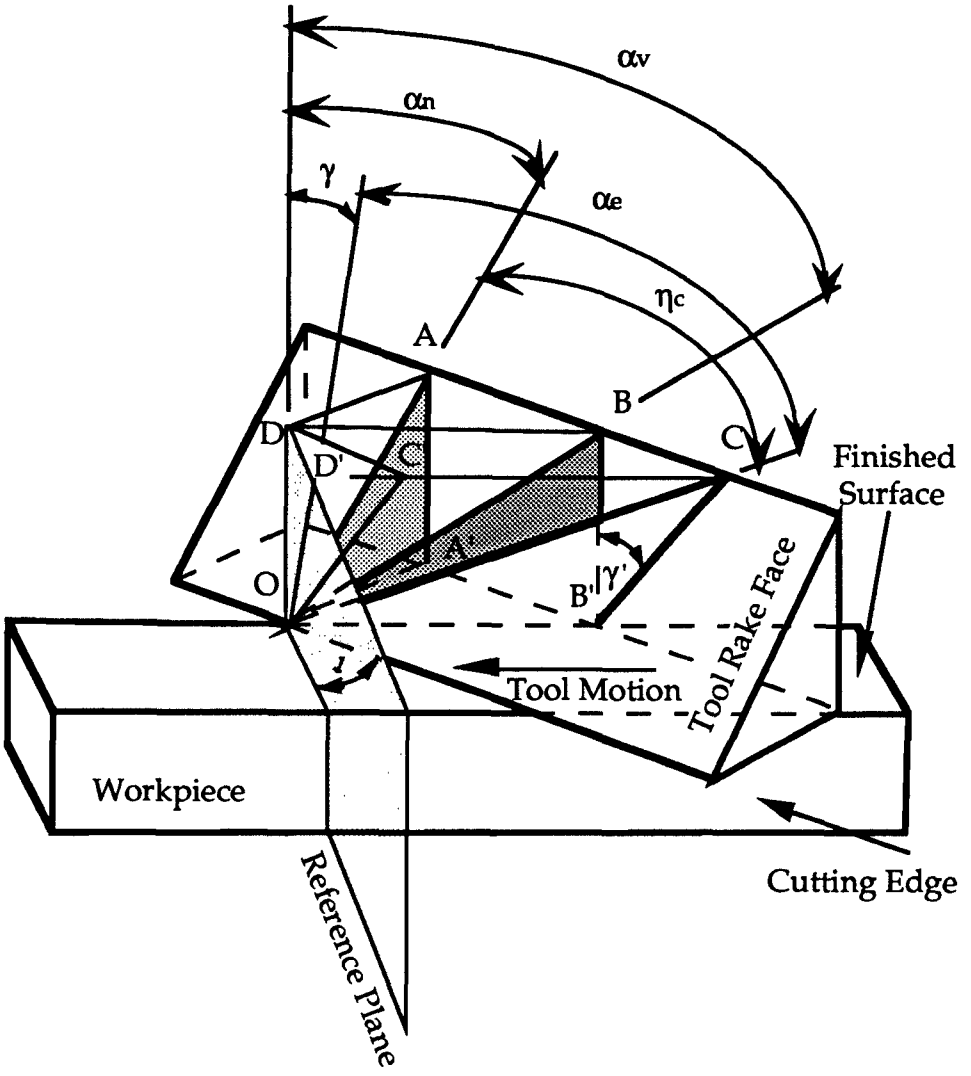

Figure 2.3. Three distinct rake angles in oblique cuttings.

$\angle$D'OC, is measured in the plane containing the chip flow direction and the cutting-velocity vector, which is the orthogonal cutting plane in oblique cutting processes. The relations between the three rake angles are given in the following equations [see Appendix A]:

$$\tan \alpha_n = \tan \alpha_v * \cos i \tag{2.1}$$

$$\sin \alpha_e = \sin \eta_c * \sin i + \cos \eta_c * \cos i * \sin \alpha_n \tag{2.2}$$

where η_c is the chip flow direction. Stabler [25] reported that ηc was approximately equal to the inclination angle i for a variety of tool and workpiece materials, rake angles, and speeds. Replacing the chip flow angle η_c by inclination angle i, Equation 2.2 becomes:

$$\sin \alpha_e = \sin^2 i + \cos^2 i * \sin \alpha_n \tag{2.3}$$

For complex tools such as a conventional lathe tool, a face-milling cutter or a twist drill, the effective rake angle should be adopted as the rake angle in the orthogonal cutting plane, where the resultant cutting force resides.

2.3.2 Cutting Force Models

In the first approximation of the cutting force study, it was assumed that the cutting force was proportional to the chip load [12,26]:

$$Fc=Ks*Ac=Ks*f*d=Ks*wd*u=Kc*u \tag{2.4}$$

where Ks is a proportionality coefficient, which is a function of workpiece material, tool geometry, and cutting conditions; Ac is chip load; f is feed rate; d is depth of cut; wd is width of cut; u is thickness of cut; and Kc is the cutting

stiffness. Later, Tobias et al. [27] introduced penetration rate and cutting speed variations into the cutting force equation 2.1 to give:

$$Fc=Kc*u + Kv*Vz + Kp*Vy \tag{2.5}$$

where Kv and Kp are proportionality coefficients, Vz is the cutting velocity, and Vy is the penetration rate. Smith and Tobias [24] also confirmed that the coefficient of penetration rate can be determined by the equation:

$$Kp=-Cp*Kc/n \tag{2.6}$$

where Cp is a penetration factor and n is a spindle speed. Zhang also proposed a tangential cutting force component to simulate the effect of tool motion in the tangential direction to the finished surface [34]. Equation 2.5 then becomes:

$$Fc=Kc*u + Kv*Vz + Kp*Vy + KtZ \tag{2.7}$$

where Kt is the proportionality coefficient and Z is the displacement of the cutting tool in the tangential direction.

Kronebergh proposed that the resultant cutting force consists of three components (p_1 p_2 and p_3) , which are proportionally related as follows:

$$Fc = \sqrt{p_1^2 + p_2^2 + p_3^2}$$

$$= p_1\sqrt{1+\left(\frac{k2}{k1}\right)^2+\left(\frac{k3}{k1}\right)^2}$$

$$= p_2\sqrt{\left(\frac{k1}{k2}\right)^2+1+\left(\frac{k3}{k2}\right)^2}$$

$$= p_3\sqrt{\left(\frac{k1}{k3}\right)^2+\left(\frac{k2}{k3}\right)^2+1} \tag{2.8}$$

where p_1=k1*f*d is the tangential force component,

p_2=k2*f*d is the radial force component,

p_3=k3*f*d is the feed force component, and

k1, k2, and k3 are the proportionality coefficients.

Equation 2.8 can be employed so that if any one of the three components is given, the resultant cutting force and the other components can be calculated by proportionality relations. This procedure enables the prediction of unmeasured cutting forces, such as the eliminated lateral cutting force of a rotating drill.

Alternatively, logarithmic proportional relations were developed and applied by Kronenberg [12]. The first equation, derived empirically, establishes a relation between cutting force, feed rate, and effective angle and has the following form:

$$R_n = C_n' * [\frac{80-\alpha_e(j)}{50}]^{nr} * f^{nf} \tag{2.9}$$

$$R_t = C_t' * [\frac{80-\alpha_e(j)}{50}]^{tr} * f^{tf} \tag{2.10}$$

where Rn and Rt are the cutting forces shown in Figure 2.2 (a) and C_n', nr, nf, C_t', tr, and tf are constants.

According to Zhang's research the relation between the cutting force and cutting speed can also be established by a logarithmic proportional relation of the form [34]:

$$R_n = C_n^{''} * (2 * \pi * r * n)^{nv} \tag{2.11}$$

$$R_t = C_t^{''} * (2 * \pi * r * n)^{tv} \tag{2.12}$$

where $C_n^{''}$, nv, $C_t^{''}$, and tv are constants.

2.4 Purpose of Study

The purpose of this thesis is to establish thrust and torque models of drilling processes for enlarging holes, based on varying geometry and cutting conditions. Such models are potentially useful in a global drilling process simulation for the prediction of tool motion and the generation of surface topography for a concurrent engineering design system. Such work is surely needed for meeting tolerance requirements, process planning, and system monitoring.

From the dynamic viewpoint, the proposed thrust and torque models should be able to reflect variations of the thrust and torque due to the change of the drill geometry, such as a larger point angle due to the drill wear at the point. Also, the performance of the drilling systems with regard to the operating parameters needs to be investigated. The following three aspects must be included in the thesis:

(1) The thrust and torque generation depends on the drill geometry, such as helix angle, point angle, web thickness, and radius, which is instrumental for tool design. The performance of the drill can be improved by designing drills to reduce thrust and torque. Also, thrust and torque variations may indicate drill point damage due

to tool wear, such as crater wear on a rake face, flank wear on a relief face, and wear at a drill point angle.

(2) The drilling force varies with the change of cutting parameters such as feed rates, spindle speeds and workpiece materials. A machine operator or process engineer selects the cutting parameters based on prediction from the models for a specific requirement, such as machining safety, noise pollution, maximum production, etc.

(3) The drilling force changes with the deflection of the drill structure. The dynamic thrust and torque can be related to the drill structures during the development of the thrust and torque models. Potentially, the developed thrust and torque models could deal with the stability of the drilling system with regard to operating parameters.

CHAPTER 3

THRUST AND TORQUE MODEL DEVELOPMENT

In this chapter, the basic methodology applied to model the thrust and torque during drilling is described. The methodology treats the thrust as the resultant cutting force of the two lips in the axial direction, and the torque is modeled as the moment of the force-couple of the two lips normal to the drill radius. The cutting force acting on each lip is modeled as a single-point tool engaged in an internal straight turning process. Similarities in geometry between lathe tools and drills are discussed. The variation of the cutting speed and the effective rake angle along the drill radius are considered as factors governing the cutting force distribution along the cutting edges. The resultant thrust and torque are obtained by integrating the distributed forces over the region where hole enlargement occurs. Empirical constants in the two models are obtained by a least squares analysis, based on the experimental data. Finally, chip formation during drilling processes is studied and related to the developed models.

3.1 Tool Geometry in Turning Processes

The American Standards Association (ASA) adopts a standard nomenclature to uniquely define the geometry of a lathe-tool. Figure 3.1 shows a representative lathe-tool and gives shorthand notation for specifying the relevant geometric features. These features include two rake angles (back and side), two relief angles (end and side), two cutting edge angles (end and side), and the nose radius.

In the machining industry, these seven parameters are very

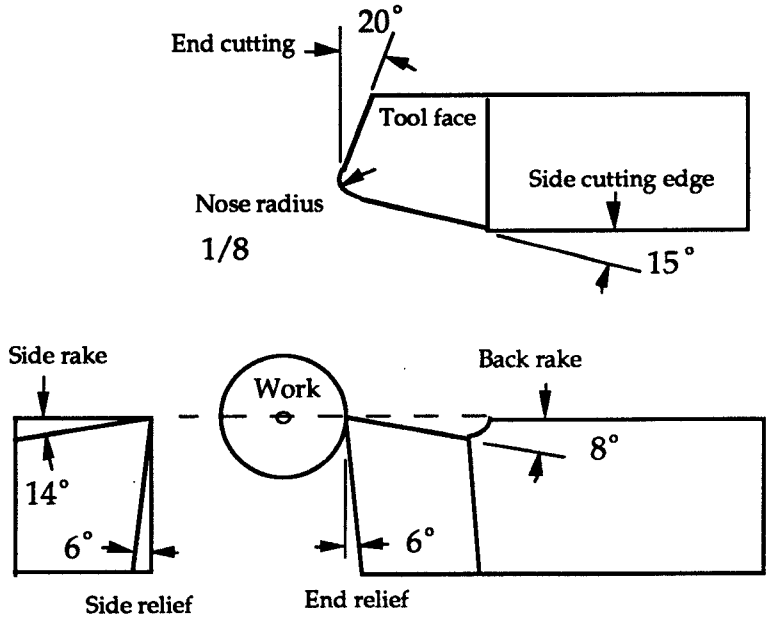

Tool Designation - 8, 14, 6, 6, 20, 15, 1/8,

- Back rake
- Side rake
- End relief
- Side relief
- End cutting
- Side cutting edge (Lead angle)
- Nose radius

Figure 3.1 Representative lathe-tool showing American Standards Association nomenclature (from [21]).

important. For example, a tool designer needs to specify these quantities, in order to carry out the desired manufacturing process. However, several additional parameters have received more attention in metal cutting research, such as the effective rake angle, normal rake angle, velocity rake angle, and inclination angle. Note that these angles are not independent; rather, they are determined when the prior seven geometric features have been specified. For example, the inclination angle defines the inclination of the tool face to a reference plane which is perpendicular to the cutting velocity vector. As shown in Figure 3.2, in the shank direction, the back rake angle, α_b, is visualized in a plane normal to the reference plane. In the direction normal to the shank direction, the side rake angle, α_s, is visualized in a plane normal to the reference plane. The rake angle is positive when the tool face is below the reference plane, (i. e. the tool lip is a sharp angle). Conversely, if the tool lip is a dull angle, the rake angle is negative. These two angles, together with the lead angle (or side cutting edge angle), Cs, determine the effective rake angle and inclination angle of the lathe tool, which are the most important angles to a machining engineer. The inclination angle, i, may be found in terms of the known side rake angle, back rake angle, and lead angle by:

$$\tan i = \tan \alpha_b * \cos Cs - \tan \alpha_s * \sin Cs \qquad (3.1)$$

The effective rake angle, α_e, shown in Figure 2.3 in Chapter 2, characterizes the cutting mechanism. This angle defines the angle at which the chip is deflected in the two dimensional cutting plane, as shown in Merchant's force circle of Figure 2.2 (a), and can be obtained by the following steps:

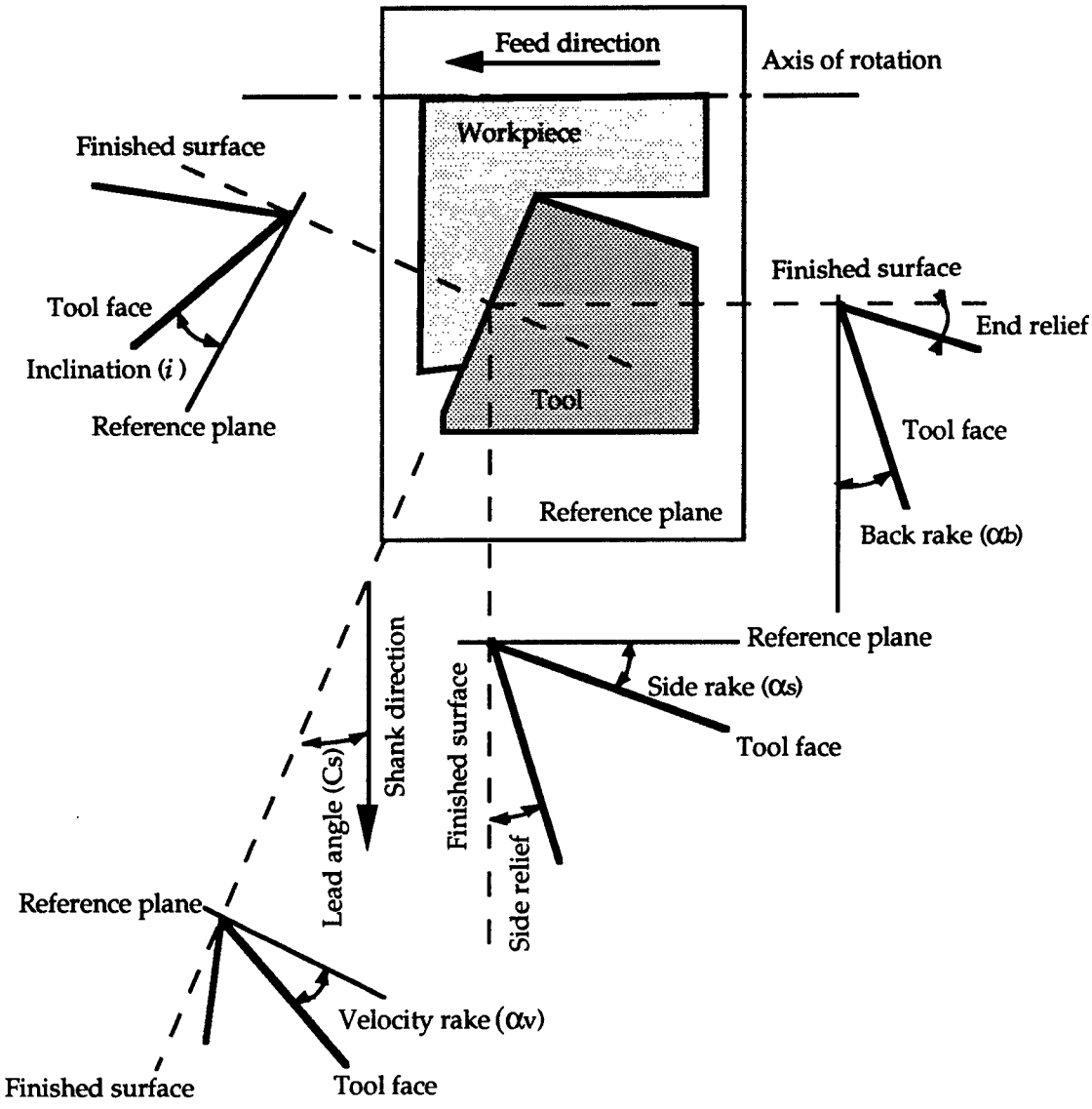

Figure 3.2 Tool geometry in turning processes.

(1) Calculate the velocity rake angle, α_v, (shown in Figure 3.2) from the given angles α_b, α_s and Cs.

$$\tan \alpha_v = \tan \alpha_s * \cos Cs + \tan \alpha_b * \sin Cs \quad (3.2)$$

(2) Calculate the normal rake angle, α_n, by using Equation 2.1.

(3) Calculate the effective rake angle, α_e, by using Equation 2.3.

3.2 Drilling Processes For Hole Enlargement

According to Kaczmarek's results [9], the thrust and torque generated during drilling are caused by three parts of a drill: the lips, margins and chisel edge. Two assumptions are made for the theoretical models of the drilling processes for hole enlargement. First, the thrust and torque are not caused by the chisel edge. The diameter of the existing hole in the workpiece is assumed to be larger than the chisel edge. Second, the thrust and torque are not caused by the margins. Drills are conically shaped with the larger diameter at the drill point, such that the margins will not be engaged in the cutting process. But in practice, the margins participate in the drilling operation due to lateral vibration of the drill. Theoretically, the drilling process can be phenomenologically treated as a pair of single-point, internal, straight turning processes, shown in Figure 3.3. During drilling, the drill rotates with respect to the fixed workpiece. Half of the difference between the diameters of the drill and the existing hole is equivalent to the depth of cut in the turning process. There are also several geometric features of the drill which are equivalent to the back rake angle, side rake angle, and lead angle of the lathe tool. The following equations provide the equivalent relations [21]:

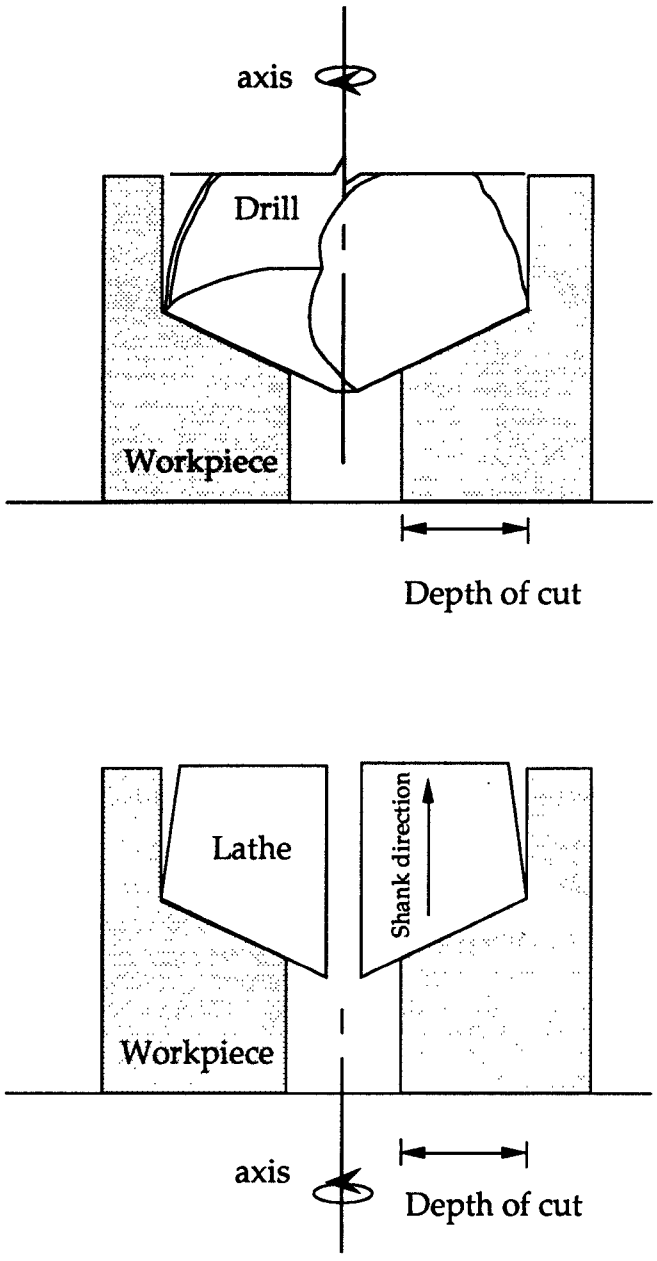

Figure 3.3 Comparison of a drilling process and a pair of internal straight turning operations.

Lathe-Tool	Drill	
side rake angle:	$\alpha_s = -\sin^{-1}(w/2r)$	(3.3)
back rake angle:	$\alpha_b = \tan^{-1}(2*\tan(\delta)*r/D)$	(3.4)
lead angle:	$Cs = p/2$	(3.5)

where w is the web thickness, r is the drill radius (a variable), δ is the helix angle at the radius r, D is the drill diameter, and p is the point angle. Equation 3.3 differs slightly from the form given in [21] for consistency within this thesis.

At points along the cutting edge of a drill, the side rake and back rake angles are functions of radius, as shown in Figure 3.4, and are measured with respect to the reference plane passing through the rotating axis of the drill at that point. By using Equations 3.1 to 3.5, the variations of side rake, back rake, normal rake, velocity rake, effective rake and inclination angles with radius r may be determined, as shown in Figure 3.4. The variations in this figure are for the drill used in the experiment, with diameter=11/16", helix angle=32^0, point angle=118^0, and web thickness=0.11". The inclination angle *i* increases as the center of the drill is approached, while the normal rake and velocity rake angles decrease and even assume large negative values. However, the effective rake angle does not become negative as a consequence of the large inclination angle near the drill point.

3.3 Force Aggregation Along Cutting Edges

To investigate the generation of the thrust and torque, it is helpful to first analyze the cutting force produced at an individual section, then

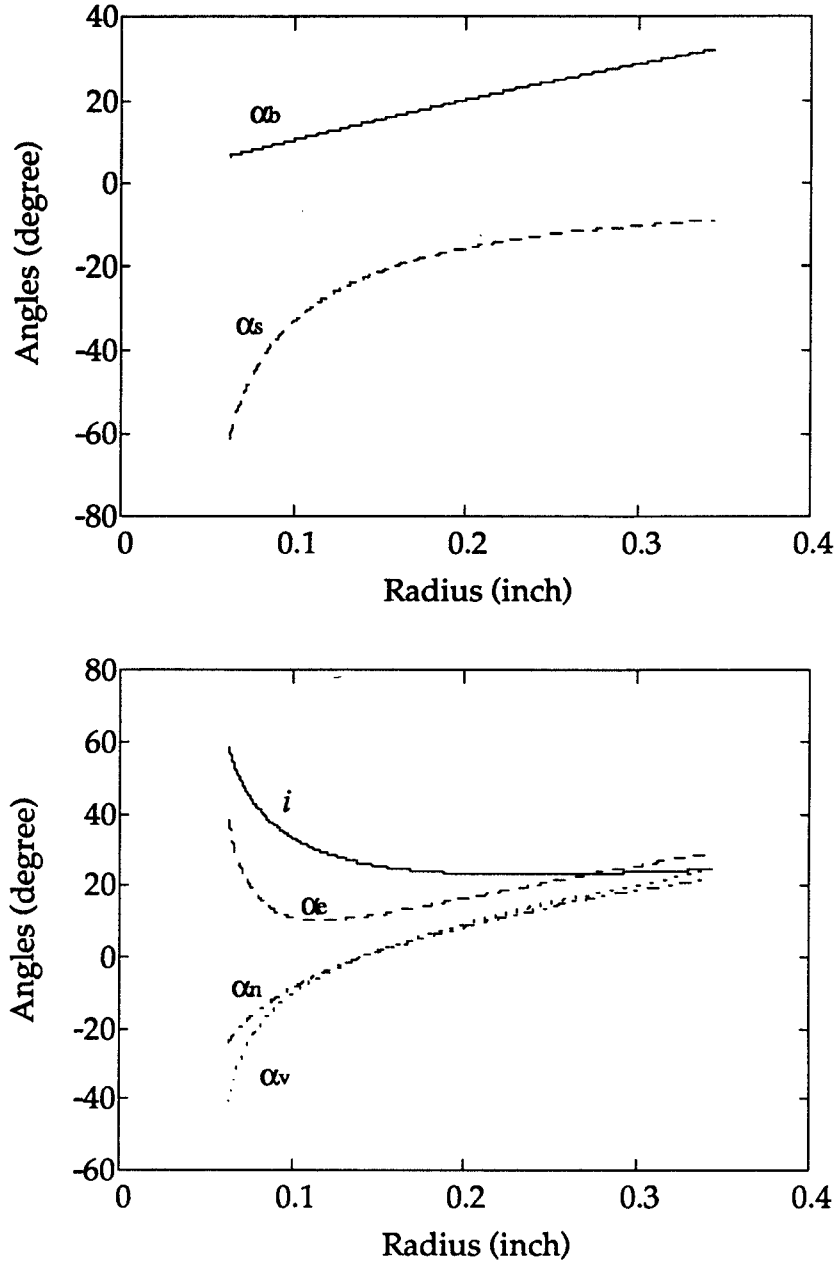

Figure 3.4 Variation of inclination and rake angles along drill radius.

decompose the local cutting force into incremental thrust and torque, and finally integrate these increments along the two cutting edges. The total thrust and torque are the results of the previous analysis. For analyzing the cutting force generated at a specific position, the cutting mechanism is treated as orthogonal cutting. The orthogonal cutting plane is defined as the plane containing the cutting force vector and the chip flow direction for the specific cutting section.

Along one cutting edge, the two cutting force components of the j^{th} section away from the center are formulated according to the following equations.

$$\Delta R_n(j) = C_n * (2 * \pi * j * \Delta r * n)^{nv} * [\frac{80 - \alpha_e(j)}{50}]^{nr} * f^{nf} * \Delta r \tag{3.6}$$

$$\Delta R_t(j) = C_t * (2 * \pi * j * \Delta r * n)^{tv} * [\frac{80 - \alpha_e(j)}{50}]^{tr} * f^{tf} * \Delta r \tag{3.7}$$

where C_n, nv, nr, nf, C_t, tv, tr and tf are constants. The forces on all sections engaged in drilling are summed to give the total thrust and torque through geometrical transformation. As shown in Figure 3.5, a split angle, γ, is defined such that the tangential force ΔR_t and normal force ΔR_n can be transformed to the X-Y-Z coordinates. The split angle is the projected angle on the reference plane between the two planes containing the velocity rake angle and effective rake angle. This angle is related to other important angles by the equation [see Appendix A]:

$$\tan(\gamma) = \tan(\eta_c) * \cos(i)/\cos(\alpha_n) - \sin(i) * \tan(\alpha_n) \tag{3.8}$$

Since, ηc is approximately equal to i, Equation 3.8 becomes

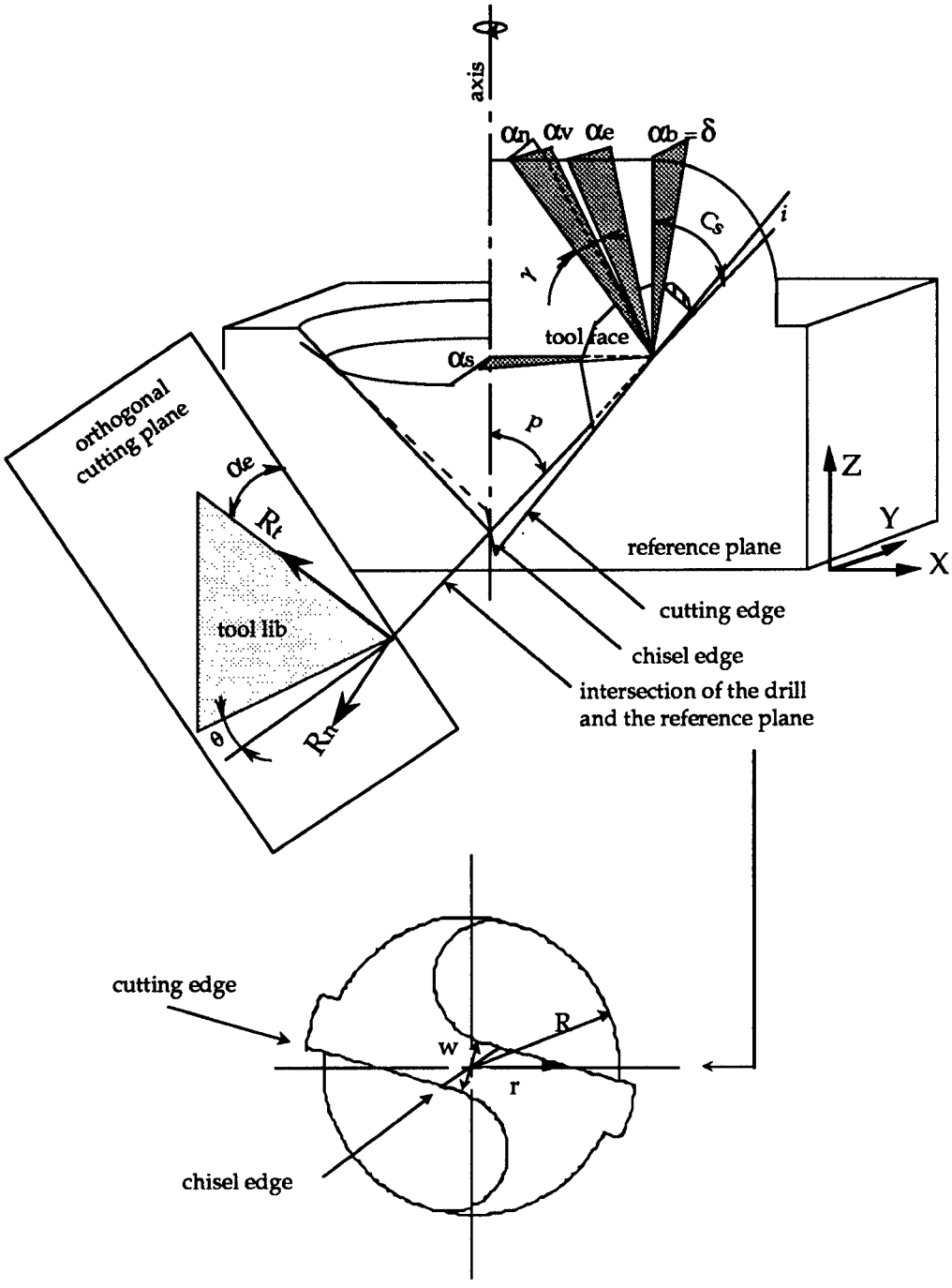

Figure 3.5 Orthogonal cutting plane in drilling processes.

$$\tan(\gamma) = \sin(i) / \cos(\alpha_n) - \sin(i) * \tan(\alpha_n) \tag{3.9}$$

The transformation in Equation 3.9 rotates ΔR_n and ΔR_t by an angle in the orthogonal plane so that the force components are either normal or tangential to the reference plane. The normal component, ΔF_y, produces the torque, and the component tangential to the reference plane gives an axial force, ΔF_Z, and a lateral force, ΔF_X. The lateral force will cancel with a symmetrical force component from the other cutting edge, but the axial force remains and is half of the thrust force. The cutting force described in X-Y-Z coordinates for the j^{th} section is

$$\begin{bmatrix} \Delta F_x(j) \\ \Delta F_y(j) \\ \Delta F_z(j) \end{bmatrix} = \begin{bmatrix} 0 & -\cos[Cs+\gamma(j)] \\ 1 & 0 \\ 0 & \sin[Cs+\gamma(j)] \end{bmatrix} \begin{bmatrix} \cos[\alpha_e(j)] & \sin[\alpha_e(j)] \\ -\sin[\alpha_e(j)] & \cos[\alpha_e(j)] \end{bmatrix} \begin{bmatrix} \Delta R_n(j) \\ \Delta R_t(j) \end{bmatrix} \tag{3.10}$$

The partial thrust, ΔTH, and partial torque, ΔTQ, are defined as

$$\Delta TH(j) = 2\Delta F_z(j) \tag{3.11}$$

$$\Delta TQ(j) = 2\Delta F_y(j) * j * \Delta r \tag{3.12}$$

By summing $\Delta TH(j)$ and $\Delta TQ(j)$ from the inner section, (j_{in}) to the outer section (j_{out}), the total thrust, TH, and torque, TQ, are calculated as

$$TH = \sum_{j_{in}}^{j_{out}} \Delta TH(j) \tag{3.13}$$

$$TQ = \sum_{j_{in}}^{j_{out}} \Delta TQ(j) \tag{3.14}$$

3.4 Determination of Constants and Numerical Simulation

In measurements of equal precision, the most probable values of observed quantities are those that render the sum of the squares of the errors a minimum. This theory is known as the principle of least squares. The constants in Equations 3.6 and 3.7 are determined by curve-fitting a set of experimental data using the method of least squares. Because the desired quantities, (ΔR_n and ΔR_t), cannot be directly measured, they must be inferred from measurements of thrust, TH, and torque, TQ, using the experiment presented in Chapter 5. There are also other intermediate quantities (ΔTH, ΔTQ, ΔFy, and ΔFz) that must be inferred to specify ΔR_n and ΔR_t.

The procedure for determining the unknown constants and numerical simulation is shown in Figure 3.6. The programs used for the curve fitting and the simulation were written by MATLAB commands and are listed in Appendix B. The determined constants for ΔR_n are: C_n=31.7134, nf=2.4649, nv=-1.8816, and nr=-5.9602; the ones for ΔR_t are: C_t=17.4092, tf=1.2251, tv=-0.8843, and tr=-4.6777. By substituting the calculated constants into the mathematical thrust and torque models and importing the test conditions, feed rate 0.0015 inch/rev and spindle speed 325 rpm, the parameters $\Delta R_n/\Delta r$, $\Delta R_t/\Delta r$, $\Delta Fy/\Delta r$, and $\Delta Fz/\Delta r$ are plotted as a function of radius in Figures 3.7 to 3.10. The figures include both theoretical predictions and experimental data. It should be pointed out that ΔR_n and ΔR_t increase dramatically when the drill center line is approached. The ΔFz term does not increase near the center due to the geometrical transformation. Although the ΔFy term increases dramatically near the center, the torque will not increase very much due to the smaller radius. By integrating the partial components along the cutting edges engaged in cutting processes, the resultant thrust and torque can be calculated.

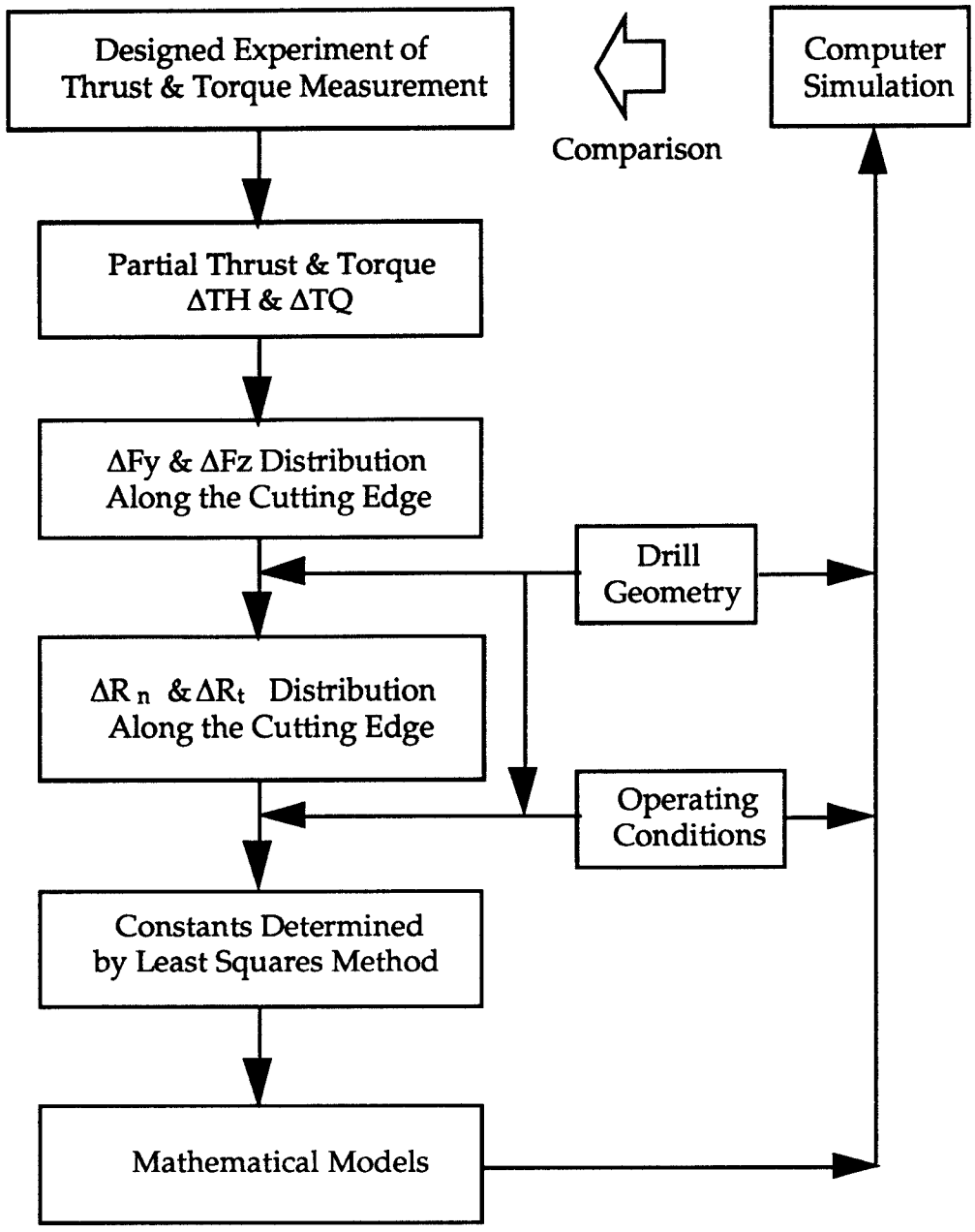

Figure 3.6 Procedure for determining constants and computer simulation.

Spindle Speed 325 rpm

Feed Rate 0.0015 in/rev

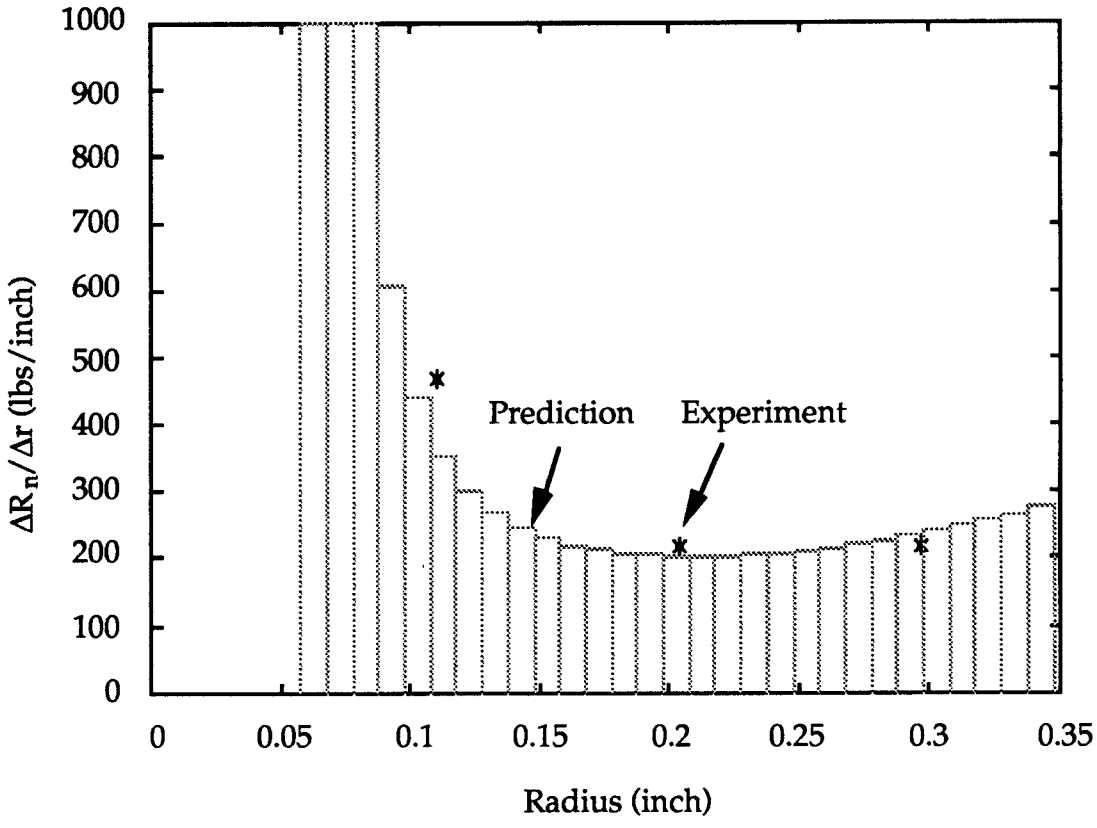

Figure 3.7 Mathematical prediction and experimental results of $\Delta R_n/\Delta r$ along radius.

Spindle Speed 325 rpm

Feed Rate 0.0015 in/rev

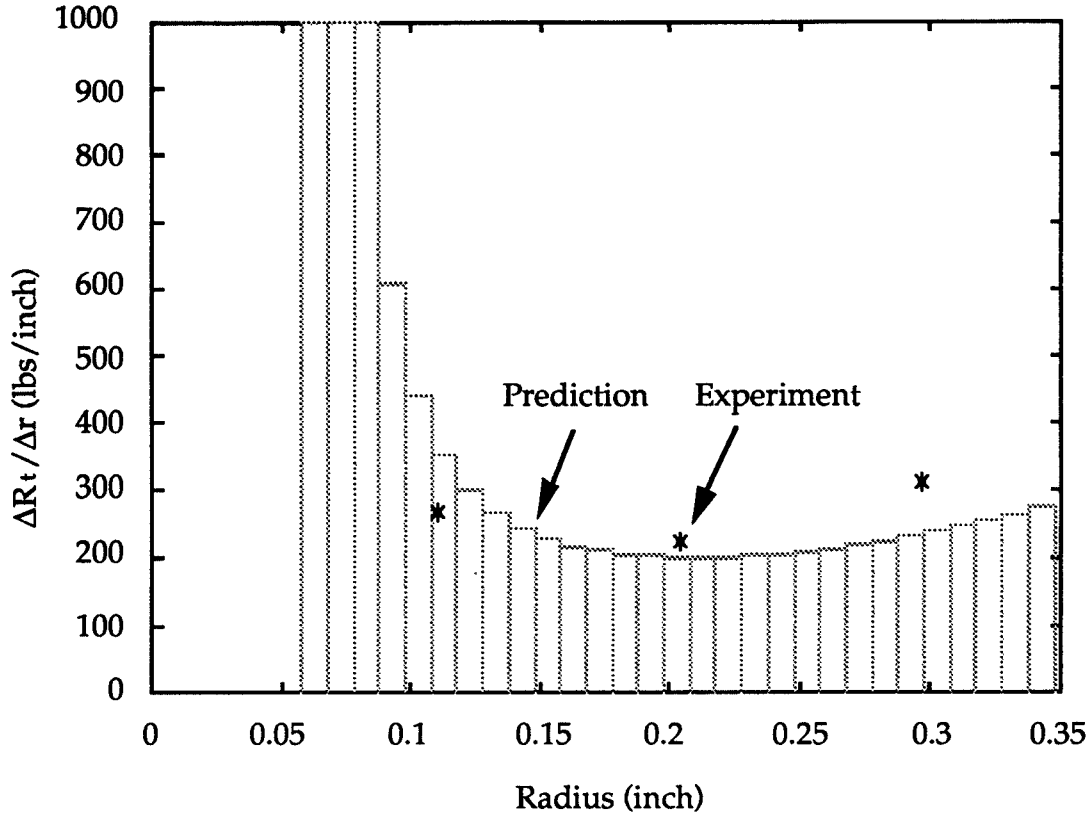

Figure 3.8 Mathematical prediction and experimental results of $\Delta R_t/\Delta r$ along radius.

Spindle Speed 325 rpm

Feed Rate 0.0015 in/rev

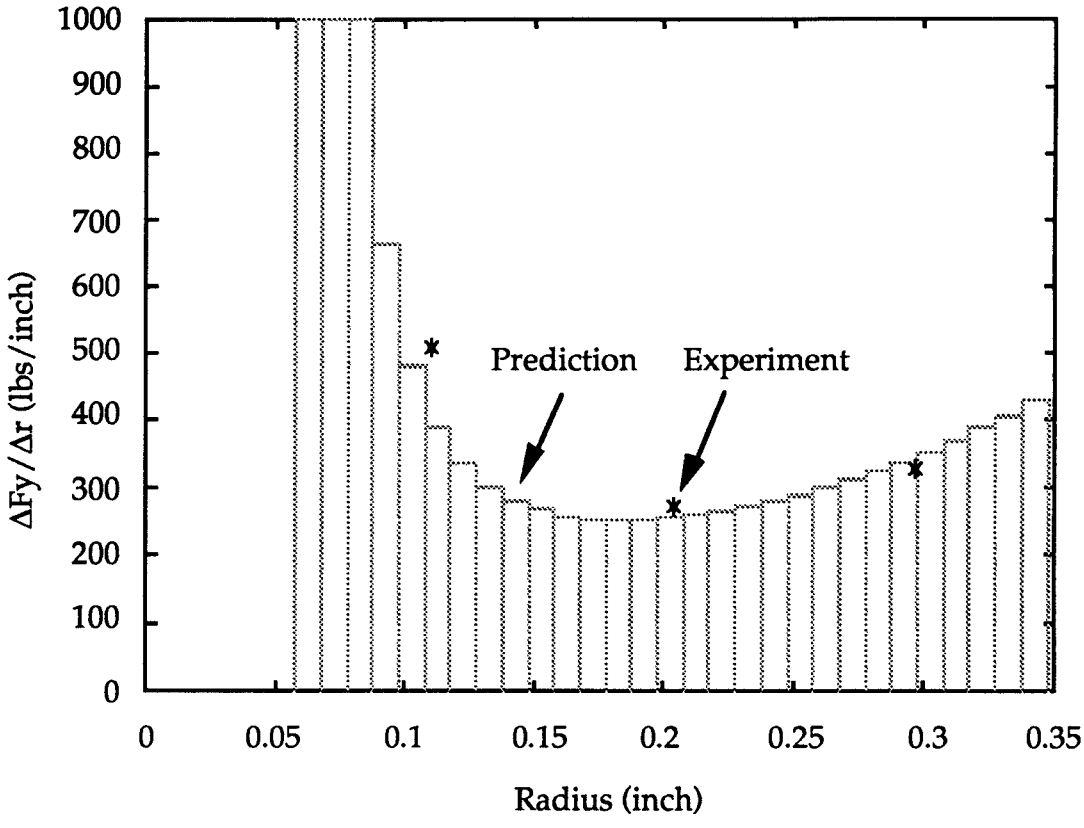

Figure 3.9 Mathematical prediction and experimental results of ΔFy/Δr along radius.

Spindle Speed 325 rpm

Feed Rate 0.0015 in/rev

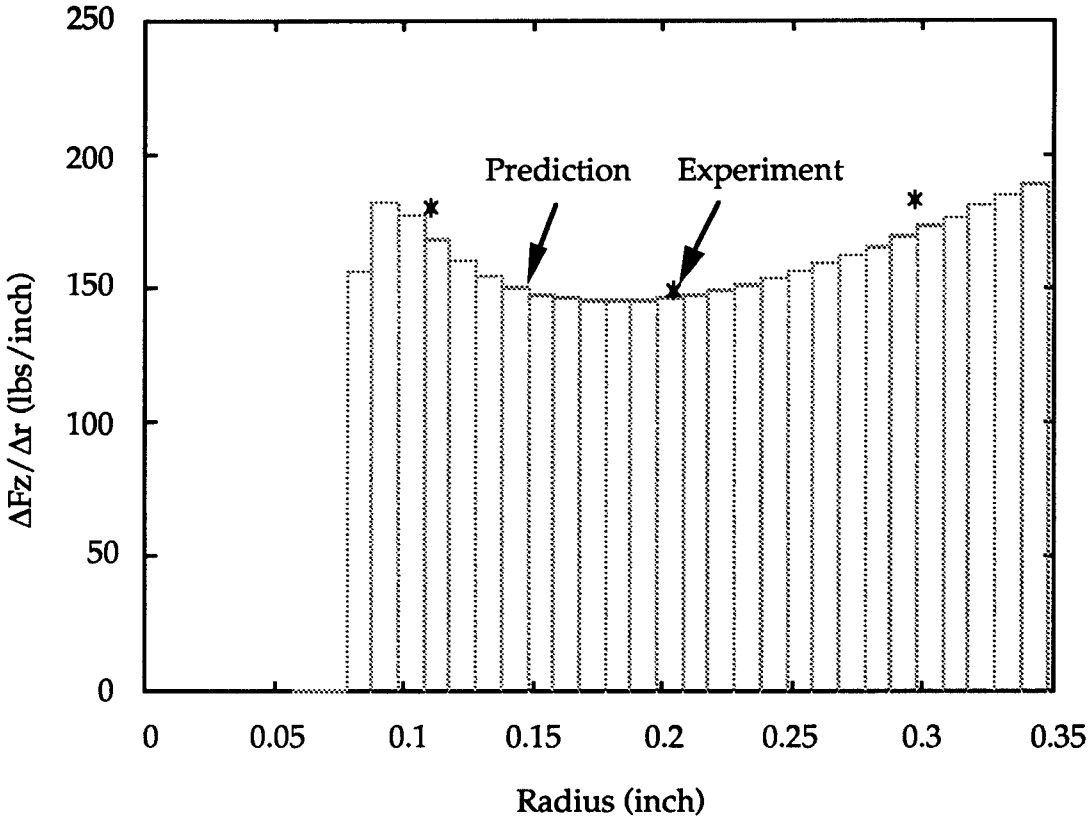

Figure 3.10 Mathematical prediction and experimental results of ΔFz/Δr along radius.

The integrated thrust and torque between radii 0.34375" and 0.025" are 32.1 lbs and 19.7 inch-lbs, which are close to the experimental data, 34.3 lbs and 18.4 inch-lbs. The ones between radii 0.34375" and 0.15625" are 60.0 lbs and 29.7 inch-lbs, which are close to the experimental data, 62.2 lbs and 28.7 inch-lbs, too. However, the integration between radii 0.034375" and 0.0625" fails to predict the resultant thrust and torque precisely, (excremental 96.0 lbs and 39.2 inch-lbs with predicted 29.1 lbs and 50.3 inch-lbs). This is mainly because of the complicated cutting mechanism near the center of drills. Beside the oblique cutting mechanism, there are indentation actions occurring in the region near the center of drills.

3.5 Chip Form of the Drilling Processes

Metal cutting processes are actually processes of chip production. Almost all the cutting energy is consumed in chip production, and most of the information for evaluating the cutting operation, such as surface finish, tool life, and cutting forces, are closely related to the chip geometry. Because of the twisted rake face and the limited space for chip flow, the drill chip formation is a complicated process. Chip formation in drilling processes is governed by the following three points [18]:

(1) The rake faces of a twist drill are not flat but twisted, and the rake angle varies along the cutting edges. This situation is not the case in other cutting tools. The twisted rake face gives the chip a rotation, ω_c, on the axis of twist drill, as shown in Figure 3.11.

(2) The cutting speed varies in proportionally with the distance from the drill center, which causes a strong side curling, or large ω_z, as

indicated with a dotted line in Figure 3.11. The non-uniform distribution of the rake angle along the cutting edge also contributes to the side curling, but not so strongly.

(3) The greatly side curled chip is forced to curl in another direction by the obstruction of the web and flutes of the drill. This action gives the chip a large ω_x.

Given the three components of angular velocity ω_c, ω_z, and ω_x, the chip experiences a helical motion with the angular velocity ω_h, which is the resultant of these three angular velocity components. After the chip clears both the web and flutes, $\omega_c << \omega_x$, the direction of ω_h, or the axis of helix, makes a larger angle with the drill axis. These actions produce a conical helical chip is produced, as shown in Figure 3.11.

As the drilling process progresses, the weight of the chip increases constantly and the center of gravity goes away from the root of the chip. The chip flow gradually becomes impeded by the web and flutes, which produces a resistance force on the chip. This force develops a bending moment, or

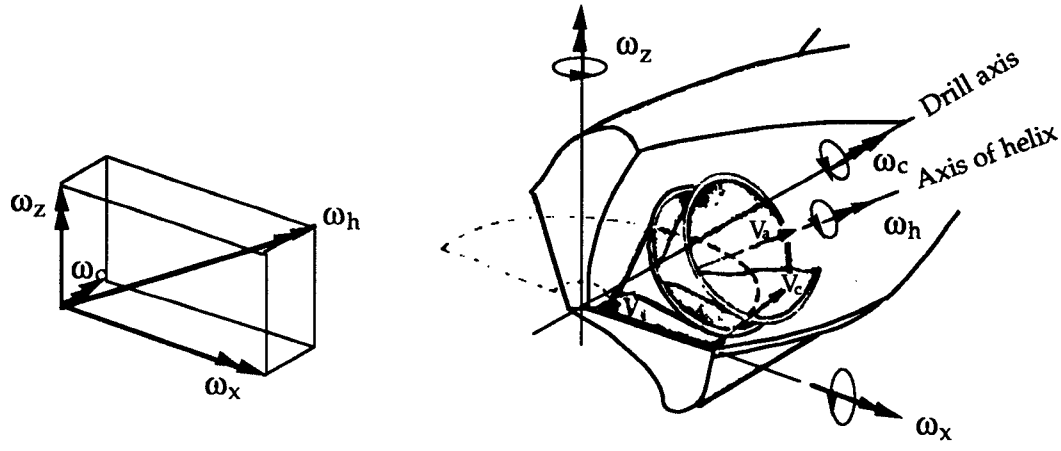

Figure 3.11 Conical helical chip produced by a twist drill (from [18]).

non-uniform stress distribution, at the root of the chip, which causes unstable or fragmented chips. The fragmentation acts to decrease the bending and the resistance force. In other words, the chip changes its form to meet the external force and the constraints governing its flow.

The resistance force acting on the chip contributes to the total thrust and torque on the drill. From the mean value point of view, this effect can be simulated as empirical constants in the thrust and torque modeling. The constants are functions of the properties of the web and flutes and are determined experimentally. Theoretically, there are no problems with chip disposal, (i.e. the thrust and torque can only be measured during the period when the chips are flowing out freely).

CHAPTER 4

DRILL STRUCTURE IDENTIFICATION

During drilling, the drill is fastened rigidly at the shank and is subjected to cutting forces distributed along its two cutting edges. A cutting force component in the lateral direction can be introduced during drilling when the cutting forces of the two cutting edges are not symmetrical. This lateral force component may cause the lateral vibration of the drill, which is the degree of freedom with the lowest natural frequency of the structure. The dynamic characteristics of the drill in the lateral direction are investigated in this chapter. The natural frequencies, damping ratios and mode shapes of the drill structure are identified through modal testing.

4.1. Methodology

Modal testing is the collection of techniques for planning, testing, data acquisition and data reduction of a dynamic test in order to estimate the system modal parameters. The collected data from the dynamic test is the frequency response, the ratio of the structural response to the excitation force in the frequency domain. The excitation may be a periodical signal of a certain frequency span or an impulse, and the response is the motion of the structure, displacement, velocity, or acceleration. These well-known frequency responses are receptance, mobility and inertance, which are the ratios of the output harmonic displacement, velocity, and acceleration to the input harmonic forces in frequency domain respectively. For example, the receptance of a multi degree of freedom system, with input at the k^{th} station and output at the j^{th} station, is [see Appendix C]:

$$R_{jk}(\omega) = \frac{x_j}{F_k}(\omega) = \sum_{r=1}^{n} \frac{{}_rA_{jk}}{\omega_r^2 - \omega^2 + i\eta_r\omega_r^2} = \sum_{r=1}^{n} \frac{\phi_{jr}\phi_{kr}}{\omega_r^2 - \omega^2 + i\eta_r\omega_r^2} \tag{4.1}$$

where ${}_rA_{jk}$ is the modal constants of the r^{th} mode, and ϕ_{jr} is the mass normalized mode shape of the j^{th} station of the r^{th} mode. Ewins stated that in the vicinity of a resonance, the total response is dominated by the contribution of the mode whose nature frequency is the closest [6]. The parameters can be extracted in the vicinity of the resonance based on a single degree of freedom system model. The receptance of the r^{th} mode is:

$${}_rR_{jk}(\omega) = \frac{{}_rA_{jk}}{\omega_r^2 - \omega^2 + i\eta_r\omega_r^2} \tag{4.2}$$

It can be shown that the receptance can be graphically represented by an exact circle with a radius ${}_rA_{jk}/2\omega_r{}^2\eta_r$, and center at (0, $-{}_rA_{jk}/2\omega_r{}^2\eta_r$) in a polar plot [see Appendix D]. It should be noted that the modal circle will rotate and translate due to the contribution of the amplitudes and phase angles of other modes and will be reflected about the real axis by a negative sign of the modal constant. In the present study, the circle-fit method is used rather than the peak-amplitude method to avoid overestimating or underestimating damping factors and modal constants in the case of close-mode structures [6].

The relations between modal circle properties and some variables are defined as shown in Figure 4.1. The values of the receptance are complex values with real and imaginary parts, implying the information of the magnitudes and the phase angles. The information of the frequency at any specific point is not shown in the polar plot, but recorded by other corresponding data. The center, the diameter, and the maximum receptance

can be identified by fitting the experimental data with a circle. The modal parameters are related to circle properties and the variables by the Equations 4.3 to 4.5 [see Appendix E].

$$\omega_r = \omega_{Max(|_rR(\omega)|)} \tag{4.3}$$

$$\eta_r = \frac{\omega_a^2 - \omega_b^2}{\omega_r^2} \frac{1}{\tan(\frac{\theta_a}{2}) + \tan(\frac{\theta_b}{2})} \tag{4.4}$$

where $\frac{\theta_a}{2} = \sin^{-1}(\frac{|R_a -_r R|}{D})$ and $\frac{\theta_b}{2} = \sin^{-1}(\frac{|R_b -_r R|}{D})$

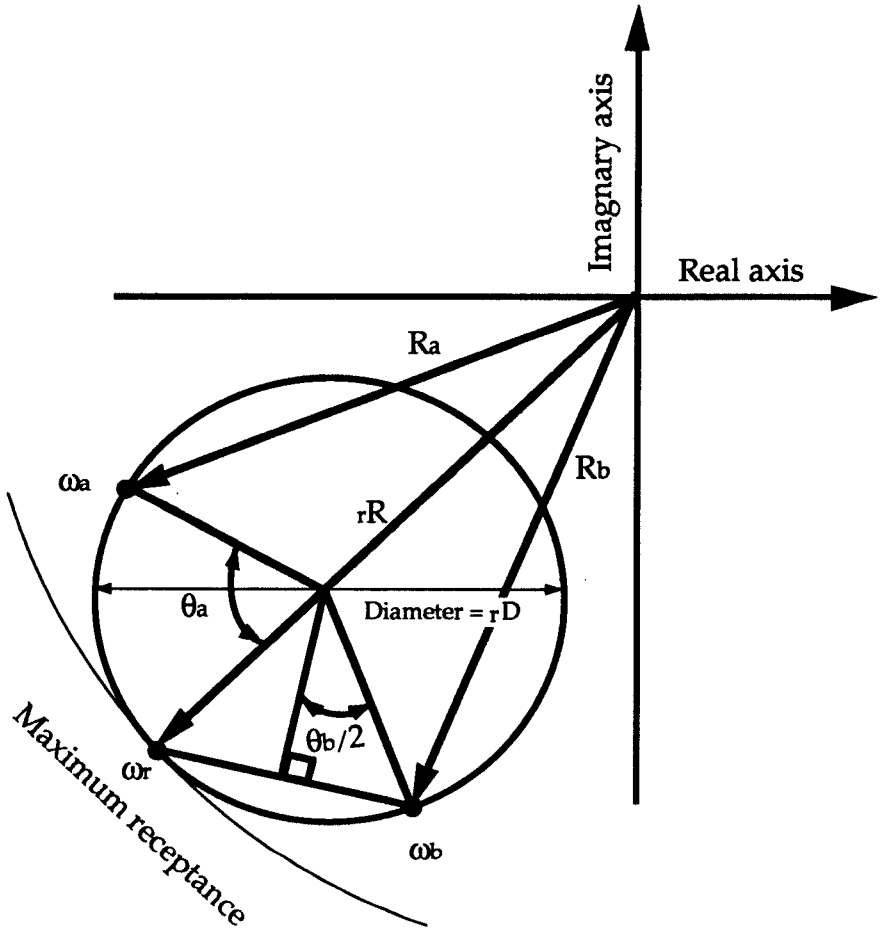

Figure 4.1 Modal circle and parameters.

$$_rA = +_rD\eta_r\omega_r^2 \qquad \text{(resonance below the real axis)}$$

or $$_rA = -_rD\eta_r\omega_r^2 \qquad \text{(resonance above the real axis)} \tag{4.5}$$

For a single frequency response measurement R_{jk} at the j^{th} station with the k^{th} input, the parameters, ω_r, η_r, and $_rA_{jk}$ of the r^{th} mode are obtained by applying the circle-fit method near the r^{th} peak. In order to identify mode shapes of a system with N stations, N frequency response are needed. They are one point frequency response, with input at the k^{th} station, output at the k^{th} station, and (N-1) transfer frequency response, with input at k^{th} station, output at the other stations. The mode shapes of the r^{th} mode and j^{th} station is calculated from modal constants as follows.

If k=j (point measurement)

$$\phi_{jr} = \phi_{kr} = \sqrt{_rA_{jj}} = \sqrt{_rA_{kk}} \tag{4.6}$$

If k ≠ j (transfer measurement)

$$\phi_{jr} = \frac{_rA_{jk}}{\sqrt{_rA_{kk}}} \qquad \text{or} \qquad \phi_{kr} = \frac{_rA_{jk}}{\sqrt{_rA_{jj}}} \tag{4.7}$$

4.2 Experiments and Data Analysis

4.2.1 Experiments

Three structures are identified. As shown in Figure 4.2, they are a solid steel bar with circular cross section, a steel bar with two straight flutes, and the twist drill mentioned in Chapter 3. Seven stations are equally arranged along each of the three structures. The excitation to the structure is arranged at the tip, station 7, such that the magnitude of the response will be

the largest, and the fundamental mode will be more precise than elsewhere. A sensor is arranged at one of the seven stations at a time. At least seven measurements for each different station are recorded for the mode shape identification.

The instruments used to do the modal testing are listed in Table 4.1. They are connected as shown in Figure 4.3. The generated impulse by the hammer at station 7 of the structure and the measured acceleration by the accelerometer are recorded by the analyzer. The measured inertance is the ratio between the former and the later calculated by the analyzer. In order to keep the precise locations of the stations along the structure, a rule with seven holes arranged the same as the stations of the structure is made. The accelerometer is affixed at station 1 while measuring the transfer frequency response. Then the accelerometer is affixed at station 2 through 7 to complete the minimum number of measurements for mode shape identification. The data is saved in an HP computer, and will be transformed to PC format for further calculation and modal analysis. The experiments are performed in the vibration laboratory, Department of Mechanical Engineering, University of Maryland, College Park.

Recorder:	Hewlett-Packard 3562A dynamic signal analyzer to record the excitation and response signals and output frequency response data.
Exciter:	a hammer with suitable tip hardness and mass to generate an impulse of a frequency span up to 5 kHz.
Sensor:	an accelerometer to measure acceleration
Fixture:	a chuck to hold structures which is fixed on a heavy base.

Table 4.1 Instruments for modal testing.

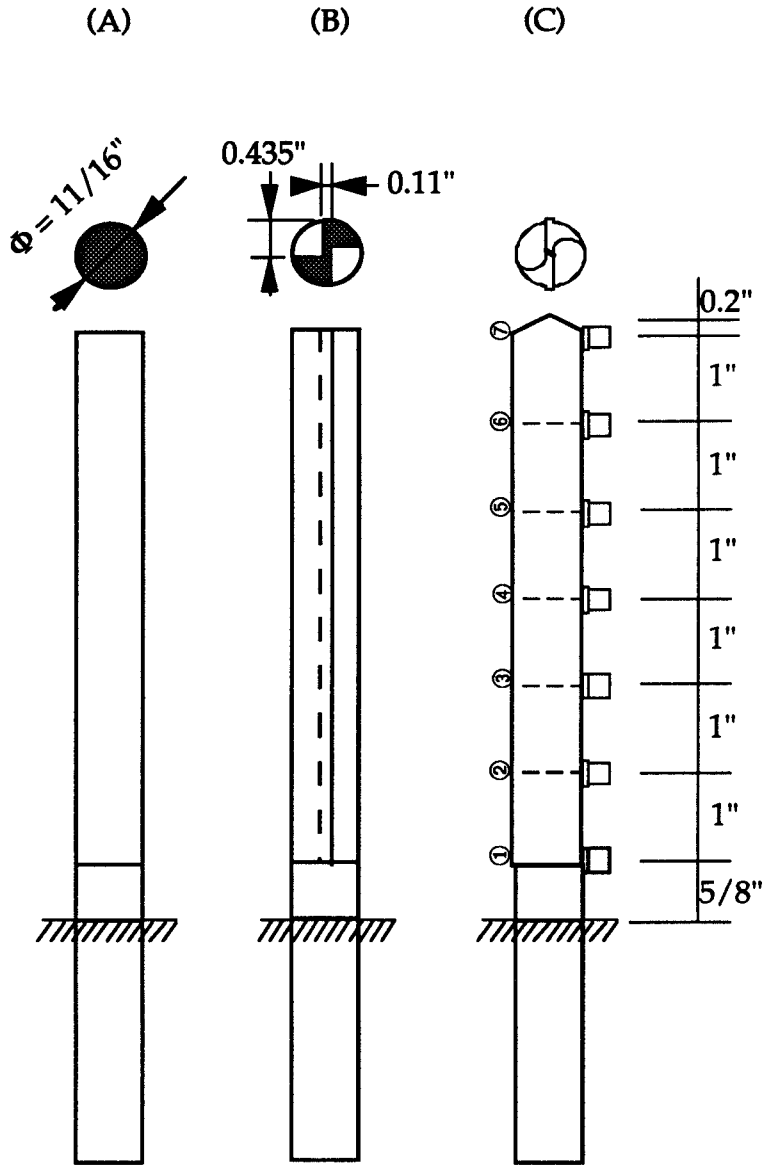

Figure 4.2 Dimension of the tested structures.

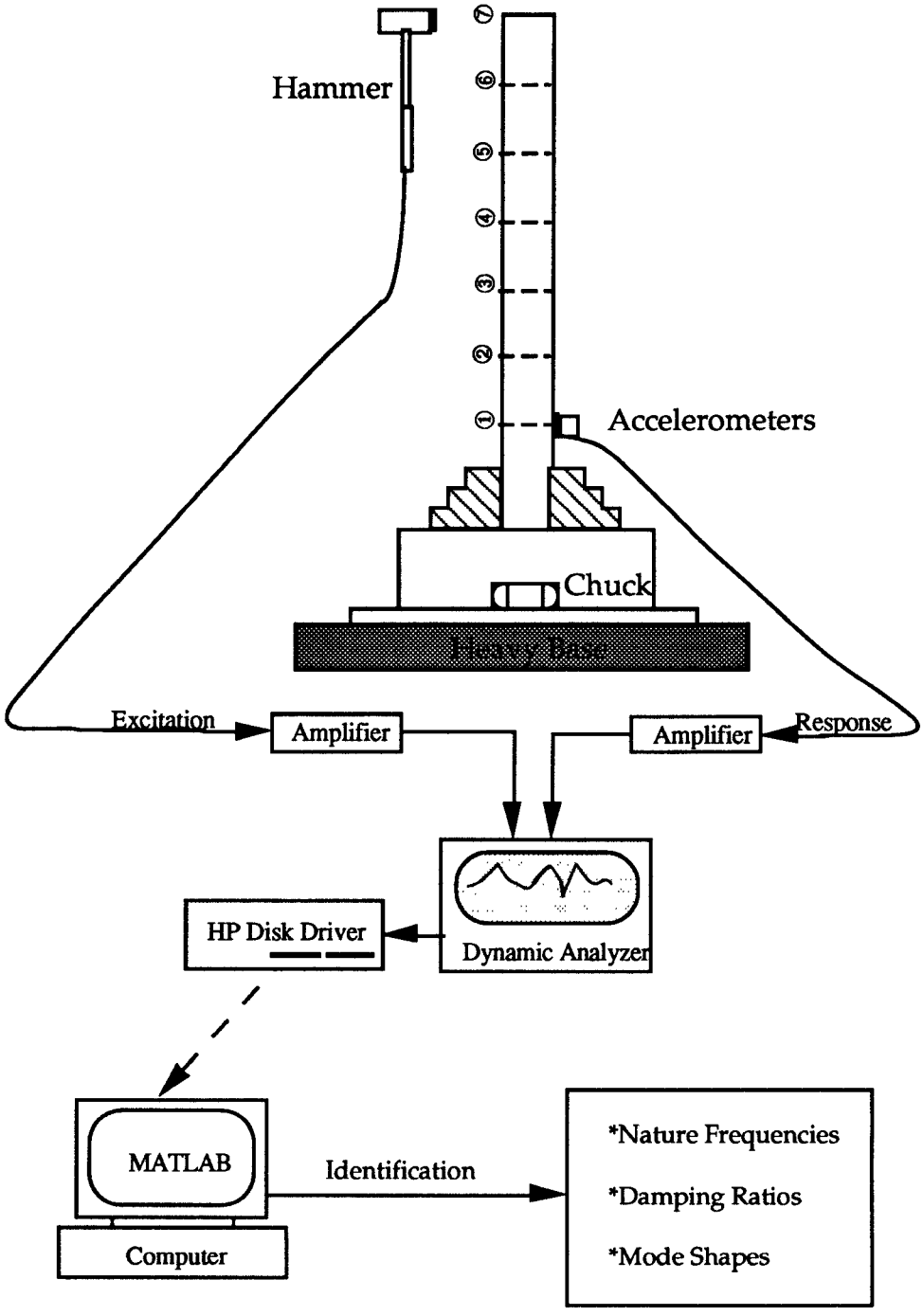

Figure 4.3 Experimental setup for modal testing.

4.2.2. Data Analysis

Theoretically, receptance of a structural damped system is an exact circle in a polar plot. In order to apply the circle-fit method, the first step is to transform the collected experimental inertance to receptance by dividing the former by $-\omega^2$. Figure 4.4 shows the semi-log plot of the measured inertance at station 1 of the case (A) solid bar and the polar plot of the receptance of the first peak, the second peak, and the third peak. The absolute peak values of the measured inertance are 0.2698, 1.7922, and 0.4975 and the ones of the transformed receptance are -0.5292×10^{-7}, 0.913×10^{-8}, and 1.94×10^{-9}. The latter are obtained by being respectively divided by the square of their frequencies in radial units.

Secondly, the circle-fit method is applied for every peak and for every single receptance measurement. There are measurements at the seven stations of the structure as shown in Figure 4.2. And for each measurement, there are three or two peaks for each single receptance within the excitation frequency range. The receptance in the frequency range of the vicinity of a peak is chosen to represent the receptance of a single degree of freedom system model for applying the circle-fit method. The range should be small but the total number of data should be large to get a better fitting confidence. The program performing the circle-fit method is written with MATLAB commands and is shown in Appendix F. Also the measured inertance signals at different stations are plotted on a semi-log scale, as shown in the appendix. Once the properties of the modal circle are identified, the modal parameters can be obtained by applying Equation 4.3 to 4.5. The redundant natural frequencies and damping ratios, obtained through point

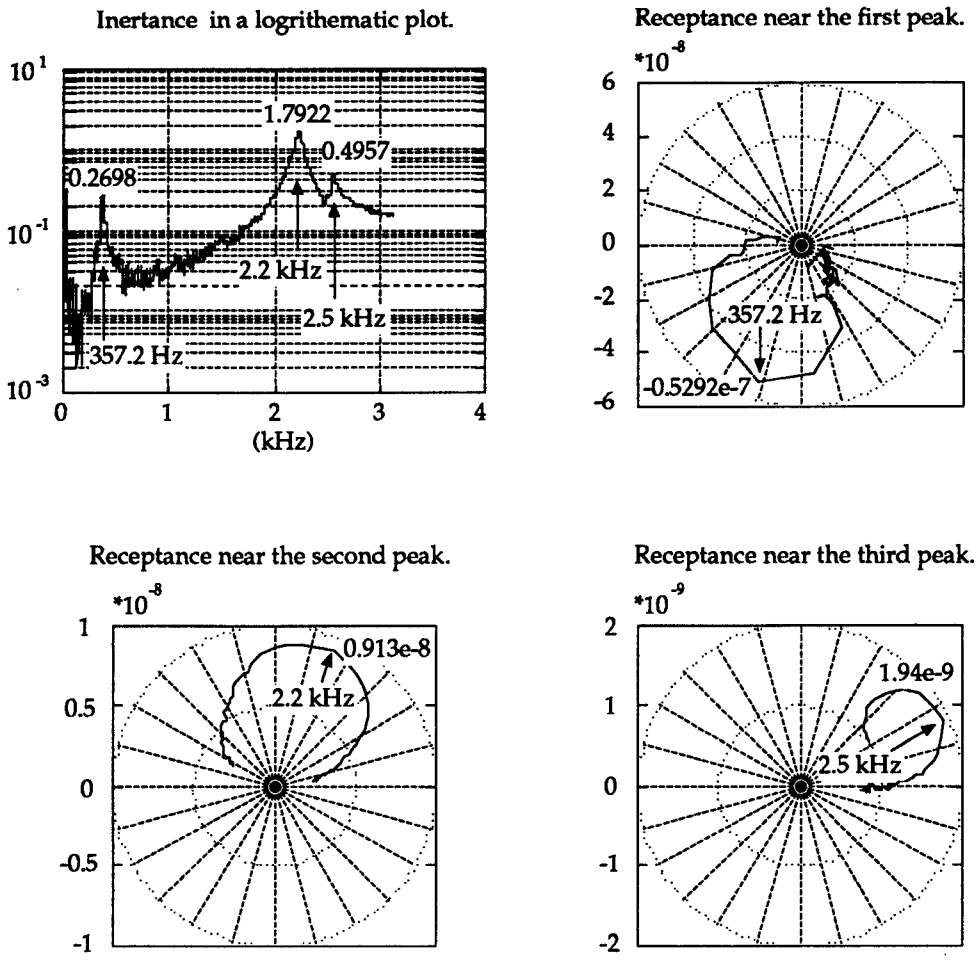

Figure 4.4 The measured inertance of the case (A) at station 1 and the transformed receptance near the three peaks for circle fit.

measurement or transfer measurements, can be averaged to get mean values.

4.3 Results and Discussion

The identified parameters are presented and the system response will be predicted and discussed in this section. The averaged natural frequencies and damping ratios for the three structures are shown in Table 4.2 and 4.3. The mode shapes for the three cases are plotted in Figure 4.5.

Natural frequencies \ Cases	(A) Solid bar	(B) Bar/flutes	(C) Drill
First mode $\omega 1$	357.2 Hz	283.0 Hz	333.1 Hz
Second mode $\omega 2$	2222.1 Hz	415.8 Hz	1688.0 Hz
Third mode $\omega 3$	2549.1 Hz	1629.5 Hz	not available

Table 4.2 The identified natural frequencies of the three structures.

Damping ratios \ Cases	(A) Solid bar	(B) Bar/flutes	(C) Drill
First mode $\eta 1$	0.05	0.03	0.03
Second mode $\eta 2$	0.03	0.06	0.03
Third mode $\eta 3$	0.01	0.02	not available

Table 4.3 The identified damping ratios of the three structures.

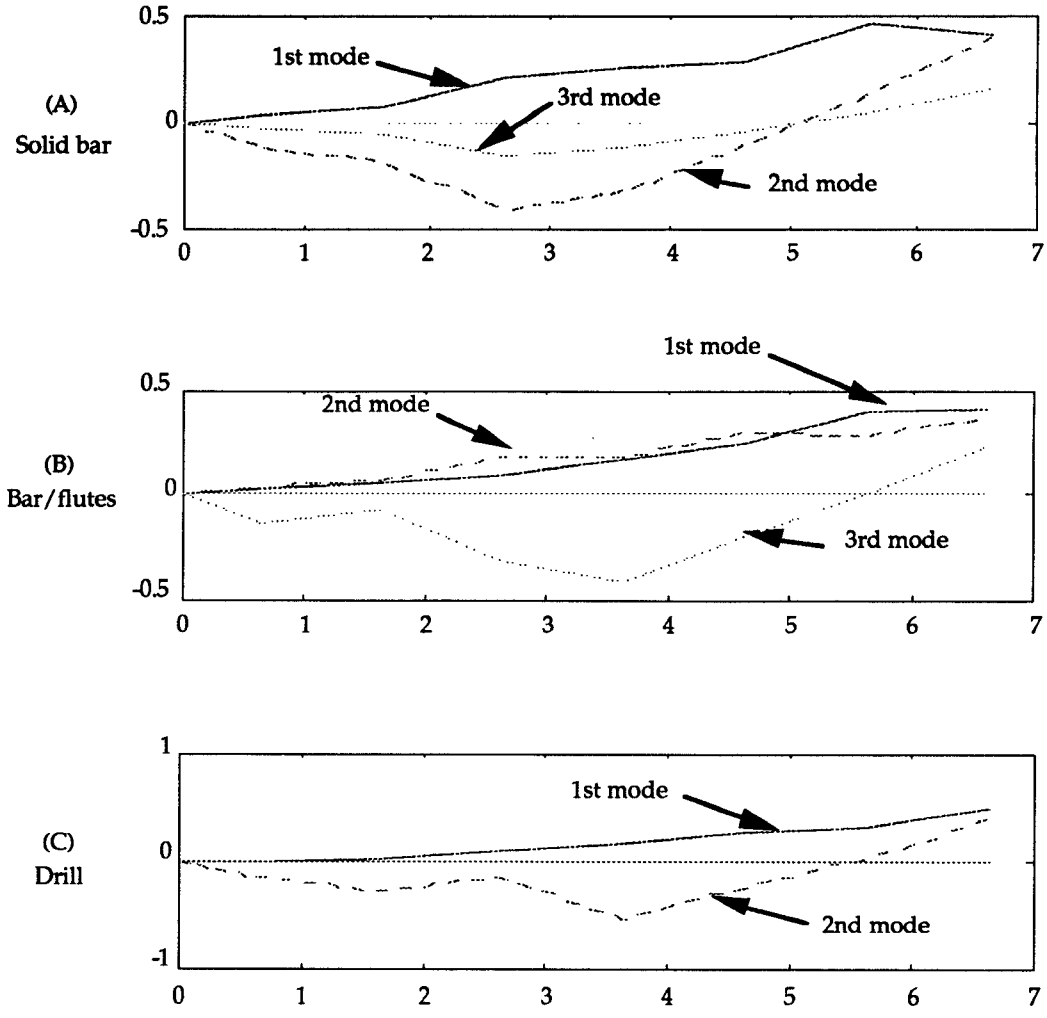

Figure 4.5 The identified mode shapes of the three structures.

Based on the identified modal parameters and the established modal space, the spatial response of the system is easy to be obtained. As a periodical input force , $\vec{F}e^{i\omega t}$, is applied to the structure, the output response, $\vec{x}(t)$, is

$$\vec{x}(t) = [\phi]\left[\frac{e^{i\omega t}}{\omega_r^2 - \omega^2 + i\eta_r\omega_r^2}\right][\phi]^T\vec{F} \tag{4.8}$$

where $\vec{x}(t)$ is the displacement at the seven stations of the structure, and $[\phi]$ is the mode shape matrix. The impulse response of the tip, (i.e. station 7), can be obtained by:

$$x(t) = \frac{\phi_{71}^2}{\omega_1^2}e^{-\frac{\eta_1}{2}\omega_1 t}\sin(\omega_{d1}t) + \frac{\phi_{72}^2}{\omega_2^2}e^{-\frac{\eta_2}{2}\omega_2 t}\sin(\omega_{d2}t) + \frac{\phi_{73}^2}{\omega_3^2}e^{-\frac{\eta_3}{2}\omega_3 t}\sin(\omega_{d3}t)$$

where $$\omega_{dr} = \omega_r\sqrt{1-(\frac{\eta_r}{2})^2} \tag{4.9}$$

By taking the second derivative of the displacement, and plotting the acceleration with respect to time, the predicted and the experimental data are compared in Figure 4.6. The two plots show satisfactory modal parameter identification. It should be noticed that the response after 0.07 seconds is dominated by the first mode only. The participation the r^{th} mode is about inversely proportional to the square of its natural frequency, ω_r^2. In the case of the drill, the participation of the first mode is about 25 times that of the second mode. It is hard to tell the participation of the second mode from the response, especially when the excitation is at the tip of the drill, which excites the first mode the most. This is the usual way in which a drill is subjected to cutting forces during drilling processes.

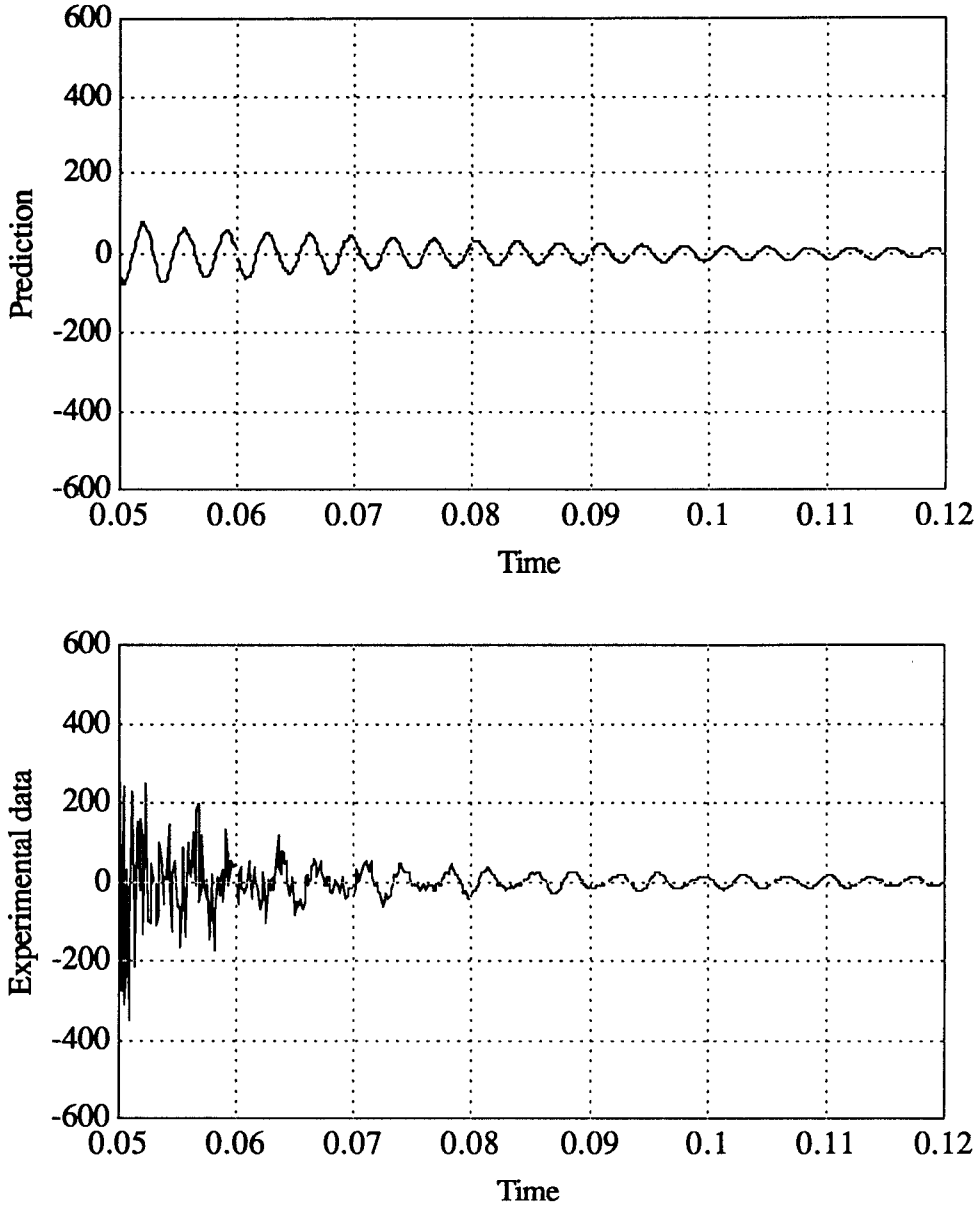

Figure 4.6 The predicted and experimental impulse response of the tip.

CHAPTER 5

SENSOR MEASUREMENT SYSTEM

AND DRILLING EXPERIMENT

In this chapter, the development of a sensor measurement system and methods of the drilling experiments are presented. The construction of a drilling dynamometer for measuring the thrust and torque is described from the design stages to the calibration procedure. Experiments are performed by drilling special specimens for determination of the constants in the thrust and torque models. A two-level design experimentation is also performed to estimate the cutting parameter effects on the thrust and torque generation. Dynamic characteristics of the drilling processes are also investigated based on the measured thrust and torque.

5.1 Construction of A Drilling Dynamometer

There are two types of sensing systems for measuring the thrust and torque of drilling processes: fixed-base and built-in types. When several tools machine on the workpiece simultaneously, the sensors are should be built into the machine tools, such as magnetic suspension spindle machining systems with magnetic bearings as senors. However, the stiffness of the tool spindle decreases dramatically due to the built-in sensors. For a fixed-base sensing system, although the stiffness of the working base decreases, its fundamental frequency could be adjusted to a level higher than the fundamental frequency of the drill. In order to measure thrust and torque precisely in this thesis, the dynamometer is designed as a base, fixing the workpieces being drilled.

The dynamometer mainly consists of several sets of strain gages. As the thrust and torque act on the dynamometer, the developed stress and strain change resistance values of the attached strain gages. Through Wheatstone bridges, the action of the thrust and torque can be detected by the output of the Wheatstone bridges. A pre-loading, or a calibration process is usually carried out to establish the quantitative mapping functions between the action of the thrust, torque and the bridge outputs. During drilling processes, the measurement of the thrust and torque can be made by measuring the bridge outputs and transforming the bridge outputs into the thrust and torque based on the calibration. There are three design stages: concept, structure, and gage layout and a calibration process described in the following sections.

5.1.1 Conceptual Design

Requirements important in dynamometer design are rigidity, sensitivity, and accuracy. The sensitivity of a good research dynamometer should be high enough such that the determined values are accurate to within a certain range, say ±1%. That is , if a dynamometer is designed for a maximum force of one hundred pounds, only one pound error between the true load and the determined value is allowable. The 1 pound error mainly comes from the sensitivity mapping of the noise level in voltage, and should be easily readable and accurately indicated. On the other hand, a dynamometer should be rigid enough so that the cutting operation is not influenced by the accompanying deflections.

The elastic body design of the dynamometer is a compromise between the requirement of sensitivity and rigidity. A thin-walled cylinder is chosen

in this thesis work. The thinner the wall, the more flexible the structure is. The flexibility increases the sensitivity, (i.e. the strains due to the thrust and torque). On the other hand, in order to compensate for the loss of the rigidity due to the sensitivity requirement, a large diameter must be chosen. Among cylinders with the same wall thickness, a larger diameter cylinder has a higher ratio of stiffness to mass, (i.e. a higher natural frequency). Also, the large diameter decreases the off-center error of the drill and the dynamometer.

In order to avoid the off-center error of the elastic cylinder and the rotating drill axis, the components are designed to minimize this error when assembled together, as shown in Figure 5.1. A central hole in the top plate is used for setting the center of the drilling machine. A concentric circular pocket under the top plate is used for aligning the elastic cylinder. The thicker parts on the two ends of the cylinder prevent the dynamometer from undergoing thermal deformation after being welded to the top and bottom plates.

5.1.2 Structural Design

The stress developed on the outer surface of the elastic cylinder is analyzed by considering a small element, described by the X-Y coordinate system in Figure 5.2. The element is subjected to the normal stresses σ_x and σ_y and the shear stress τ_{xy}, due to the thrust, TH, and the torque, TQ, respectively, which are given by:

$$\sigma_x = 0 \tag{5.1}$$

$$\sigma_y = -\frac{TH}{A_s} \tag{5.2}$$

$$\tau_{xy} = \frac{TQ \times R_s}{J_s} \tag{5.3}$$

where A_S is the cross section area,

$$A_s = \pi(R_s^2 - R_i^2) \tag{5.4}$$

and J_S is the polar moment of inertia,

$$J_s = \tfrac{1}{2}\pi(R_s^4 - R_i^4) \tag{5.5}$$

A Mohr's circle is constructed for the stress transformation of the same element described by another X'-Y' coordinate system. The new coordinate system (X'-Y') is rotated 45 degrees counterclockwise with respect to the original one (X-Y). The normal stresses along the X' and Y' axis are

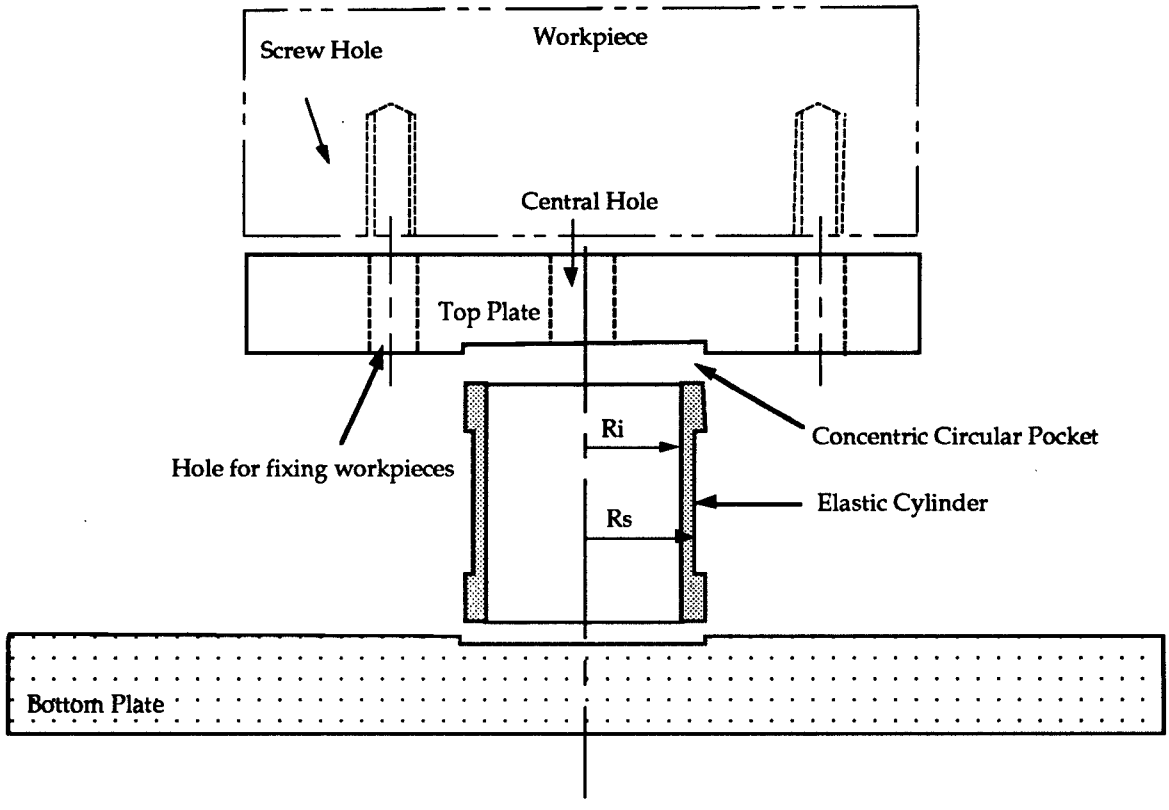

Figure 5.1 The dynamometer design.

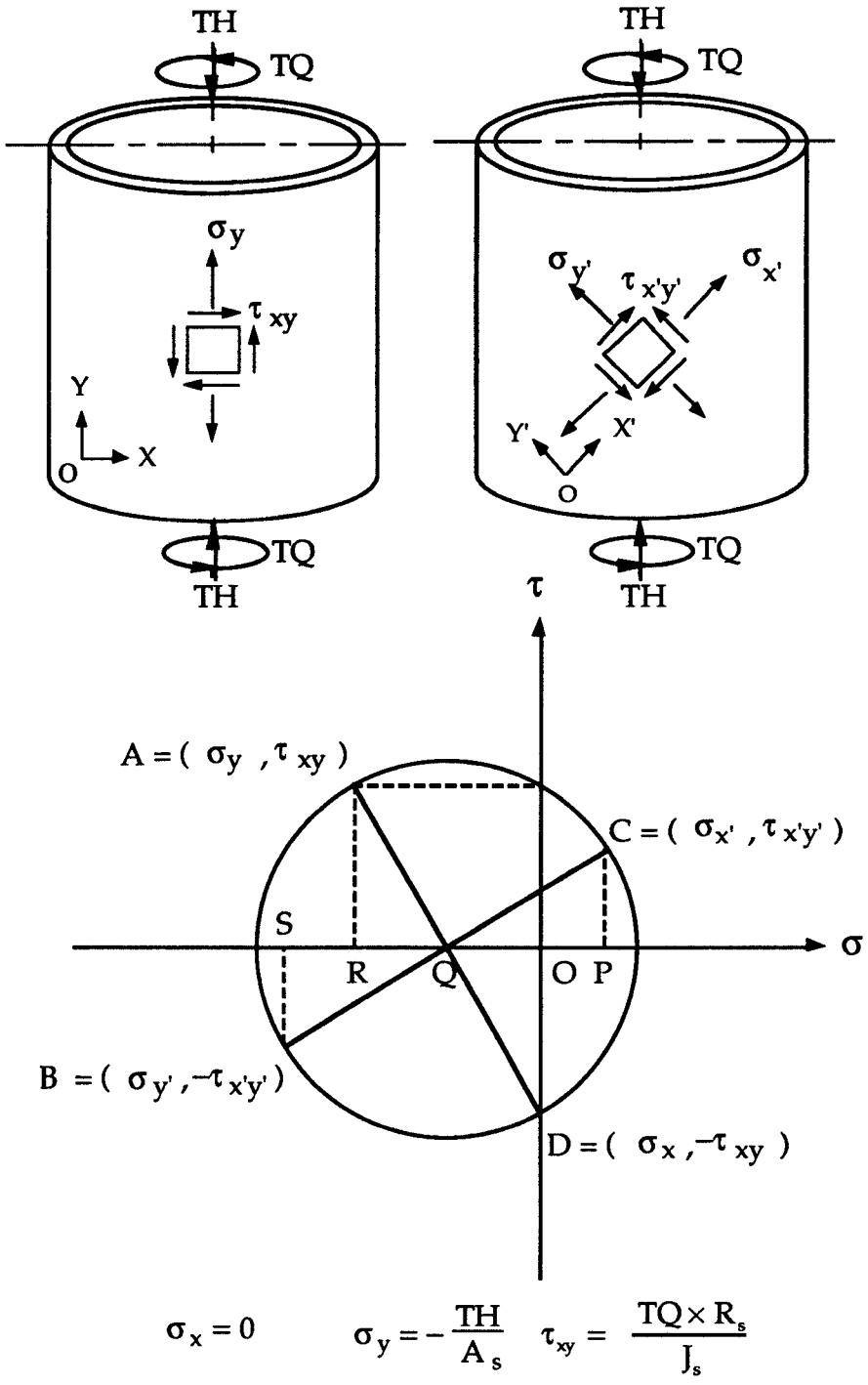

$$\sigma_x = 0 \qquad \sigma_y = -\frac{TH}{A_s} \qquad \tau_{xy} = \frac{TQ \times R_s}{J_s}$$

Figure 5.2 The Mohr's circle for stress in the cylinder.

calculated by comparing the triangles ΔQAR, ΔQDO, ΔBQS, and ΔCQP, as shown in Figure 5.2. The stresses are given by,

$$\sigma_{x'} = -\frac{TH}{2A_s} + \frac{TQ \times R_s}{J_s} \tag{5.6}$$

$$\sigma_{y'} = -\frac{TH}{2A_s} - \frac{TQ \times R_s}{J_s} \tag{5.7}$$

The strains along the X, Y, X', and Y' directions are governed by the following equations:

$$\varepsilon_x = \frac{\sigma_x}{E} - \frac{\nu\,\sigma_y}{E} \tag{5.8}$$

$$\varepsilon_y = \frac{\sigma_y}{E} - \frac{\nu\,\sigma_x}{E} \tag{5.9}$$

$$\varepsilon_{x'} = \frac{\sigma_{x'}}{E} - \frac{\nu\,\sigma_{y'}}{E} \tag{5.10}$$

$$\varepsilon_{y'} = \frac{\sigma_{y'}}{E} - \frac{\nu\,\sigma_{x'}}{E} \tag{5.11}$$

The maximum stress and minimum strain with respect to various cylinder dimensions can be calculated based on Equations 5.1 through 5.11 for achieving a suitable dynamometer design. The criteria are specified according to the workpiece material, drill diameter, and prior experience. The material properties of the selected steel are $E=10.6\times10^6$ psi, $G=3.9\times10^6$ psi, $\nu=0.36$, and yield stress is 60 ksi.

5.1.3 Gage Layout Design

Eight strain gages are installed on the cylinder surface at positions along, normal to, and 45 degrees (+ and -) oblique to the thrust direction. Three measured strains are adequate to construct the Mohr's circle for strain (or stress) in the cylinder. The other five measurements are arranged specially in Wheatstone bridges to compensate for thermal effects and the unavoidable bending moment and, also, increase the precision.

A strain gage is essentially a resistance element. In general, the resistance of a strain gage varies when it is subjected to a strain. Two factors are considered for selecting the gages: the gage factors and the size. The smaller the gage size, the more exactly the strain of the target point is measured, but the capacity for heat dissipation through the small gage area is limited. The undissipated heat will degrade the accuracy of the resistance measurement. A gage factor is defined as the resistance variation of the gage ($\Delta R_g/R_g$) per unit strain (ε), and is given by,

$$S_g = \frac{\Delta R_g / R_g}{\varepsilon} \tag{5.12}$$

where ε is the strain along the axis of the gage. For a given S_g, the unknown strain can be determined by measuring $\Delta R_g/R_g$. This quantity is usually measured by connecting the gages into Wheatstone bridge circuits as shown in Figure 5.3. The output voltage is initially zero when R1*R3=R2*R4 or R5*R7=R6*R8 (i.e. the bridge is balanced). and varies from zero when any resistance changes. The ratio of the input and the output voltage in the Wheatstone bridge circuits are described by Equations 5.13 and 5.14:

$$\frac{\Delta E_{out1}}{E_{in}} = \frac{r_e}{(1+r_e)^2}\left(\frac{\Delta R_1}{R_1} - \frac{\Delta R_2}{R_2} + \frac{\Delta R_3}{R_3} - \frac{\Delta R_4}{R_4}\right) \tag{5.13}$$

$$\frac{\Delta E_{out2}}{E_{in}} = \frac{r_e}{(1+r_e)^2}\left(\frac{\Delta R_5}{R_5} - \frac{\Delta R_6}{R_6} + \frac{\Delta R_7}{R_7} - \frac{\Delta R_8}{R_8}\right) \tag{5.14}$$

where r_e is the ratio of the resistances in the Wheatstone bridge (R_2/R_1 and R_6/R_5). For the given loading on the cylinder, the gages are arranged as in Figure 5.3 to provide maximum sensitivity and compensation against undesirable bending moments. The relationship between the thrust and the measured strain can be obtained by substituting Equations 5.1 and 5.2 into Equations 5.8 and 5.9 to give:

$$TH = -\varepsilon_y E A_s = \frac{\varepsilon_x E A_s}{\nu} \tag{5.15}$$

The relationship between thrust, TH, and output voltage, ΔE_{out1}, can be obtained by substituting Equations 5.12 and 5.15 into Equation 5.13 and simplifying:

$$TH = -\frac{E A_s (1+r_e)^2}{2(1+\nu) r_e S_g E_{in}} \Delta E_{out1} \tag{5.16}$$

Similarly, the relationship between the torque and the measured strain can be obtained by substituting equations 5..6 and 5.7 into the simultaneous equations 5.10 and 5.11 and solving simultaneously:

$$TQ = \frac{E J_s}{2(1+\nu) R_s}(\varepsilon_{x'} - \varepsilon_{y'}) \tag{5.17}$$

The relationship between torque, TQ, and output voltage, ΔE_{out2}, can be obtained by combining equations 5.12, 5.14, and 5.17:

$$TQ = \frac{E J_s (1+r_e)^2}{4(1+\nu) R_s r_e S_g E_{in}} \Delta E_{out2} \tag{5.18}$$

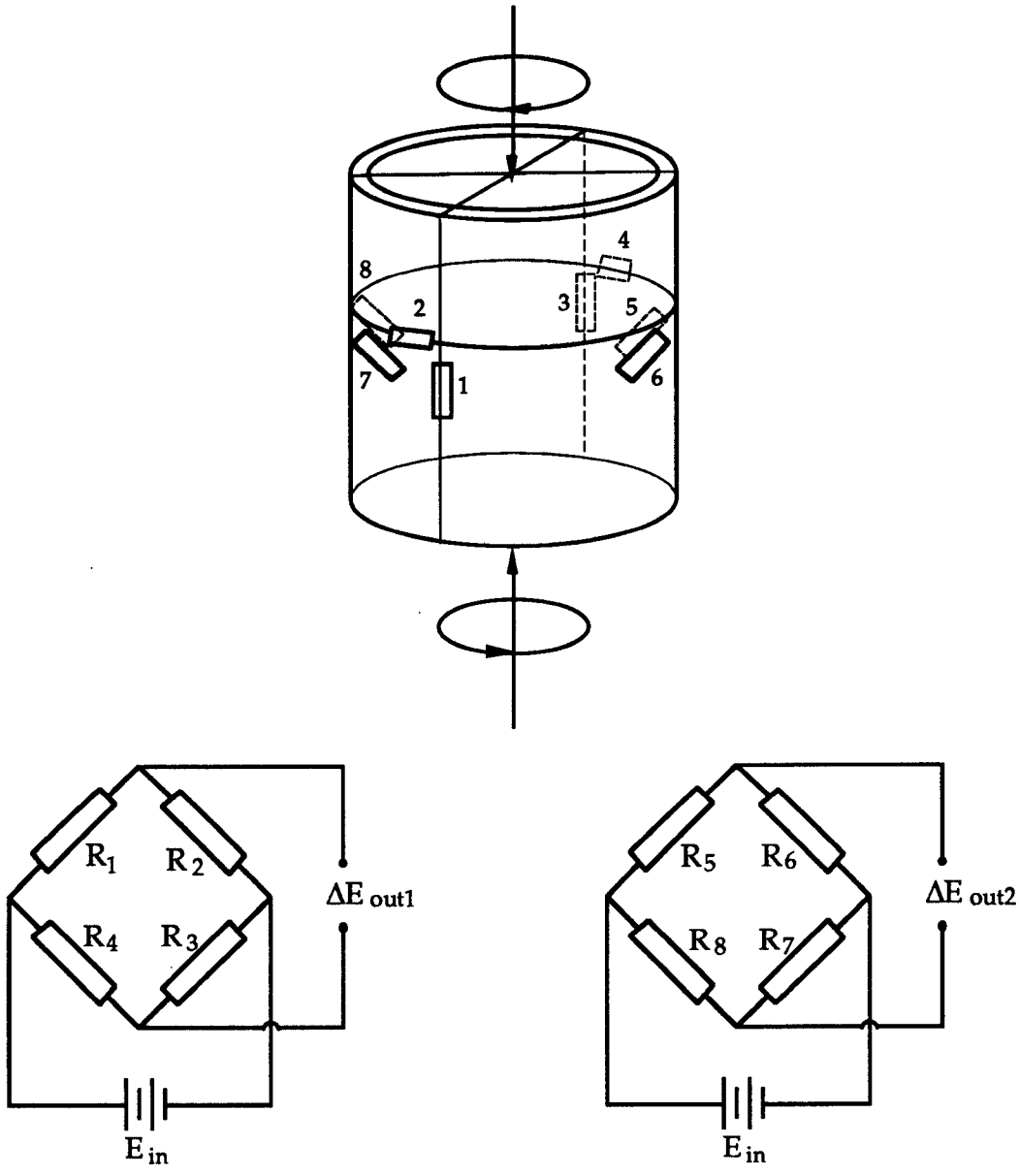

Figure 5.3 The layout of the strain gages.

In order to fit the requirement of the data acquisition system used, an amplifiers is arranged to magnify the signals. As shown in Figure 5.4, the magnification factor of the operational amplifier is determined by the ratio of the resistant, R1/R2. A signal digitizer is used to convert the voltage to digital signals for on-line monitoring of the thrust and torque using a personal computer. Both the thrust and torque are proportional to the output voltages, and ready to be read after calibration.

In the present experiment, the total time for measurement is about several seconds only, and the strains are assumed to be uniformly distributed on the surface covered by the strain gage. The data of the selected strain gages is listed below:

Gage Type:	EA-13-240LZ-120
Resistance (Ohms)	120.0
Gage Factor:	2.110
Size:	0.24" *0.08"
Temperature Range:	-100^0 to $+350^0$F (-75^0 to $+175^0$C)
Fatigue Life:	10^8 cycles at 1200$\mu\varepsilon$, 10^6 cycles at 1500$\mu\varepsilon$
Producer:	Measurements Group, Inc.

5.1.4 Calibration of the Dynamometer

A dynamometer should be calibrated prior to its use. The main purpose of the calibration process is to establish the transfer functions between the voltage signals and the thrust and torque generated during the drilling process. The diagram of the strain gage calibration process is shown in Figure 5.5. Two channels, V_{th} and V_{tq}, are recorded when either thrust or torque is applied, such that the cross-talk terms can be estimated. The

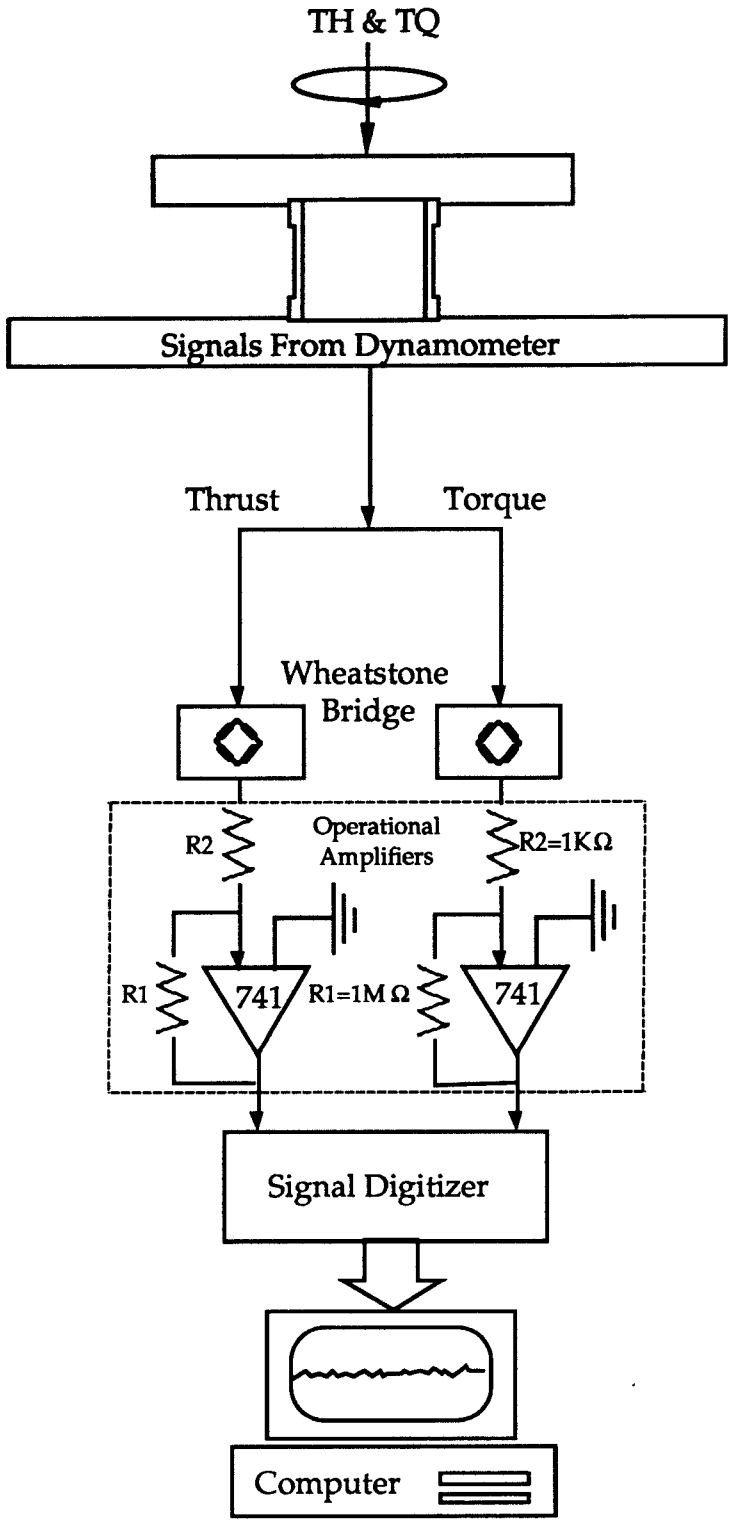

Figure 5.4 Connection of the experiment test.

relationship between the applied thrust (or torque) and voltage output of the dynamometer is shown in Table 5.1, and plotted in Figure 5.6. The transfer function (or transmission ratio), TR, is defined as the mapping from the input (applied thrust or torque) and the output (computer voltage reading) in matrix form:

$$TR = \begin{bmatrix} \frac{\Delta V_{th}}{\Delta TH} & \frac{\Delta V_{th}}{\Delta TQ} \\ \frac{\Delta V_{tq}}{\Delta TH} & \frac{\Delta V_{tq}}{\Delta TQ} \end{bmatrix} = \begin{bmatrix} T_{11} & T_{12} \\ T_{21} & T_{22} \end{bmatrix} = \begin{bmatrix} 0.0220 & -0.0016 \\ -0.0019 & 0.0391 \end{bmatrix} \tag{5.19}$$

Each element, T_{ij}, of TR is the transfer function of the i^{th} computer voltage output and the j^{th} applied force component. The force vector, or the thrust and torque, can be calculated as:

$$\begin{bmatrix} TH \\ TQ \end{bmatrix} = TR^{-1} \begin{bmatrix} V_{th} \\ V_{tq} \end{bmatrix} = \begin{bmatrix} 45.5490 & 1.8804 \\ 2.1760 & 25.0574 \end{bmatrix} \begin{bmatrix} V_{th} \\ V_{tq} \end{bmatrix} \tag{5.20}$$

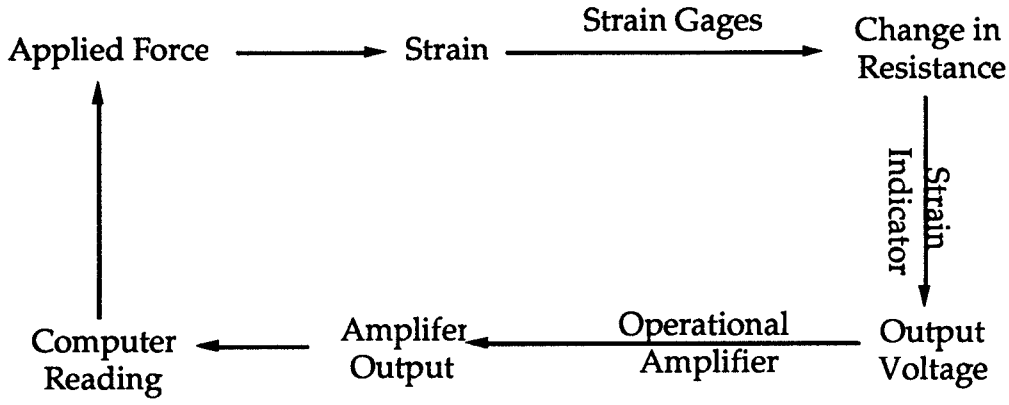

Figure 5.5 Diagram of the drilling dynamometer calibration process.

Thrust (lbs)	V_{th} (volt)	V_{tq} (volt)
10	0.2700	0.0300
20	0.4800	0.0100
30	0.7200	-0.0200
40	0.9200	-0.0300
50	1.1400	-0.0600
60	1.3600	-0.0800
70	1.5800	-0.1000
80	1.8000	-0.1200
90	2.0200	-0.1300
100	2.2400	-0.1500
90	2.0000	-0.1500
80	1.7800	-0.1300
70	1.5600	-0.1200
60	1.3300	-0.0900
50	1.1000	-0.0700
40	0.8900	-0.0600
30	0.6800	-0.0400
20	0.4500	-0.0300
10	0.2300	-0.0100

Torque (inch-lbs)	V_{th} (volt)	V_{tq} (volt)
48.75	-0.0400	1.5900
97.50	-0.1200	3.3200
146.25	-0.1800	5.2200
195.00	-0.2600	7.2400
243.75	-0.3500	9.2200
195.00	-0.2800	7.3400
146.25	-0.1900	5.6200
97.50	-0.1000	3.5600
48.75	-0.0300	1.6200

Table 5.1 Calibration voltage and applied load.

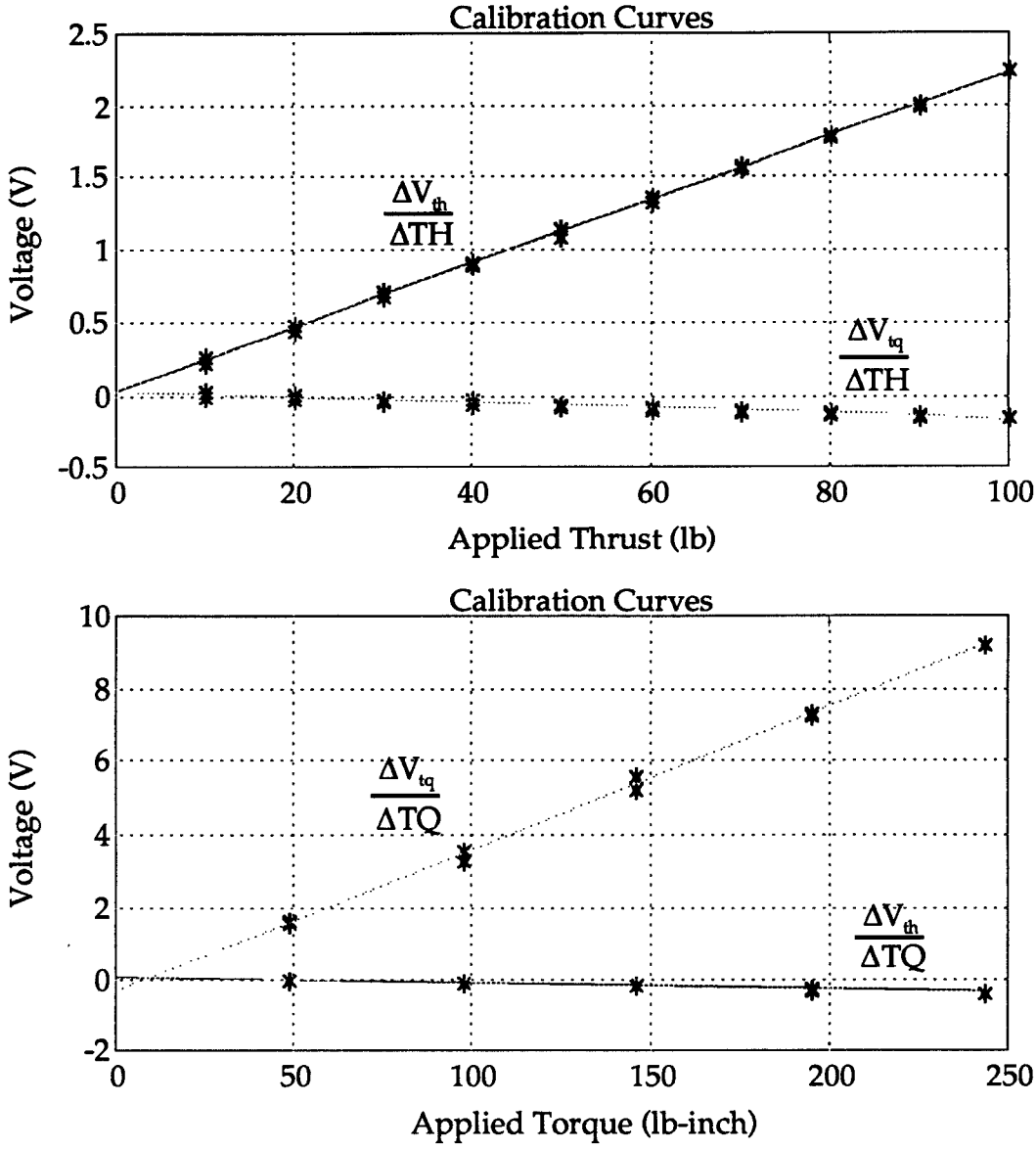

Figure 5.6 Calibration curves.

5.2 Experimental Study

The need to perform experimental studies in this thesis work is evident. The mathematical models developed are based on general physical laws and results from previous research reported in the books and/or publications. The models have to be completed through the calibration process of the undetermined constants. The cutting parameter effects on the thrust and torque are investigated, also. The developed sensing system has to be shown to be useful. There are three main objectives to carry out the experimental studies:

(1) Calibrate the constants introduced during the model development

(2) Investigate the cutting parameter effects on the thrust and torque.

(3) Explore the possibility of on-line monitoring of drilling operations.

5.2.1 Experimental setup and environments

The experiments are performed on a milling machine in the shop floor at the Department of Mechanical Engineering, University of Maryland, College Park. The drill, dynamometer, and machine table can be seen from Figures 5.7 (a). The drill with the geometrical properties, the same as the drill in chapter 3 and 4, is selected to do the experiment. Heavy-duty water-soluble coolant is applied to avoid the effects of the heat generated during machining. Aluminum 6061 T6 material is selected as workpiece to perform the test. The two pulleys fixed on the machine tables are used to turn the gravity of the standard weights into the force components producing the torque needed for calibration.

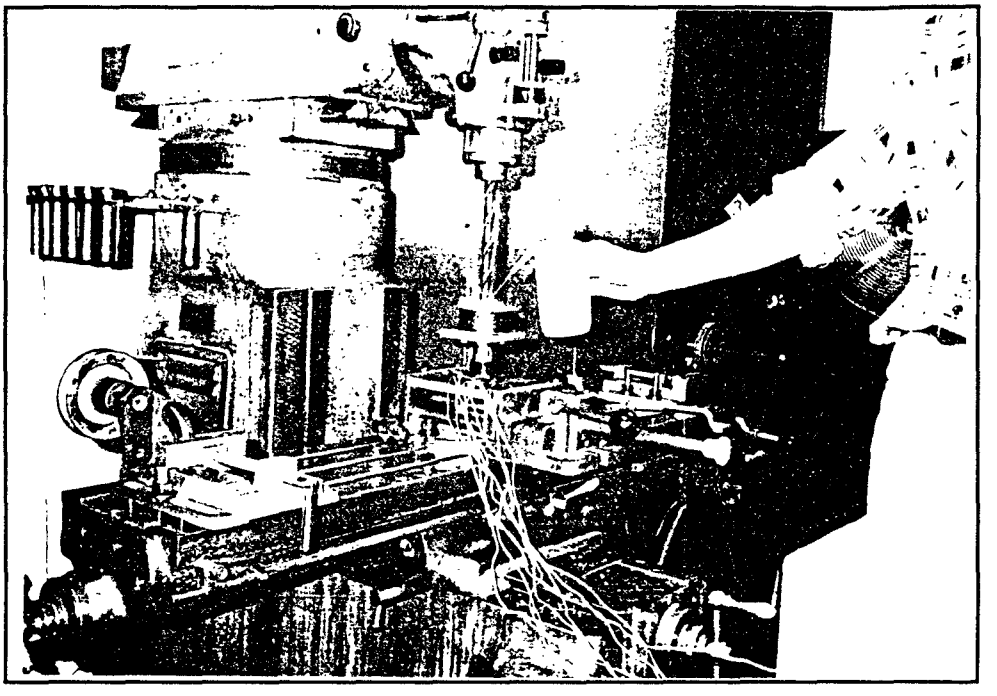

Figure 5.7 (a) Experimental setup.

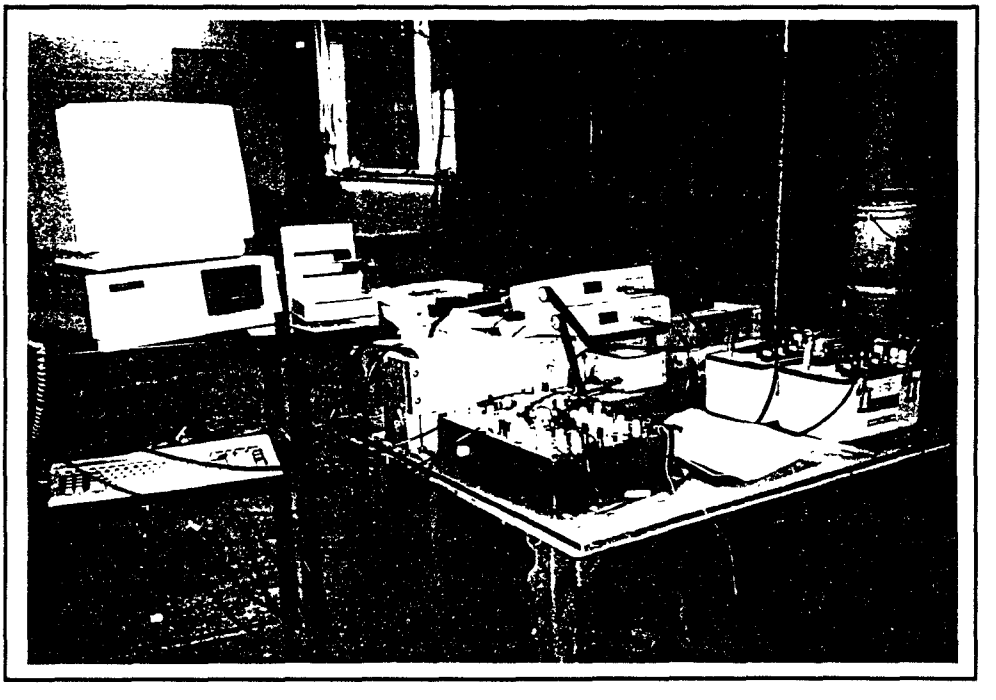

Figure 5.7 (b) Experimental setup.

Figure 5.7 (b) shows the Wheatstone bridge, operational amplifiers, and the data acquisition system. The sampling rate is selected as 0.05 ms, such that the highest frequency of the detectable signal reaches up to 10 kHz. The total number of sampling is 2048 for each channel. The noise level is estimated by the measurement under no load. The standard deviation of the noise is 1.2 lbs for thrust and 0.8 inch-lbs for torque. The noise mainly comes form the amplifier circuits and the measurement environment.

5.2.2 Preparation of Workpiece Specimens

The cutting forces at a small sections along the cutting edges is analyzed in Chapter 3. The analyzed force components are summed to form the resultant thrust and torque. Conversely the partial thrust and torque of the small section are measured by machining the workpiece on the section only. It is not practical to produce the workpiece of the special geometry, but it is easy to produce different size holes. The thrust and torque differences between enlarging two different-radius holes to a certain diameter are the partial thrust and torque contributed by drilling the section between the two radii only.

The workpiece with an echelon concave hole, shown in Figure 5.8 is designed for the experiment to investigate the indirect observations, partial thrust and partial torque. Three holes of different size, H1, H2 and H3, are made before carrying out the experiments. The depth of each of the three holes is about 1/4". The diameters of the three holes are 2/16", 5/16", and 8/16", respectively. Such a design allows three various drilling processes with equal incremental width of drilling by an 11/16"-drill. At the beginning

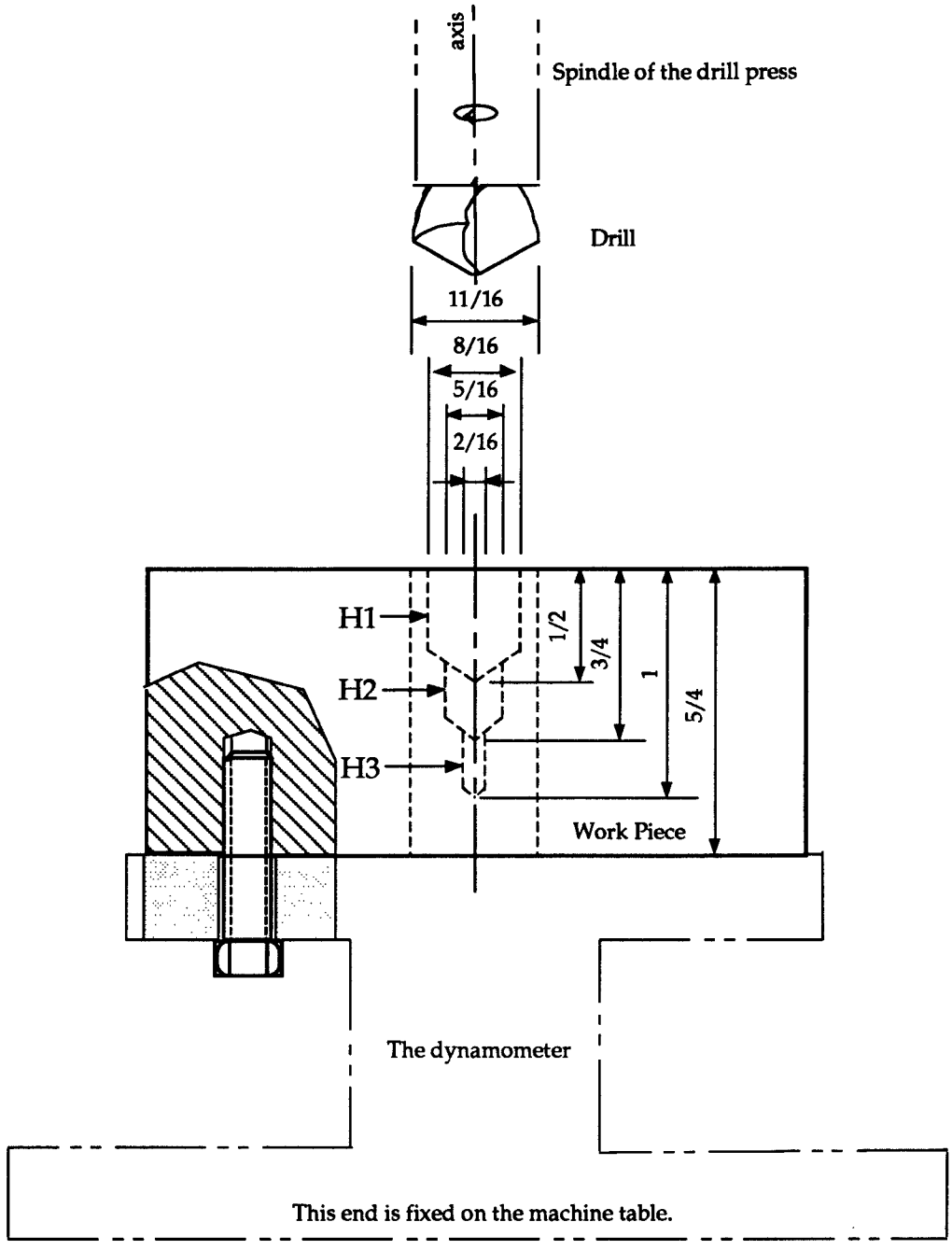

Figure 5.8 Workpiece specimen with three holes for drilling experiments.

of a drilling operation, the width of drilling is the difference between 11/16" and 8/16", which is defined as the first section. When the drill enlarging the pre-made hole, H2, the width of drilling changes to (11/16"-5/16"), which is the combination of the first and second sections. Again, when the third pre-made hole, H3, is drilled, the width of the drilling changes to (11/16"-3/16"), combination of the first, second, and third sections. In order to keep the drill axis at the center of the those holes, the holes are made on the dynamometer, just before the test is performed without changing the fixture. The concentric holes, H1, H2, H3, at different depth guarantee the most accurate concentric location and the least error for these test. The principle is known as the "Blocking Principle". During enlarging holes H1, H2, H3, thrusts TH1, TH2, TH3 and torques TQ1, TQ2, and TQ3 are measured by the built dynamometer. The partial thrusts, ΔTH1, ΔTH2, and ΔTH3 and partial torques, ΔTQ1, ΔTQ2, ΔTQ3 represent the thrust and torque needed for drilling the first, second, and third section of the workpiece, which can be estimated through the measurements by:

$$\begin{aligned}
&\Delta TH1 = TH1, \\
&\Delta TH2 = TH2 - TH1 \\
&\Delta TH3 = TH3 - TH2 \\
&\Delta TQ1 = TQ1 \\
&\Delta TQ2 = TQ2 - TQ1 \\
&\Delta TQ3 = TQ3 - TQ2
\end{aligned} \tag{5.21}$$

Figure 5.9 and 5.10 demonstrate the measured thrusts and torques of drilling three holes, H1, H2 and H3, in one workpiece under the same operating condition, showing the mean values of these measurements. Based on the estimated partial thrusts and partial torques, ΔTH and ΔTQ,

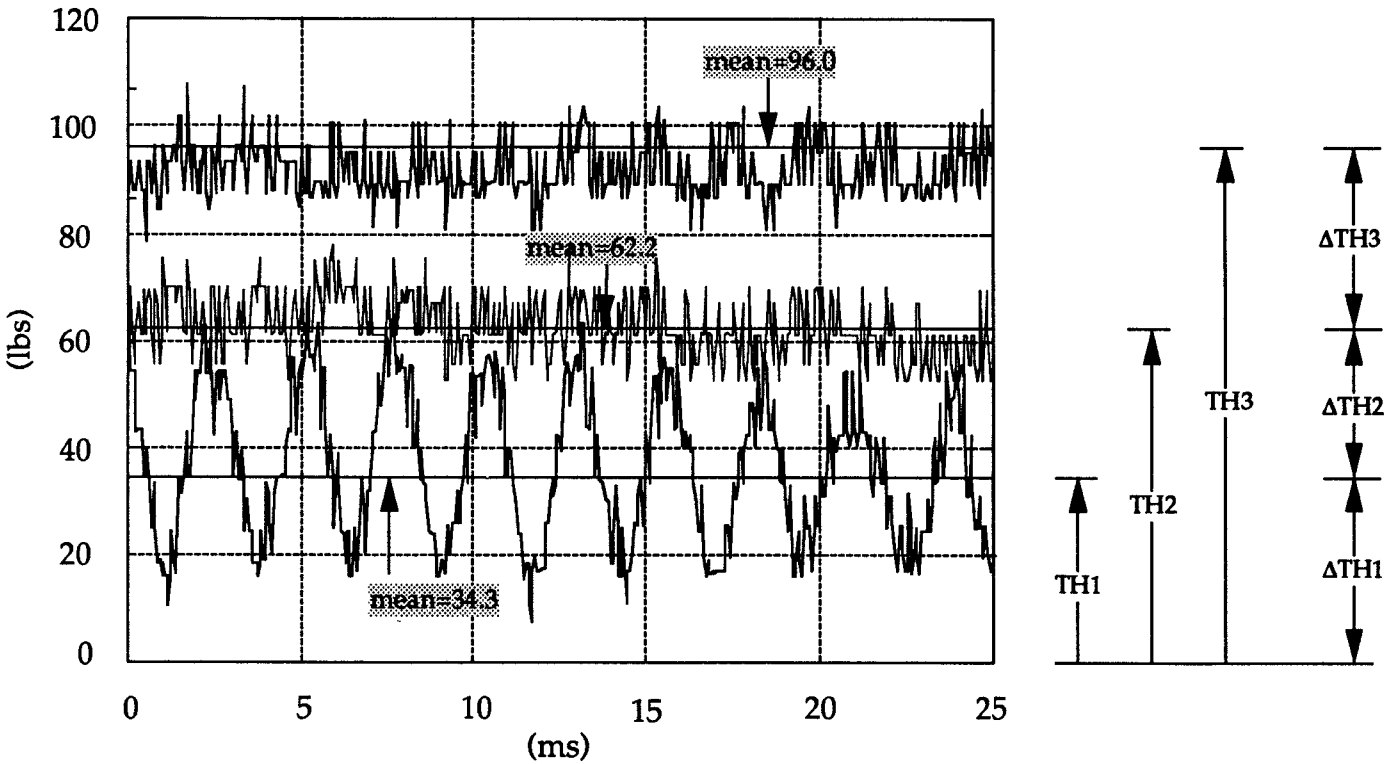

Figure 5.9 Thrust measurements TH1, TH2, and TH3 under feed rate 0.0015 in/rev and spindle speed 325 rpm.

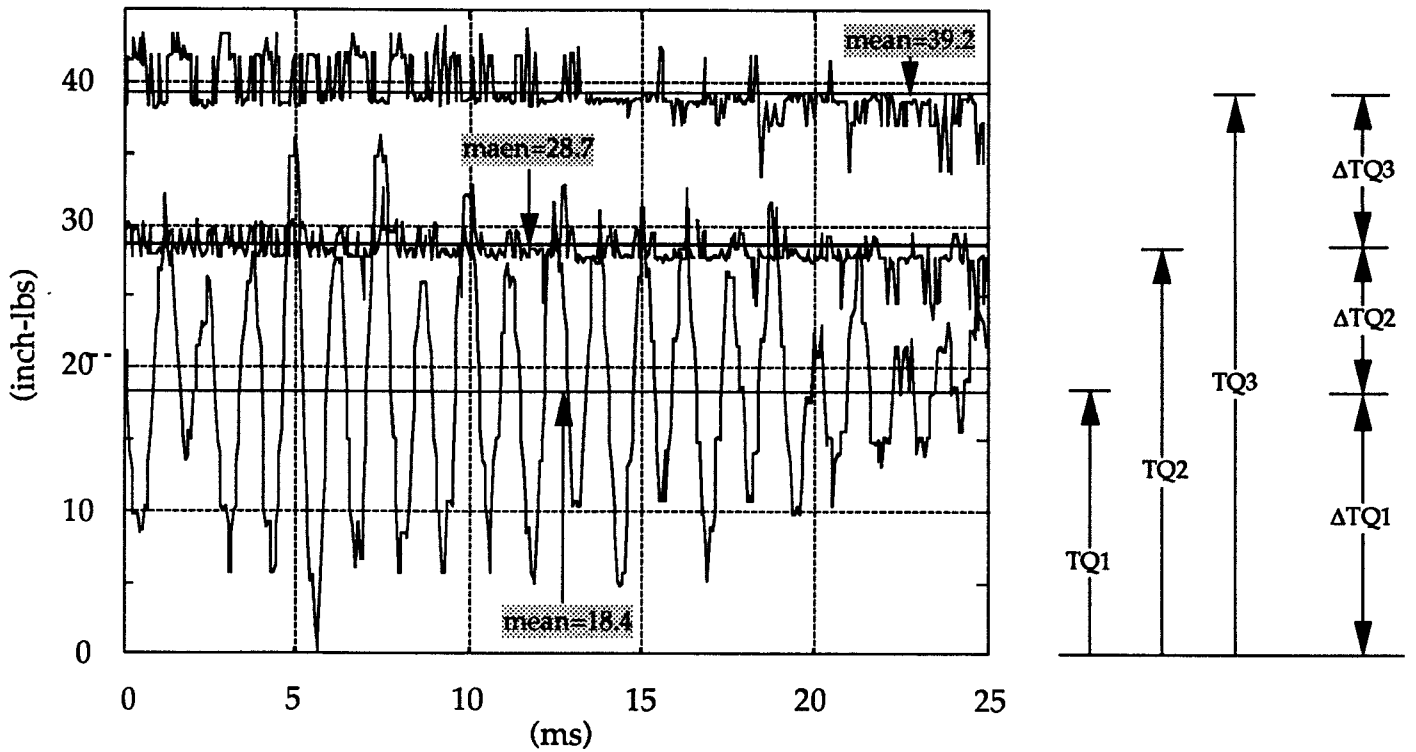

Figure 5.10 Torque measurements TQ1, TQ2, and TQ3 under feed rate 0.0015 in/rev and spindle speed 325 rpm.

indirectly observed through the preparation of the specially designed specimens, the cutting force distribution along the drill radius can be obtained. It is assumed that the axial force, ΔF_z, along the drill axis is represented by half of the partial thrust at the midpoint of the section. The cutting force normal to drill radius and axis, ΔF_y, is represented by half of the torque divided by radius at the midpoint of the section. The derived observations then are transformed to ΔR_n and ΔR_t for the calibration processes of constant determination, described in Chapter 3.

5.2.3 Investigation of Cutting Parameter Effects

Based on the force model in two dimensional cutting processes, large feed rate will introduce large cutting force, and large spindle speed will introduce small cutting force. The thrust and torque generated during drilling processes vary as the condition of the machining operations changes. In order to investigate the effects of the cutting parameters on the generation of the thrust and torque, experiments are conducted based on the strategy called two-level design of experimentation. As shown in Figure 5.11, four tests are performed under two different feed rates and two different spindle speeds at the four corners of the combination of the low levels, coded -1, and the high levels, coded +1 Figure 5.12 and 5.13 show the measured thrust and torque signals of the four tests of drilling holes of the same size, H1. The four mean values of the tests are used to perform a factorial analysis and to estimate the effects of feed rate and spindle speed on the thrust and torque. Empirical models of the thrust and torque can be established to represent the level of the cutting parameter effects. The detail procedures and the results will be discussed in Chapter 6.

Test Condition Number	Feed (inch/rev) F	Spindle Speed (rpm) N
a. Original units of variables		
1	0.0015	325
2	0.0030	324
3	0.0015	660
4	0.0030	660
b. Coded units of variables		
1	-1	-1
2	+1	-1
3	-1	+1
4	+1	+1

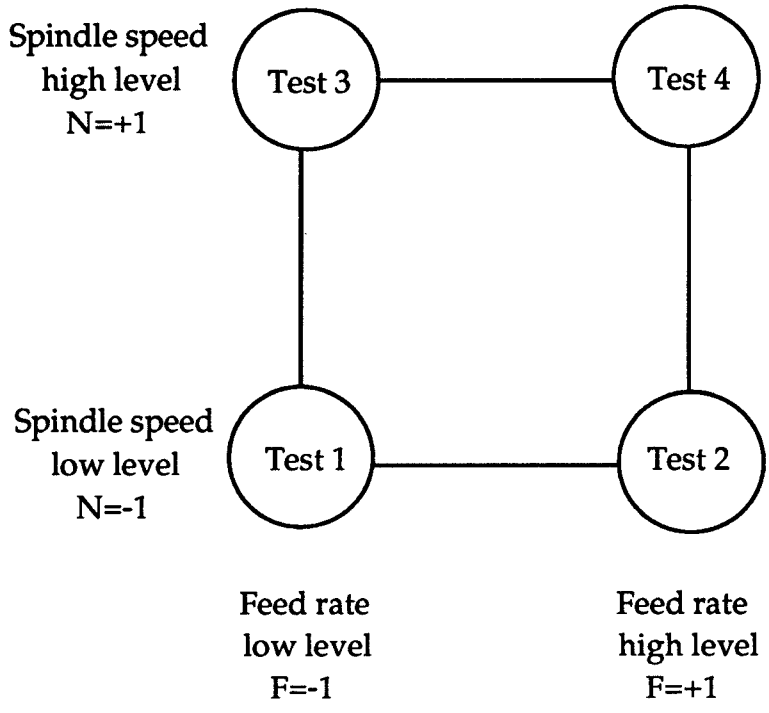

Figure 5.11 Two-level design of experimentation.

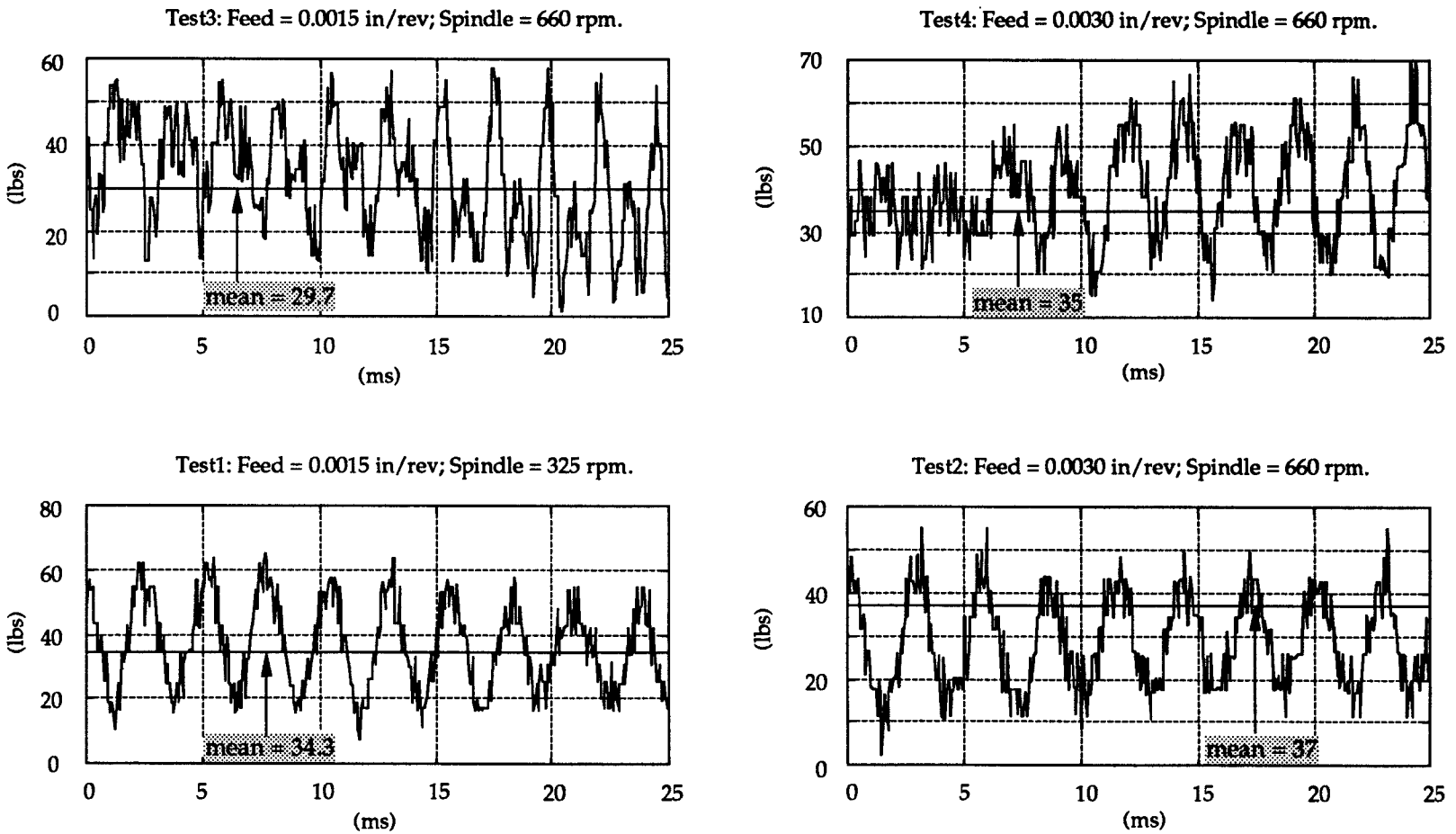

Figure 5.12 Thrust measurements of drilling hole H1
under four test conditions.

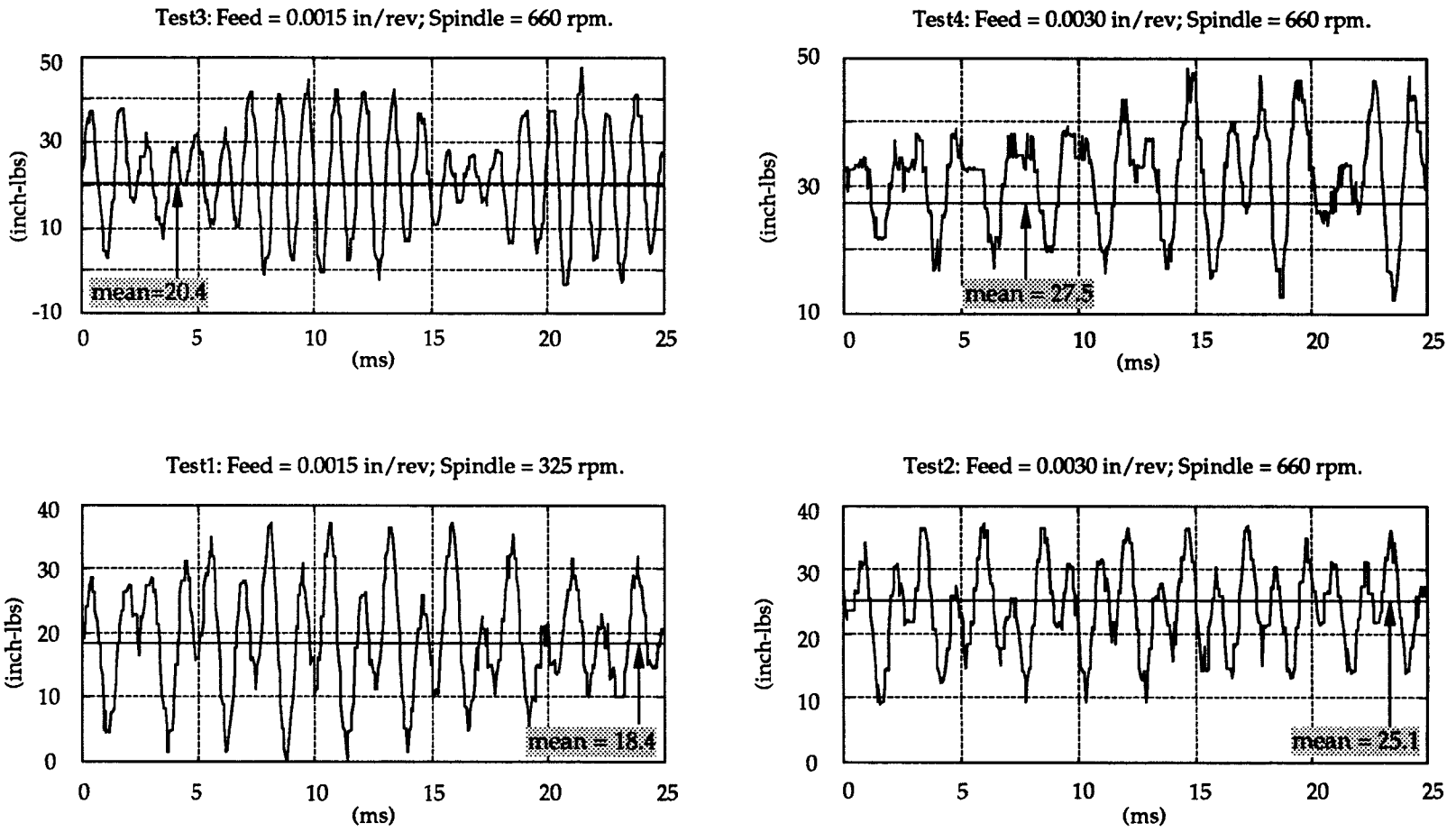

Figure 5.13 Torque measurements of drilling hole H1 under four test conditions.

5.2.4 Dynamic Characteristics of the Measured Thrust and Torque

In order to address the dynamic characteristics of the machining process, the measured thrust and torque signals during the sampling period are transformed to frequency domain by FFT (Fast Fourier Transformation) in MATLAB. The power spectra of the measured thrusts, TH1, TH2, and TH3 and torques, TQ1, TQ2, and TQ3 for drilling holes H1, H2 and H3 under test condition 1 (feed rate=0.0015 in/rev; spindle speed=325 rpm) are shown in Figure 5.14 and 5.15. The figures show the energy status of the measured signals in frequency domain, from drilling hole H1, H2 to H3, corresponding to the three plots placed from the top to the bottom. Usually, the dynamic signals are dominated by the modes of the lower natural frequencies of the machine tool. The lower modes of the measured signals are used to compare with the identified modal parameters in chapter 4 to realized how the drill structure affect the the thrust and torque generation. Also, the measured signals are the response of the dynamometer due to excitation thrust and torque generated during drilling processes. The dynamometer should have a higher fundamental natural frequency than the lowest mode of the drill structure, such that the measured signals can correctly represent the generated thrust and torque.

In Figure 5.14, the first plot of drilling hole H1 shows an obvious peak appearing at a specific frequency, which is more obvious compared with the plots of drilling holes H2 and H3. There are lots of energy appearing in the form of a harmonic thrust oscillating at the frequency. This is due to an orbit vibration in the lateral direction at the beginning of the drilling process. The

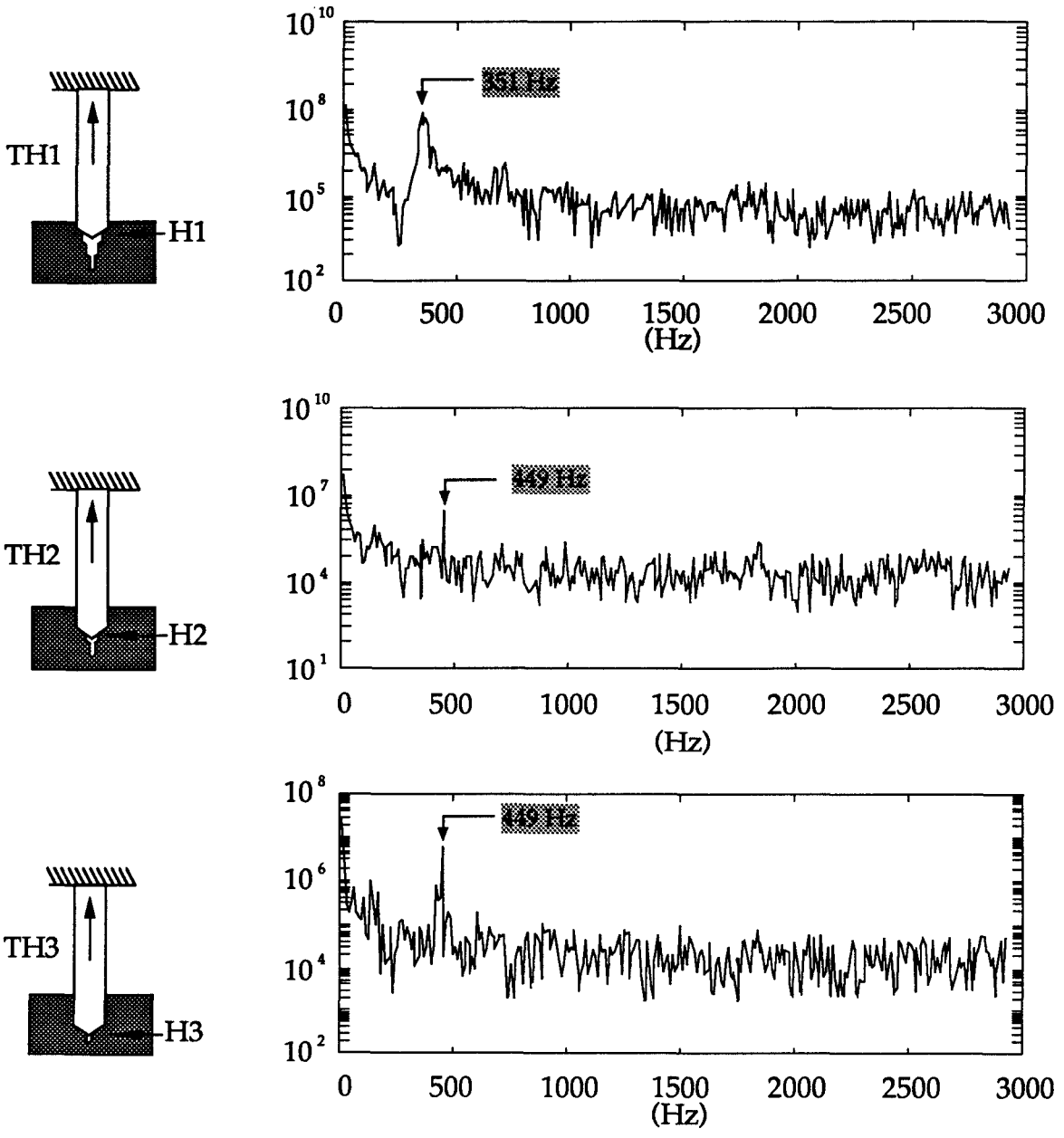

Figure 5.14 Power spectra of the thrust measurements TH1, TH2, and TH3 under test condition 1.

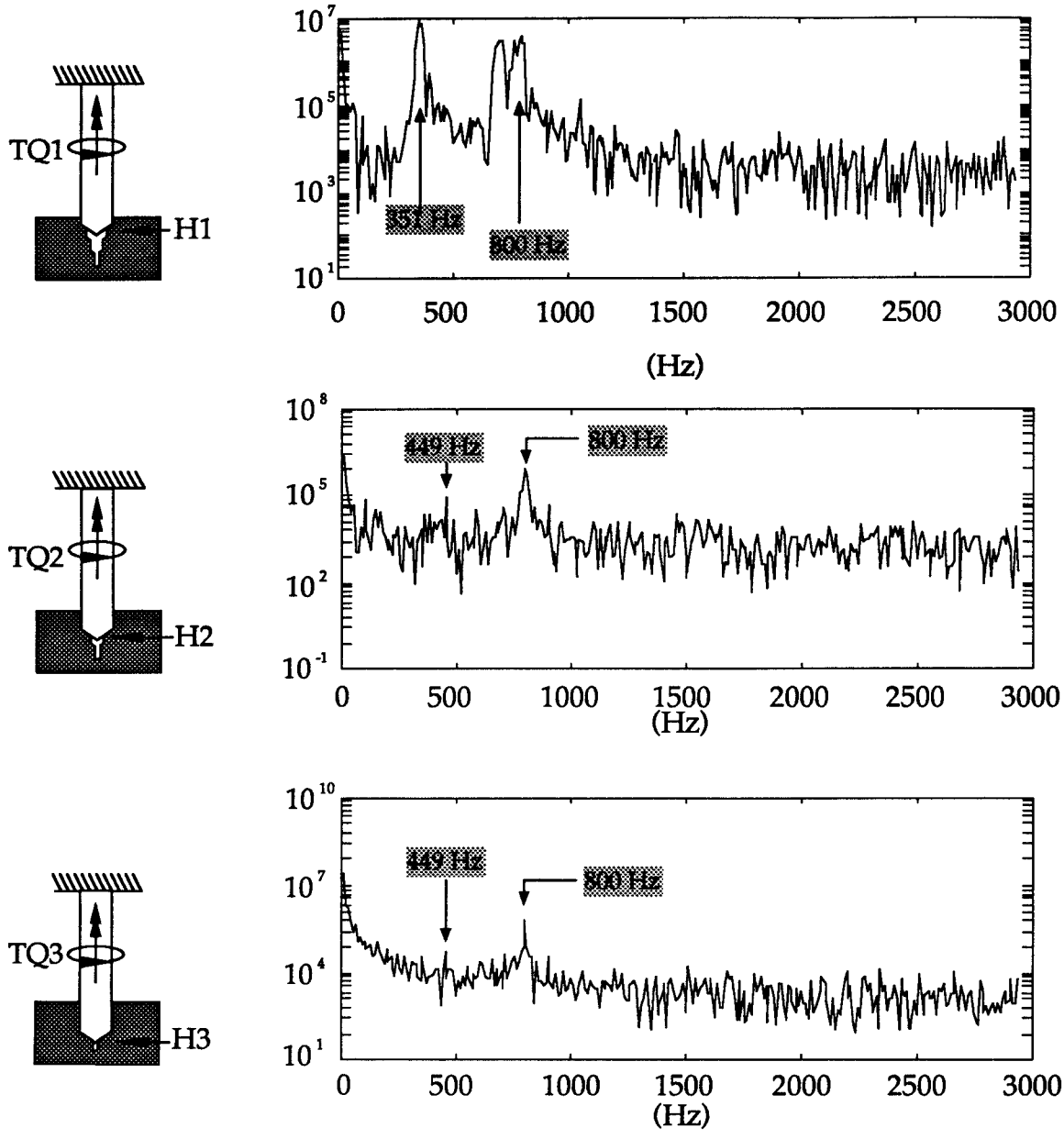

Figure 5.15 Power spectra of the torque measurements TQ1, TQ2, and TQ3 under test condition 1.

vibration components in the lateral direction of the drill excite the degree of freedom of the lowest natural frequency and cause the oscillation of the cutting force generation in the orthogonal cutting plane as well as the resultant thrust. Since the drill merges into the workpiece during drilling, the free boundary condition at the drill tip will become supported. And the length of drill will become shorter and shorter while the machining process is going on. The drilling process will become more stable; the drill structure becomes stiffer and the peak of the power spectra becomes less obvious. Besides, the natural frequencies of the drill will increase due to the increasing stiffness of the structure. As shown in the first plot of drilling hole H1, the first peak of the power spectrum is at 351 Hz which is a little higher than the identified one (333.1 Hz) in chapter 4. As the drilling process is going on, the first peaks of the power spectra of drilling holes H2 and H3 become higher (449 Hz).

Similar phenomenon of the first peak of the measured torque can be seen in Figure 5.15. The vibration components in the lateral direction of the drill cause the oscillation of the cutting force generation in the orthogonal cutting plane and the resultant torque. In the last plot of drilling hole H3, the first peak can hardly be distinguished. Special attention should be given to the second mode of the spectra (800 Hz). By referring to the results of Chapter 4, the second mode of the drill structure is 1688 Hz, which is much higher than 800 Hz. And this second mode (800 Hz) occurs only in the torque measurements. Inference is made that the mode is the torsional vibration of the dynamometer, which is higher than the lowest mode of the drill structure. This guarantees the stability of the machining processes and the precision level of the mean of the thrust and torque measurements.

CHAPTER 6

INVESTIGATION OF CUTTING PARAMETER EFFECTS AND ON-LINE MONITORING STRATEGY

In this chapter, experimental results obtained from the two-level design experimentation during the drilling tests are analyzed. Empirical models to establish the relations between the thrust and cutting parameters and between the torque and cutting parameters are derived through factorial analysis. Important observations regarding optimal combinations of cutting parameter settings for achieving specific objectives are found through the analysis. The prototype system for performing on-line monitoring of the drilling operation developed in this work is discussed. A strategy for implementing a sensor-based drilling system, for allowing control from shop floor, is presented, suggesting the direction of future research.

6.1 Cutting Parameter Effects on Thrust and Torque Generation

In Chapter 5, a detailed description of the experimental study of the thrust and torque was presented. Data of the thrust and torque during the drilling tests were collected. In this section, a factorial analysis will be carried out to reveal the information from the experimental results.

6.1.1 Factorial Analysis

Examining the data at the first column in Table 6.1, they represent the mean values of the measured thrust, TH1, during the drilling process of hole H1. An empirical model can be built through factorial analysis from the measured data. The empirical model can be used for the thrust prediction as

long as the spindle speed and feed setting are within the limits represented by the upper and lower levels. The empirical model used in this thesis work consists of a mean value, two main effects and an interaction effect, namely,

$$F_{prd} = \text{Mean} + \frac{MF_f}{2}F + \frac{MF_n}{2}N + \frac{IF_{fn}}{2}N \times F \tag{6.1}$$

The factorial Analysis performed in this thesis work focuses on the estimation of the mean value, main effects, and interaction effect as listed in Equation 6.1. The mean value in Equation 6.1 is calculated from averaging the four measured thrust forces at the four machining conditions. Its physical interpretation is the predicted thrust force when spindle speed is set at the middle of 325 and 660 rpm and feed is set at the middle of 0.0015 and 0.0030 inch/rev, calculated as Equation 6.2:

$$\text{Mean} = \frac{1}{4}(34.3 + 37.0 + 29.7 + 35.0) = 34.0 \tag{6.2}$$

Consider the first and second tests of the measured thrust, TH1, in Table 6.1, the corresponding thrust forces (34.3 lbs and 37.0 lbs) differ 2.7 lbs only

	F	N	TH1 (lbs)	TH2 (lbs)	TH3 (lbs)	TQ1 (inch-lbs)	TQ2 (inch-lbs)	TQ3 (inch-lbs)
Test 1	-1	-1	34.3	62.2	96.0	18.4	28.7	39.2
Test 2	+1	-1	37.0	67.3	107.7	25.1	39.4	52.4
Test3	-1	+1	29.7	56.4	86.3	20.4	29.0	36.3
Test4	+1	+1	35.0	68.7	103.3	27.5	41.5	52.1

Table 6.1 The mean values of the measured thrust and torque.

because of feed rate. The spindle speed setting is the same for both of these conditions. In addition to this pair, there is another pair of the thrust forces (29.7 lbs and 35.0 lbs) that differ 5.3 lbs only because of feed rate. The average of these two measures (4.0 lbs) represents the main effect of spindle speed on the thrust force. It is calculated by Equation 6.3:

$$MF_f = \frac{1}{2}[(37.0 - 34.3) + (35.0 - 29.7)] = 4.0 \tag{6.3}$$

In a similar manner, the main effect of spindle speed on the thrust can be calculated by averaging the two measures, i.e., the difference (-4.6 lbs) between 34.3 lbs and 29.7 lbs, and the difference (-2.0 lbs) between 37.0 lbs and 35.0 lbs, as shown in Figure 6.3. In the present case, the main effect of spindle speed, denoted by MF_n, is -3.3 lbs, as shown in Equation 6.4:

$$MF_n = \frac{1}{2}[(29.7 - 34.3) + (35.0 - 37.0)] = -3.3 \tag{6.4}$$

It should be pointed out that in the above calculations, the feed rate effect is much larger with a higher spindle speed setting (5.3 lbs) than that with a low spindle speed setting (2.7 lbs), as shown in Figure 6.1. The spindle speed effect is much larger with a low feed rate setting (-4.6 lbs) than that with a high feed rate setting (-2.0 lbs), as shown in Figure 6.2. The two cutting parameters, spindle speed and feed rate, do not behave additively and therefore "interact". A measure of this interaction can be identified by the difference between the spindle speed effect with a low feed setting (-4.6 lbs) and the spindle speed effect with a high feed setting (-2.0 lbs). By convention, half the difference is called the spindle speed by feed interaction, or, in symbols, the $N \times F$ interaction. In the present case, the $N \times F$ interaction is

o Spindle Speed 325 rpm

* Spindle Speed 660 rpm

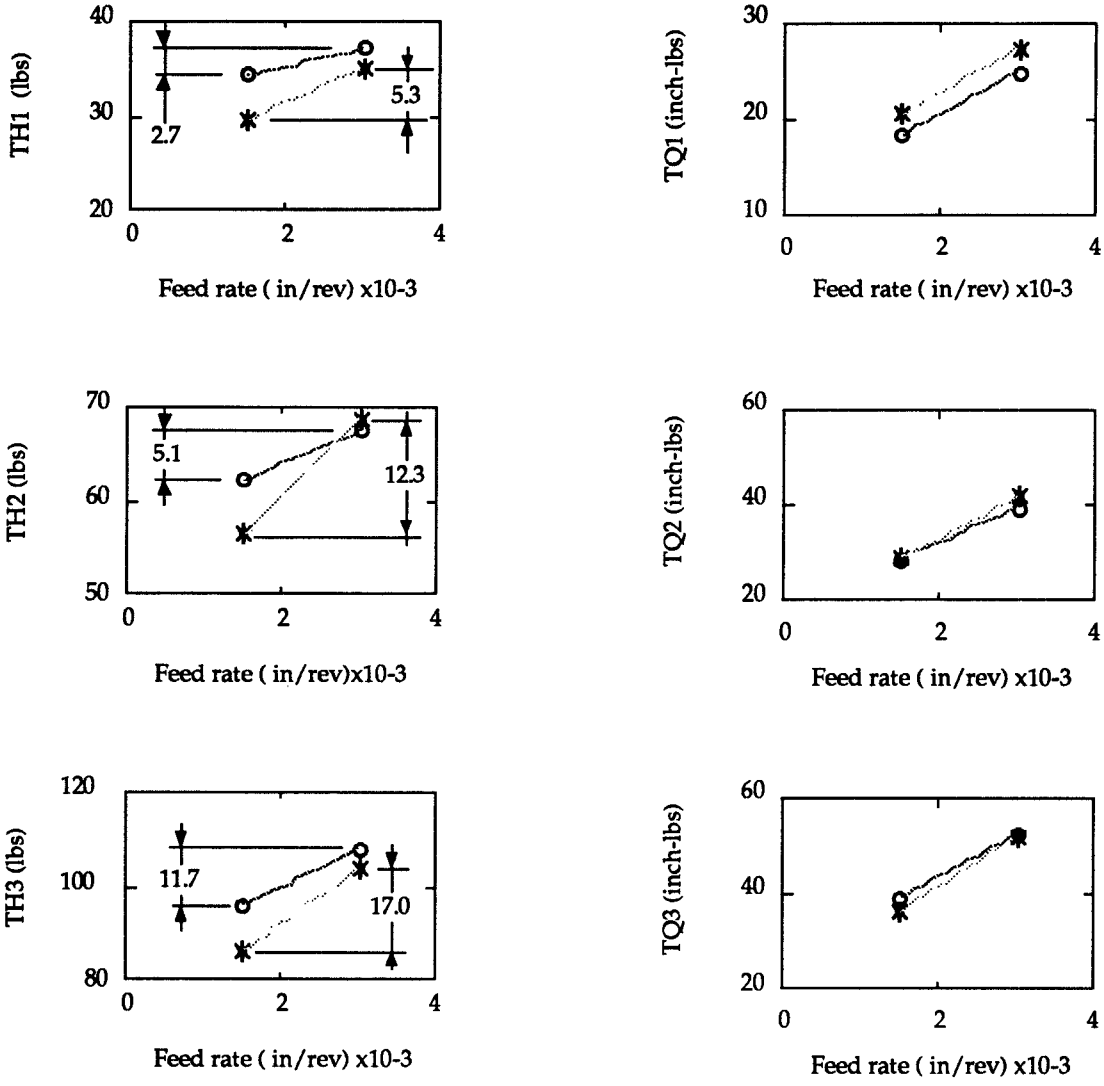

Figure 6.1 Feed rate effect on thrust and torque.

o Feed Rate 0.0015 in/rev

* Feed Rate 0.0030 in/rev

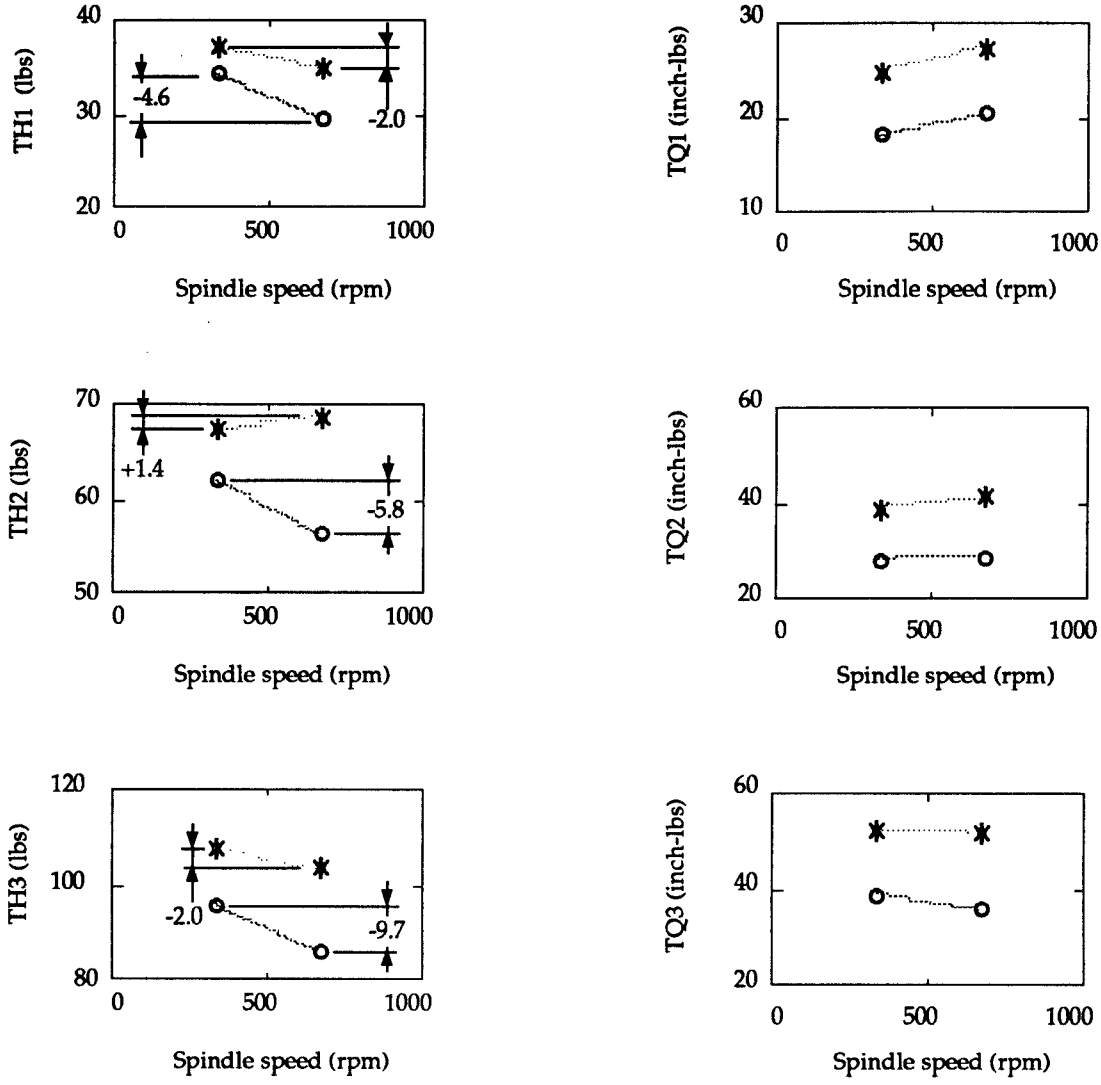

Figure 6.2 Spindle speed effect on thrust and torque.

1.3 lbs, as shown in Equation 6.5:

$$IF_{fn} = \frac{1}{2}[(35.0 - 37.0) - (29.7 - 34.3)] = 1.3 \tag{6.5}$$

Upon obtaining the four estimates through the factorial analysis, the development of an empirical model for thrust force prediction is completed. In the present case, the developed empirical model of drilling hole H1 is given by:

$$TH1_{prd} = 34 + \frac{4.0}{2}F - \frac{3.3}{2}N + \frac{1.3}{2}N \times F \tag{6.6}$$

For example, at given spindle speed and feed rate settings, say 325 rpm and 0.0015 inch/rev, the empirical model gives a thrust force prediction equal to 34.3 lbs. In fact, the measured thrust force was 34.3 lbs. Comparing the two numerical values, the prediction is at an accurate level. More important is that the developed empirical model enables us to estimate the thrust force at the spindle speed and feed rate settings which have not been tried yet. The prediction accuracy should be at an acceptable level as long as the given settings are within the experimental ranges specified by the upper and lower levels.

Based on the other thrust values in Table 6.1 and following the above procedure, the two empirical models, listed as Equations 6.7 and 6.8, represent the thrust force as a function of spindle speed and feed rate when drilling hole H2 and hole H3, respectively. The interaction of spindle speed and feed rate can also be seen in Figure 6.1 and 6.2.

$$TH2_{prd} = 63.7 + \frac{8.7}{2}F - \frac{2.2}{2}N + \frac{3.6}{2}N \times F \tag{6.7}$$

$$TH3_{prd} = 98.3 + \frac{14.4}{2}F - \frac{7.0}{2}N + \frac{2.6}{2}N \times F \tag{6.8}$$

Regarding the relations between the torque and cutting parameters, the data in Table 6.1 related to the torque measurements during the drilling tests are used. The following three equations are the empirical models to describe the torque as a function of spindle speed and feed rate.

$$TQ1_{prd} = 22.8 + \frac{6.9}{2}F + \frac{2.2}{2}N + \frac{0.2}{2}N \times F \tag{6.9}$$

$$TQ2_{prd} = 34.6 + \frac{11.5}{2}F + \frac{1.2}{2}N + \frac{0.9}{2}N \times F \tag{6.10}$$

$$TQ3_{prd} = 45.0 + \frac{14.5}{2}F - \frac{1.6}{2}N + \frac{1.3}{2}N \times F \tag{6.11}$$

As shown in the three torque plots on the right hand side in Figures 6.1 and 6.2, there is little effects of interaction of spindle speed and feed rate. It should be noticed that the interaction factors of the torque empirical models are less significant than their main factors. In addition, the noise level during experiment is 0.8 inch-lbs for torque. Consequently, these interaction factors can be neglected from the derived empirical models.

6.1.2 Interpretation of the Developed Empirical Model

From the results of the above factorial analysis, the following important conclusions can be made.

(1) The thrust generated during drilling decreases as spindle speed increases. Physical interpretation of the drilling processes would be the temperature effect. A high spindle speed is associated with a high temperature distribution in the cutting zone. The softening

of the workpiece material results in a small magnitude of the thrust force.

(2) The thrust generated during drilling increases as feed rate increases. This is simply due to the increase of the cutting area. However, the unit thrust, the ratio of the thrust to the cutting area decreases as feed rate increases. A possible reason could be the decrease of strain rate as a result of increase of the chip thickness.

(3) The increase of the thrust as feed rate increase is more significant at a high spindle speed (5.3 lbs) than the increase of the thrust at a low spindle speed (2.7 lbs). As indicated in Figure. 6.1, the difference in the thrust in the former case is almost two times that of the later. This provides an important observation that for maintaining an equivalent machining productivity, combinations of a low feed rate with a high spindle speed are preferable for the reduction or control of the thrust force.

6.1.3 Comparison Among the Developed Empirical Models

In this section, comparisons between the developed empirical models are made to reveal the characteristics of the thrust force and torque distributions along the cutting edges.

The first comparison is made among the three thrust force empirical models, namely, Equations 6.6 to 6.8. These three equations represent the thrust generated during drilling the three different holes, H1, H2, and H3. From the observation of the mean values, it is evident that the thrust force while drilling hole H3 is large since the drilling region is the largest and is

the closest to the drill center. On the other hand, the thrust involved in drilling hole H1 is relatively small. This indicates the importance of controlling the thrust force when small holes are drilled and the drill structural strength is extremely weak. In addition, the interaction between spindle speed and feed rate seems more effective in drilling hole H2. Such a strong interaction implies the necessity of a careful selection of spindle speed and feed rate for achieving an optimal drilling operation, which balance the quality and productivity needs.

The second comparison is among the three torque empirical models, namely, Equations 6.9 to 6.11. It is interesting to note that the three displayed patterns are similar to one another regarding both the magnitude and the interaction effect. Specifically, the numerical value of the displayed interaction is almost equal to zero. This important observation strongly indicates that, for drills with large diameters, controlling the rigidity of torsional deformation seems secondary compared to the control of the thrust. However, drills with small diameters might be subjected to excessive torsional deflection resulting drill failure or breakage during drilling operation.

6.2 Implementation of On-Line Monitoring

Increasing competition, high costs, and decreasing productivity force industry to production automation. A need for quality improvement, scrap rate reduction, and production rate promotion has led to a rapid development of sensor-based manufacturing systems which will eventually offer the manufacturing industries with untended machining. Appropriate

on-line monitoring systems and associated computer controls are the key to successful implementation of the untended machining.

In this thesis work, an on-line sensing system is designed and fabricated to measure the thrust and torque during drilling processes. After careful calibration, the designed sensing system is tested with great satisfaction as witnessed. Through the entire experimental studies performed in this thesis work, the developed sensing system has provided valuable information and data regarding the thrust, torque, and dynamic characteristics of the drill vibration. In this section, the use of the sensing system for on-line monitoring and a basic strategy for implementing a sensor-based drilling system are discussed.

Figure 6.3 presents a graphical view of a sensor-based drilling system. As indicated, the sensing system is fixed on the machine tool table. During drilling, the generated thrust and torque will be detected by the sensing system. For example, the output of the sensing system should be kept at a certain level when the drilling process is in its normal status. Any dramatical change of mean values or power spectra of the thrust and torque is an indication that the drilling process could go away from its normal status. For example, the drill wear during drilling could increase the mean value of the thrust and torque during drilling or change their power spectra. Consequently, the monitoring of the output signals from the sensing system represents an indirect method to perform an on-line monitoring of the drill wear progress. As indicated in Fig. 6.3, a computer-based controller is also required in the sensor-based drilling process. The controller receives the detected thrust and torque signals through a feedback path. A comparison between the detected signals and the predicted signals would be made to

produce the control signal for an adjustment to keep the drilling process in its normal status as long as the machining accuracy is maintained. Therefore, the main function of this built-in controller is to generate a signal to correct the drill motion, either through spindle speed, or through feed rate, or both. The central part of the controller is a physics-based system model to carry out an accurate prediction. The thesis research is mainly driven by this motivation.

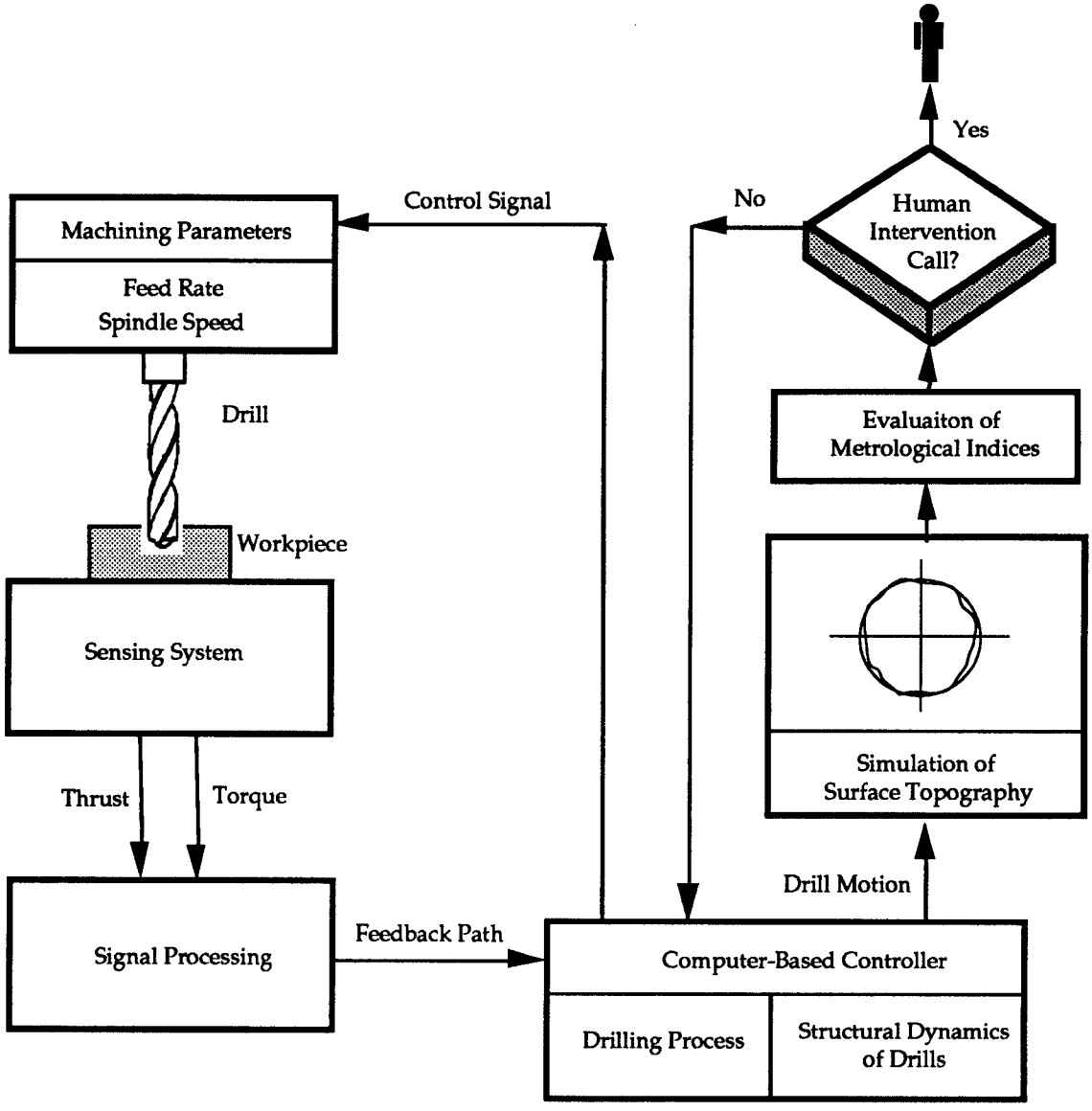

Figure 6.3 Sensor-based drilling system.

It should be pointed out that the implementation of the sensing system in this thesis work actually represents development of a prototype system for a sensor-based drilling system. It is anticipated that integration of the analytical and experimental work performed in this thesis research and expansion of such an integration will eventually lead to the implementation of a real sensor-based drilling system on the shop floor.

However, there are difficulties in implementing a sensor-based drilling system and an untended machining system. The major difficulty would be inadequate reliability and fast response control. The proposed sensing systems could not be capable of providing fast response due to the availability of inexpensive strain gages. Although high power computers enables us to develop and implement with great speed, lack of powerful sensor signature analysis systems and control strategies are still main concerns. There is a hope that in the near future, some reliable sensing and control systems will be available to meet the needs of untended manufacturing.

CHAPTER 7

CONCLUSIONS AND RECOMMENDATIONS

In this chapter, the main conclusions from the present study are summarized, followed by recommendations for future work.

7.1 Conclusions

In the present study, the investigation of thrust and torque generated during drilling processes is summarized into four aspects: analytical mathematical models, drill structure identification, drilling dynamometer development, and cutting parameter effects estimation.

(1) The mathematical models have been developed for thrust and torque prediction based on the drill geometry and the cutting parameters. An orthogonal cutting plane has been found in oblique cutting processes, which is applied to the cutting force analysis along the cutting edges of a drill.

(2) The drill structure is identified through the modal testing. The predicted response based on the identified modal parameters is at a reasonable accurate level compared to the measured response during vibration test.

(3) The prototype drilling dynamometer is designed and constructed. The measured dynamic signals reveal that the fundamental natural frequency of the dynamometer is higher than the lowest natural frequency of the drill structure. The stiffness of the whole

drilling system does not decrease due to the built dynamometer, which guarantees the reliability of the built dynamometer.

(4) By using the dynamometer, the cutting parameter effects on the thrust and torque are estimated. The combination of a low feed rate and high spindle speed is found to be the most efficient method for reducing or controlling the thrust force while maintaining an equivalent machining productivity.

7.2 Recommendations

Based on the present study, the following recommendations with respect to the future work in this area are made.

(1) The cutting mechanism of the web and the cutting edge near the drill center is suggested to be investigated for obtaining more complete mathematic models.

(2) Regarding surface topography, roundness, and cylindricity of finished holes after drilling processes, the structural dynamics of the drill should be investigated two-dimensionally. Not only the experimental work, but also the theoretical modeling has to be performed. Finite element method can be used to simulate the drill structure, and Rayleigh-Ritz method can be used to model the structure theoretically.

(3) For modern high speed machining systems, the built drilling dynamometer is not capable of providing fast response. Semiconductor strain gages could be useful in fulfilling the high sensitivity requirement.

References

1. Armarego, E. J. A. and Wiriyacosol, S.," Thrust and Torque Prediction in Drilling From a Cutting Mechanics Approach," Annals of the CIRP, Vol. 28, No. 1, 1979, pp.87-91.
2. Billau, D. J. and McGoldrick, P. F.," An Analysis of the Geometry of the Periphery of the Flank Face of Twist Drills Ground with Cylindrical and Conical Form," Int. J. Mach. Tool Des. Res. Vol. 19, pp. 69-86, 1979.
3. Bird, W. W. and Fairfield, H. P.,"A Twist Drill Dynamometer," Trans. ASME, vol.26, 1904-1905, pp.355-366.
4. Burnham, M. W.," An Analysis of Drill Deflection for Deep Miniature Holes," ASME Paper No. MR80-956, 1980, pp1-24.
5. Burnham, M. W., " The Mechanics of Drilling Small Holes," 10th North American Manufacturing Research Conference, Ontario, May 1983, pp.325-329.
6. Ewins, D. J., 1984, "Modal Testing: Theory and Practice,"Research Studies Press Ltd., pp.153-167.
7. Galloway, D. F., "Some Experiments on the Influence of Various Factors on Drill Performance," Trans. of ASME, Vol. 79, 1957, pp. 191-231.
8. Glaser, D. L. and Nachtigal, C. L., "Development of a Hydraulic Chambered, Actively Controlled Boring Bar," J. of Engr. for Industry, Trans. ASME. Vol. 101. Nov. 1979, pp. 362-368.
9. Kaczmarek, J., "Principles of Machining By Cutting, Abrasion and Erosion," Peter Peregrinus Limited, Stevenage, England, 1976.

10.. Kline, W. A., DeVor, R. E. and Lindberg, J. R., "The Prediction of Cutting Forces in End Milling with Application To Cornering Cuts," Int. J. Mech. Tool Des. Res., Vol. 22 No.1. pp. 7-22. 1982.

11. Kline, R. G. and Nachtigal C. L., "The Application of Active Control to improve Boring Bar Performance," Trans. ASME. Series G. Vol. 97, Nov. 1975 pp.179-183.

12. Kronenberg, M., "Machining Science and Application," Pergamon Press Inc., 1966.

13. Lee S. J., "The Influence of drill Characteristics and Entry Mechanisms in Drilling Performances," Ph.D. Thesis, Univ. of Wisconsin-Madison, 1986.

14. Magrab, E. B. and Gilsinn D. E., "Buckling Load and Natural Frequencies of Drill Bits and Fluted Cutters," ASME, Journal of Engineering for Industry, Vol. 106, Aug. 1985, pp. 196-204.

15. MacBain, J. C., Harding, K. G. and Tekinalp, O., "Vibration Modes and Frequencies of Twist Drills Using Laser Holographic Interferometry,"

16. Merchant, M. E., "Basic Mechanics of the Metal-Cutting Process," J. of Appl. Mech. Sept. 1944, pp. A-168 to A-175.

17. Merritt, H. E., "Theory of Self-Excited Machine-Tool Chatter." Trans. ASME, Vol.87, November 1965, pp. 447-454.

18. Nakayama, K. and Ogawa, M, "Basic Rules on the form of Chip in Metal cutting," Ann CIRP v27 n1 1978, Gen Assem of CIRP, 28th: Manuf Technol, Eindhoven, Neth, Aug 28-Sep 2 1978. Publ by Tech Rundsch, Berne, Switz, 1978, pp 17-21.

19. Oxford, Jr C. J., "On the Drilling of Metals 1 Basic Mechanics of the Process," Trans. Am. Soc. mech. Engrs., Vol. 77, February 1955, pp. 103-114.

20. Rolt, L. T. C., "A Short Story of Machine Tools," The M. I. T. Press, Massachusetts Institute of Technology, Cambridge, Massachusetts 1965.

21. Shaw, M. C., "Metal Cutting Principles," Oxford University Press Inc., 1984.

22. Shaw, M. C. and Oxford, JR. C. J. , "On the Drilling of Metals 2 The Torque and Thrust in Drilling," Trans. Am. Soc. mech. Engrs., Vol. 79, January 1957, pp. 139-148.

23. Shi H.M.," A New Method for Analyzing and Calculating Angles On Cutting Tools," Int. J. Mach. Tool Des. Res. Vol. 22, No.3, pp. 177-196, 1982.

24. Smith, J. D. and Tobias, S. T., "The Dynamic Cutting of Metals," Int. J. Mach. Tool Des. Res., Vol. 1, No. 4, 1961, pp.283-292.

25. Stabler, G. V. (1951). Proc. Instn Mech. Engrs 165,14.

26. Taylor, F. W., "On the Art of Cutting Metals,"Trans. ASME, Vol.28, 1906, p.240.

27. Tobias, S. T. and Fishwish, W., "Theory of Regenerative Machine Tool Chatter,"Engineer, London, Vol.205, 1958, pp. 199.

28. Thomson, W. T., 1988, "Theory of Vibration with Application," Prentice-Hall International, Inc., Third Edition, pp 67-74.

29. Tsai, W. D. and Wu, S. M.," Computer Analysis of Drill Point Geometry," Int. J. Mach. Tool Des. Res. Vol.19, pp.95-108, 1979.

30. William, J. E., "A Dynamic Model of The Cutting Force System In The Turning Process," M. S. Thesis, Univ. of Illinois at Urbana-Champaign, 1990.

31. Williams, R. A., " A study of the Basic Mechanics of the Chisel Edge of a Twist Drill," Int. J. Prod. Res. Vol. 8, No.4, 1970, pp.325-343.

32. Williams, R. A., " A Study of the drilling Process," ASME, Journal of Engineering for Industry, Vol. 96, Nov. 1974, pp.1207-1215.

33. Wu, S. M. and Shen, J. M., "Mathematical Model of Multifaceted Drills," Trans. of the ASME, J. of Eng. for Ind., Vol. 105, 1983, pp. 173-182.

34. Zhang, G. M., "Dynamic Modeling and Dynamics Analysis of the Boring Machining System," Ph.D. Thesis, University of Illinois at Urbana-Champaign, 1986.

Appendix A

Derivation of the Effective Rake Angle and the Split Angle

Referring to Figure 2.3, the effective rake angle is

$$\sin(\alpha e) = \frac{\overline{CC'} + \overline{D'C'}}{\overline{OC}}$$

where

$$\overline{CC'} = \overline{OA} * \frac{\sin(\alpha n)}{\cos(i)}$$

$$\overline{D'C'} = \sin(i) * (\overline{AC} - \overline{AB})$$

$$= \sin(i) * [\overline{OA} * \tan(\eta c) - \overline{OA} * \sin(\alpha n) * \tan(i)]$$

$$\overline{OC} = \frac{\overline{OA}}{\cos(\eta c)}$$

Therefore $\sin \alpha e = \sin \eta c * \sin i + \cos \eta c * \cos i * \sin \alpha n$

Referring to the split angle, γ, shown in Figure 2.2, it is obtained by projecting the angle γ', on to the reference plane with inclination angle i. The angle, γ', is,

$$\tan(\gamma') = \frac{\overline{BC}}{\overline{B'B}} = \frac{\overline{OA} * \tan(\eta c) - \overline{OA} * \sin(\alpha n) * \tan(i)}{\overline{OA} * \cos(\alpha n)}$$

Therefore the split angle, γ , is,

$$\tan(\gamma) = \tan(\gamma') * \cos(i)$$

$$= \tan(\eta c)\frac{\cos(i)}{\cos(\alpha n)} - \sin(i) * \tan(\alpha n)$$

Appendix B

Programs for Constant Determination and Numerical Simulation

Constant Determination

```
clear
clg

% Measured ΔTH & ΔTQ
th1=[34.28 27.87 33.82];                    % ΔTH of Test 1
th2=[37.04 30.29 40.4];                     % ΔTH of Test 2
th3=[29.65 26.74 29.94];                    % ΔTH of Test 3
th4=[35.01 33.72 34.61];                    % ΔTH of Test 4
tq1=[18.36 10.37 10.45];                    % ΔTQ of Test 1
tq2=[25.09 14.29 13.03];                    % ΔTQ of Test 2
tq3=[20.38 8.59 7.29];                      % ΔTQ of Test 3
tq4=[27.53 14.10 10.63];                    % ΔTQ of Test 4
th=[th1 th2 th3 th4];
tq=[tq1 tq2 tq3 tq4];

% Transformation from (ΔTH & ΔTQ) to (ΔRn & ΔRt)
cs=118/2/180*pi;                            % Lead angle
ae=[0.4421 0.2922 0.1856];                  % Effective rake
rr=[0.2820 0.3264 0.5221];                  % Split angle
or=[9.5 6.5 3.5]/32;                        % Radius
ae=[ae ae ae ae];
rr=[rr rr rr rr];
r=[or or or or];
w=cs*ones(rr)+rr;
ΔRn=-sin(ae)./sin(w).*th/2+cos(ae).*tq./r/2;    % ΔRn
ΔRt=cos(ae)./sin(w).*th/2+sin(ae).*tq./r/2;     % ΔRt

% Linear regression in logarithmic scale
v=2*pi*or; vv=[325*v 660*v 325*v 660*v];
x=log(vv);                                  % Cutting speed factor
vae=(80*ones(ae)-ae/pi*180)/50;
y=log(vae);                                 % Rake angle factor
f=[0.0015*ones(th1) 0.030*ones(th1)]; f=[f f];
z=log(f);                                   % Feed rate factor
trans=[ones(x);x;y;z]';                     % Least squares method
cn=trans\log(ΔRn)';                         % Constants for ΔRn
ct=trans\log(ΔRt)';                         % Constants for ΔRt
```

Numerical Simulation

```
clear;
clg;

% Operating Conditions
sp=325;                                          % Spindle speed
f=0.0015;                                        % Feed rate

% Material properties
cn=31.7134;                                      % Constants for ΔRn
nf=2.4649; nv=-1.8816; nr=-5.9602;
ct=17.4092;                                      % Constants for ΔRt
tf=1.2251; tv=-0.8843; tr=-4.6777;

% Geometry of the drill
rmax=11/32;                                      % Radius of drill
rmin=2/32;                                       % Radius of hole
d=rmax-rmin;                                     % Depth of cut
dr=0.01;                                         % Radius increment
r=(rmin:dr:rmax);                                % Radius variable
hlx=32/180*pi;                                   % Helix angle
point=118/180*pi;                                % Point angle
web=0.11;                                        % Web thickness
as=-asin(r.\web/2);                              % Side rake
ab=atan(tan(hlx)*r/rmax);                        % Back rake
cs=point/2;                                      % Lead angle
i=atan(tan(ab)*cos(cs)-tan(as)*sin(cs));         % Inclination
av=atan(tan(as)*cos(cs)+tan(ab)*sin(cs));        % Velocity rake
an=atan(cos(i).*tan(av));                        % Normal rake
ae=asin(sin(i).*sin(i)+cos(i).*cos(i).*sin(an)); % Effective rake
rr=atan(sin(i)./cos(an)-tan(an).*sin(i));        % Split angle

% Calculation of thrust & torque
x=2*pi*sp*r;                                     % Cutting speed factor
y=(80*ones(r)-ae*180/pi)/50;                     % Effective rake factor
z=f;                                             % Feed rate factor
ΔRn=exp(cn)*(z^nf)*(x.^nv).*(y.^nr)/(3/32);      % ΔRn
ΔRt=exp(ct)*(z^tf)*(x.^tv).*(y.^tr)/(3/32);      % ΔRt
w=cs*ones(r)+rr;
Δfx=ΔRn.*cos(w).*sin(ae)-ΔRt.*cos(w).*cos(ae);   % ΔFx
Δfy=ΔRn.*cos(ae)+ΔRt.*sin(ae);                   % ΔFy
Δfz=-ΔRn.*sin(w).*sin(ae)+ΔRt.*sin(w).*cos(ae);  % ΔFz
th=2*sum(Δfz*dr)                                 % Thrust
tq=2*sum(r.*Δfy*dr)                              % Torque
```

Appendix C

Receptance of MDOF System

$$[K + iH - \omega^2 M]\{x\}e^{i\omega t} = \{f\}e^{i\omega t}$$

$$\{x\} = [K + iH - \omega^2 M]^{-1}\{f\} = [R(\omega)]\{f\}$$

$$[K + iH - \omega^2 M] = [R(\omega)]^{-1}$$

By applying the mass orthogonality of the mass normalized mode shape vectors, described by the following equations:

$$[\phi]^T[M][\phi] = [I]$$

$$\{\phi\}_r = \frac{1}{\sqrt{m_r}}\{\varphi\}_r$$

where $\{\varphi\}_r$ is the r^{th} mode shape.

$\{\phi\}_r$ is the r^{th} mass normalized mode shape.

$[m_r] = [\varphi]^T[M][\varphi]$ is the normalized factor.

the equation can be written as:

$$[\phi]^T[R(\omega)]^{-1}[\phi] = \left[(\lambda_r^2 - \omega^2)\right], \qquad \text{where } \lambda_r^2 = \omega_r^2 + i\eta_r\omega_r^2$$

$$[R(\omega)] = [\phi]\left[(\lambda_r^2 - \omega^2)\right]^{-1}[\phi]^T$$

The receptance of MDOF system is

$$R_{jk}(\omega) = \sum_{r=1}^{n} \frac{\phi_{jr}\phi_{kr}}{\omega_r^2 - \omega^2 + i\eta_r\omega_r^2}$$

Appendix D

Structural Damping SDOF System

According to Thomson [27], " Experiments by several investigators indicate that for most structural metals, such as steel or aluminum, the energy dissipated per cycle is independent of frequency over a wide frequency range and proportional to the square of the amplitude of vibration. Internal damping fitting this classification is called solid damping or structural damping." Energy dissipated per cycle for structural damping is

$$W_{ds} = h\pi X^2 \qquad /h\pi, \text{ a constant}$$

Assuming harmonic oscillations, , energy dissipated per cycle for viscous damping is

$$W_{dv} = \oint c\dot{x}dx = \oint c\dot{x}^2 dt$$

$$= c\omega^2 X^2 \int_0^{\frac{2\pi}{\omega}} \cos(\omega t - \phi)dt = \pi c\omega X^2$$

By equating the energy dissipated by the two, an equivalent viscous damping is given as

$$c_{eq} = \frac{h}{\omega}$$

The equation of motion for structural damping may be written as

$$m\ddot{x} + \frac{h}{\omega}\dot{x} + kx = f(t)$$

Because of the harmonic oscillations, the equation becomes

$$(-m\omega^2 + k + ih)Xe^{i\omega t} = Fe^{i\omega t}$$

The receptance, defined as displacement/force is

$$R(\omega) = \frac{X}{F}(\omega) = \frac{1}{-m\omega^2 + k + ih} = \frac{A}{\omega_n^2 - \omega^2 + i\eta\ \omega_n^2}$$

where $\eta=\eta/k$, $A=1/m$.

$$R(\omega) = \frac{A(\omega_n^2 - \omega^2)}{(\omega_n^2 - \omega^2)^2 + (\eta\ \omega_n^2)^2} + i\frac{A(\eta\omega_n^2)}{(\omega_n^2 - \omega^2)^2 + (\eta\ \omega_n^2)^2}$$

$$= Re(R) + i\ Im(R)$$

$$(Re(R))^2 + (Im(R) + \frac{A}{2\omega_n^2\eta})^2 = (\frac{A}{2\omega_n^2\eta})^2$$

The polar (Nyquist) plot of receptance for a structural damped SDOF system form a circle of radius $A/2\omega n^2\eta$, center at (0, $-A/2\omega n^2\eta$).

Appendix E

Modal Circle Properties

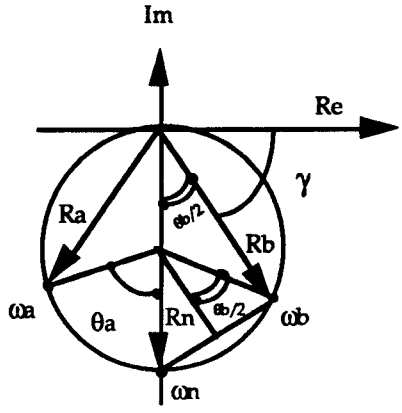

For a point ωb along the path of the plot, the tangent of the phase angle of the complex receptance,tan(γ), can be described as the ratio of its imagery part and the real part:

$$\tan(\gamma) = \frac{\eta \omega_n^2}{\omega_n^2 - \omega_b^2}$$

The complementary angle of γ is $\frac{\theta_b}{2}$, such that

$$\tan(\frac{\theta_b}{2}) = \frac{1-(\frac{\omega_b}{\omega_n})^2}{\eta}$$ also for point ωa $$\tan(\frac{\theta_a}{2}) = \frac{1-(\frac{\omega_a}{\omega_n})^2}{\eta}$$

By adding the above two equations, the damping factor η becomes,

$$\eta = \frac{\omega_a^2 - \omega_b^2}{\omega_n^2} \frac{1}{\tan(\frac{\theta_a}{2}) + \tan(\frac{\theta_b}{2})}$$

Appendix F

Program to Identify Modal Parameters and the Measured Inertance

```
function [wn,zt,ar,xc1,yc1,r]=curfit(f,h);
%
%  find the nature frequency, Wn
%
[s,i]=sort(-abs(h));            % the maximum response
wn=f(i(1));
%
%  find Xc, Yc, R of the modal circle
%
x1=real(h);
y1=imag(h);
a1=[sum(x1.*x1) sum(x1.*y1) sum(x1);
   sum(x1.*y1) sum(y1.*y1) sum(y1);
   sum(x1)    sum(y1)    length(x1)];
b1=[-sum(x1.*x1.*x1+x1.*y1.*y1);
   -sum(x1.*x1.*y1+y1.*y1.*y1);
   -sum(x1.*x1    +y1.*y1    )];
p1=a1\b1;
xc1=-p1(1)/2;
yc1=-p1(2)/2;
r1=(xc1^2+yc1^2-p1(3))^.5;
r=r1;
%
%   find the modal damping, zt
%
dif=length(f)/5;
tha=asin(abs(h(i(1))-h(i(1)+dif))/2/r1);    % tha & thb are 2-sided
thb=asin(abs(h(i(1))-h(i(1)-dif))/2/r1);    % of Wn by 'dif' points
zt=(f(i(1)+dif)^2-f(i(1)-dif)^2)/wn^2/(tan(tha)+tan(thb));
%
%  find the modal constant, Ar
%
ar=2*r1*wn^2*zt*4*pi^2;
```

Inertance at station 1

(A)

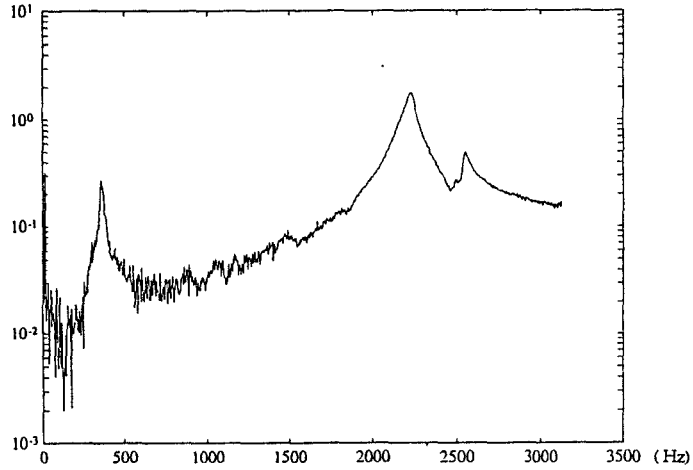

(B)

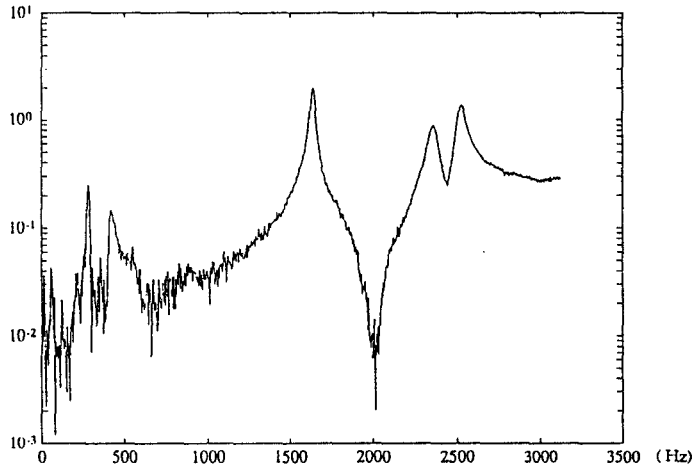

(C)

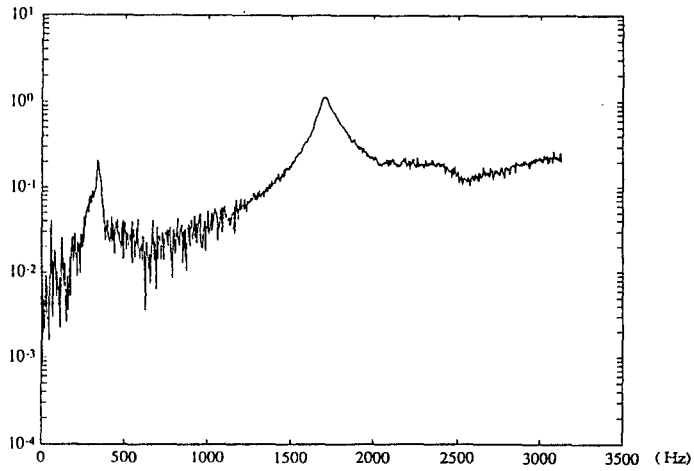

Inertance at station 2

(A)

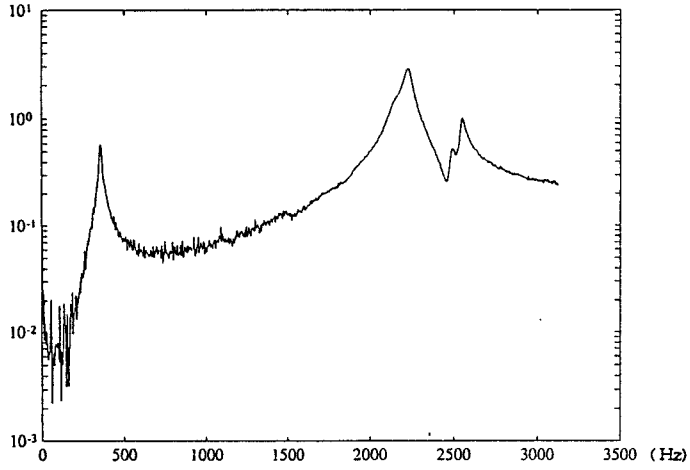

(B)

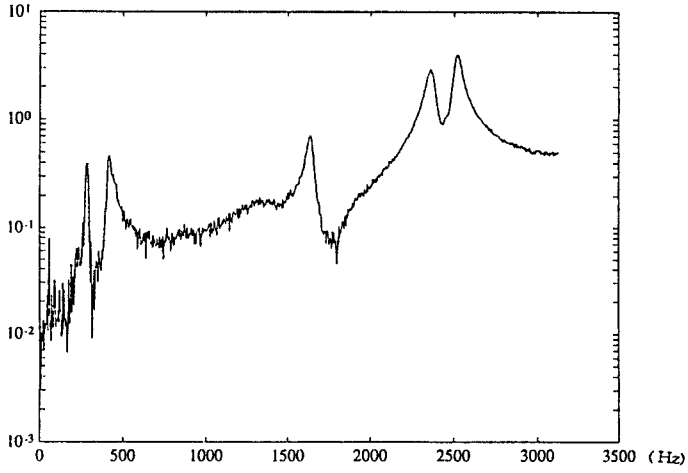

(C)

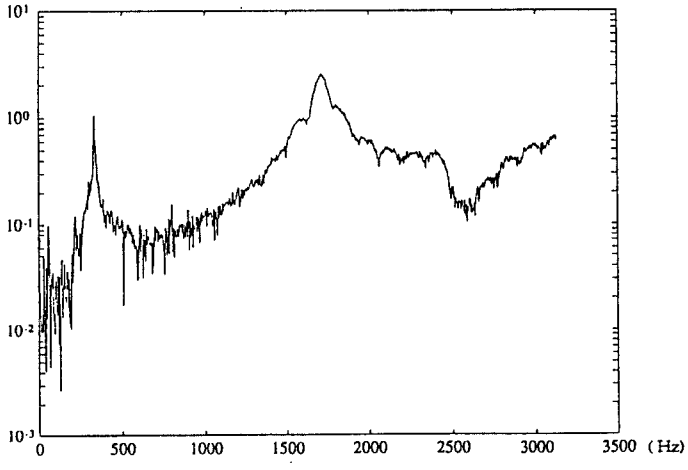

Inertance at station 3

(A)

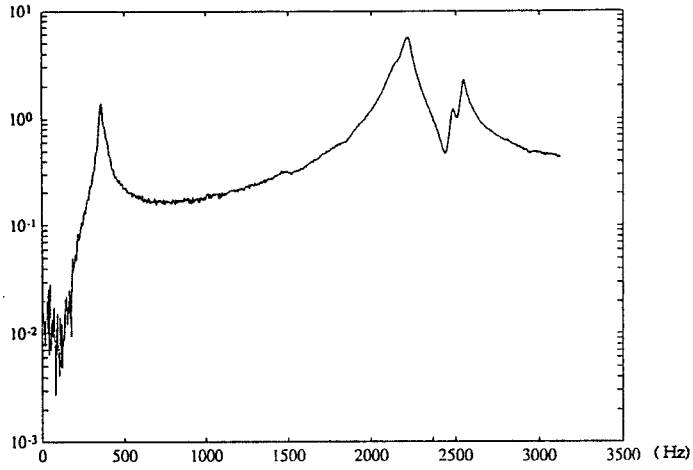

(B)

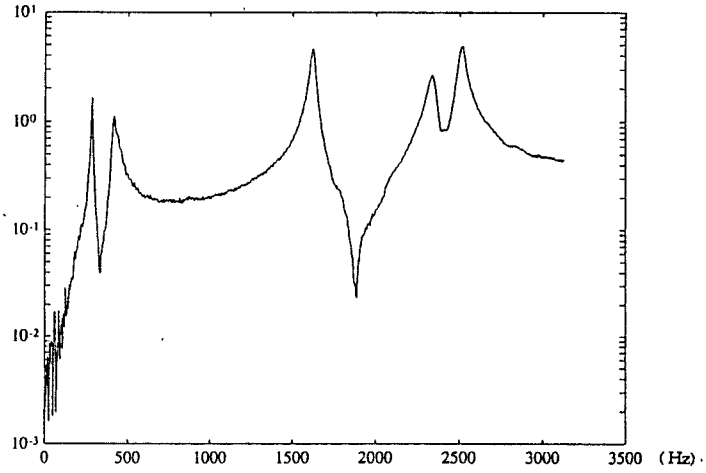

(C)

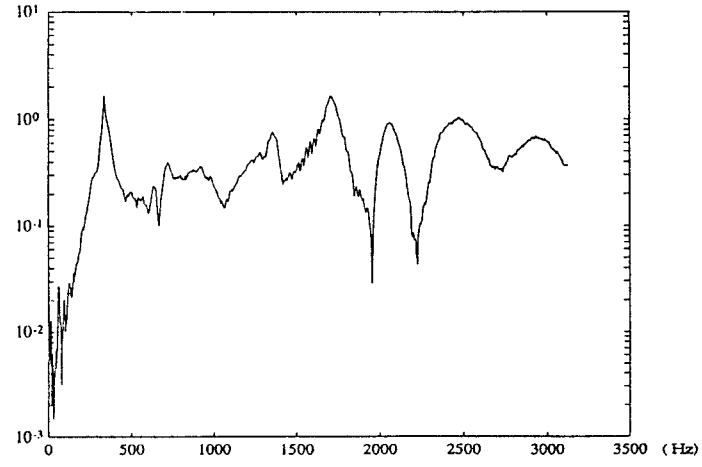

Inertance at station 4

(A)

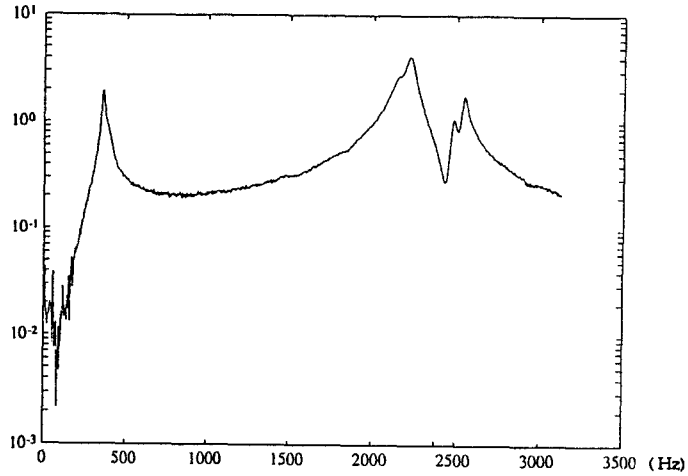

(B)

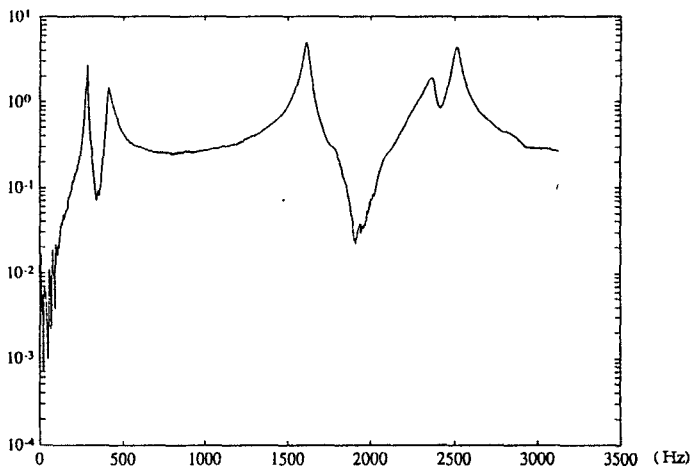

(C)

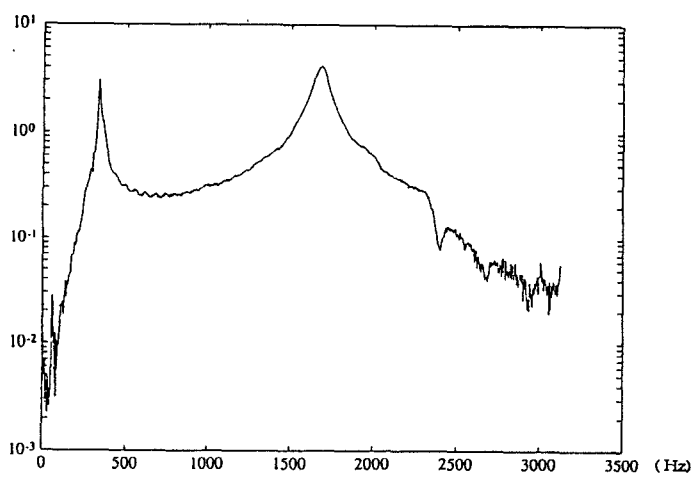

Inertance at station 5

(A)

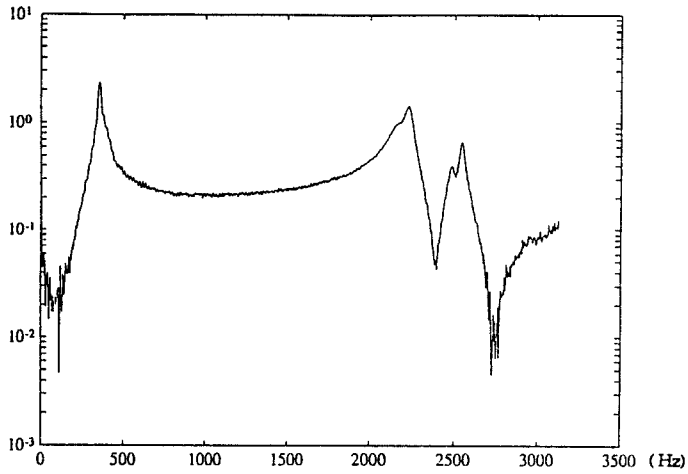

(B)

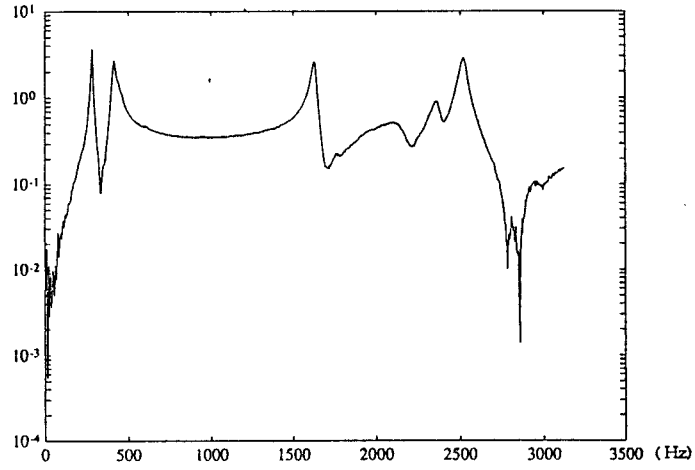

(C)

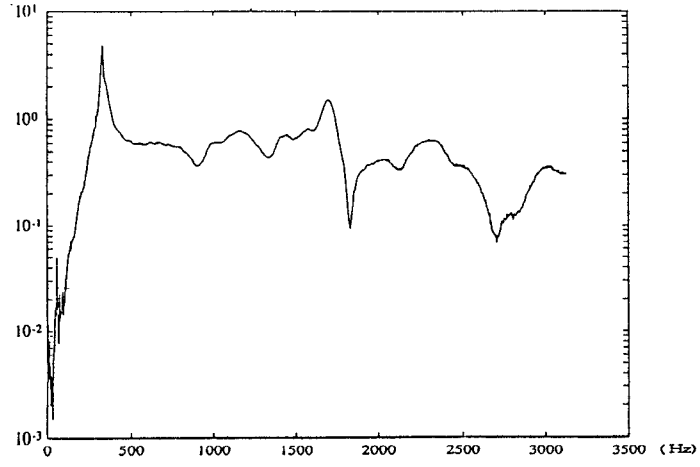

Inertance at station 6

(A)

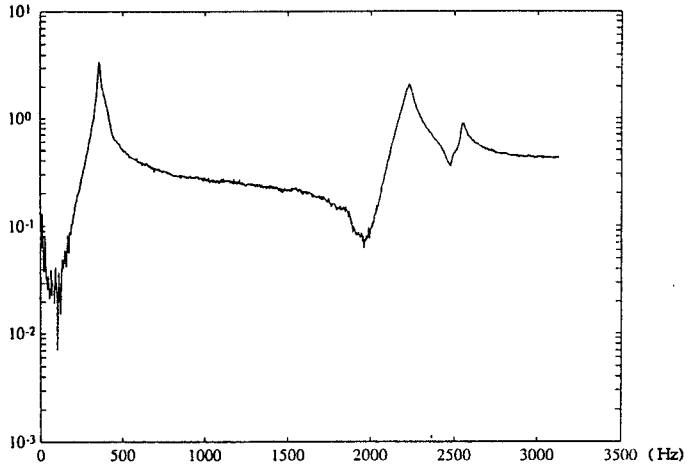

(B)

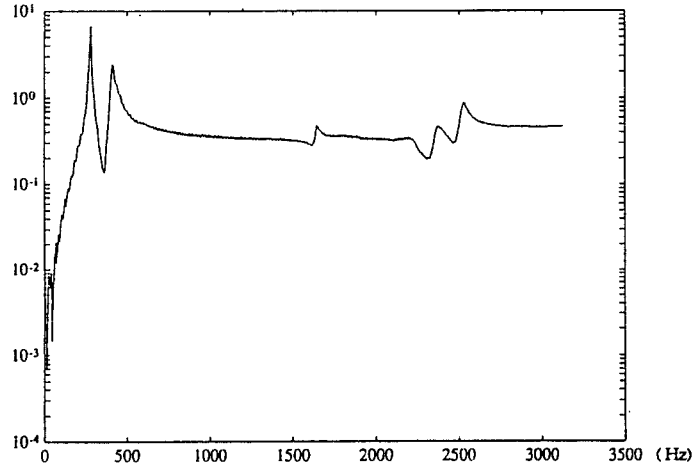

(C)

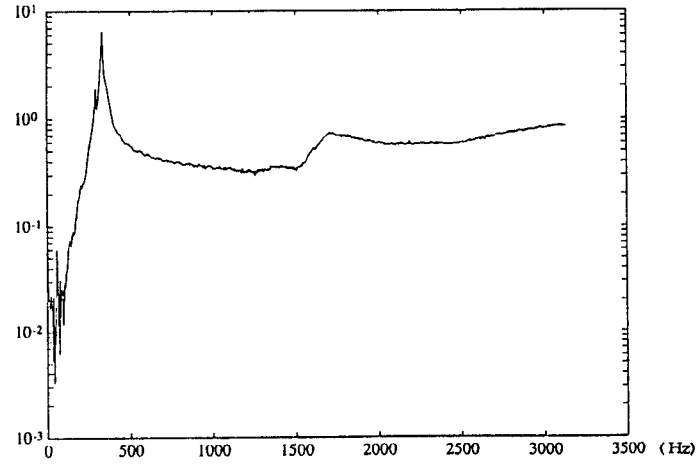

Inertance at station 7

(A)

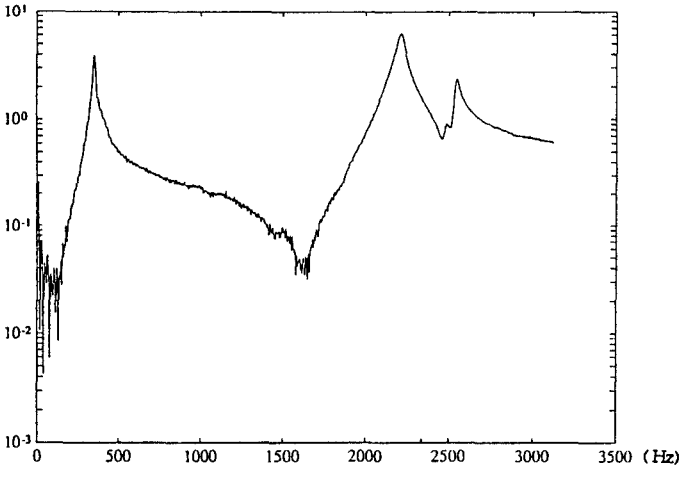

(B)

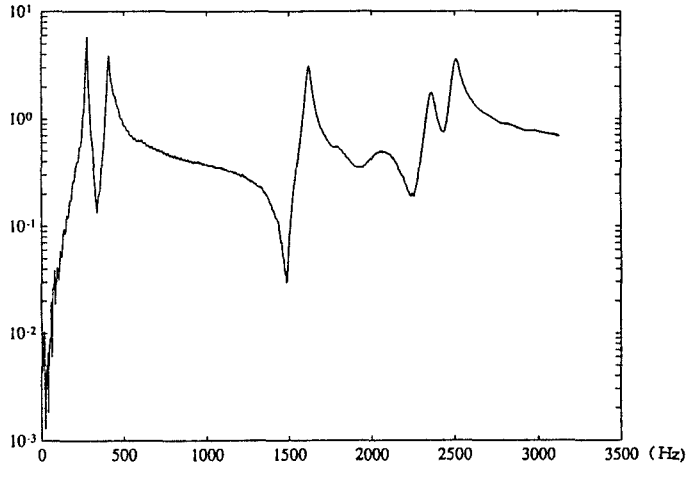

(C)